

Università degli Studi di Torino



Facoltà di Scienze Matematiche, Fisiche e Naturali

Dipartimento di Fisica Sperimentale

Dottorato di Ricerca in Fisica Fondamentale, Applicata ed Astrofisica

XX ciclo – a.a. 2004–2007

A study of the proton spectra from hypernuclear Non Mesonic Weak Decay with FINUDA

Candidato

Stefania Bufalino

Relatore

Prof. Tullio Bressani

Coordinatore

Prof. Stefano Sciuto

Settore scientifico disciplinare: FIS/04

Contents

1	Λ hypernuclei	7
1.1	Introduction	7
1.2	Production of Λ hypernuclei	8
1.3	Strangeness exchange production	16
1.3.1	In flight production	17
1.3.2	Production with K^- at rest	17
1.4	Associated production reaction	20
1.5	Photoproduction reaction	21
2	Weak Decay modes of Λ Hypernuclei	23
2.1	Introduction	23
2.2	Weak decay modes of Λ -Hypernuclei	24
2.2.1	The mesonic decay	25
2.2.2	The non mesonic decay	28
2.3	Theoretical Models	30
2.4	Experimental results	32
3	The FINUDA experiment	41
3.1	The DAΦNE collider	41
3.2	Experimental setup for the first data taking	43
3.2.1	The vertex region	45
3.2.2	The tracking region	48
3.2.3	The outer scintillator array	50
3.2.4	The Magnet	51
3.3	FINUDA Experimental setup for 2006/2007 data taking	51

4	Offline software and simulation method	55
4.1	The FINUDA Off-line software	56
4.1.1	General framework and tools	56
4.1.2	General Event Reconstruction procedures.	58
4.2	The FINUDA MonteCarlo simulation	64
4.3	FINUDA acceptance calculation	67
4.4	FINUDA Particle IDentification	71
5	Data Analysis	75
5.1	First analysis of ${}_{\Lambda}^{12}\text{C}$	77
5.2	NMWD of the ${}_{\Lambda}^7\text{Li}$	82
5.3	NMWD of ${}_{\Lambda}^5\text{He}$	88
5.3.1	Proton weak decay of ${}_{\Lambda}^5\text{He}$ from ${}^7\text{Li}$ targets	88
5.3.2	Proton weak decay of ${}_{\Lambda}^5\text{He}$ from ${}^6\text{Li}$ targets	89
5.4	New analysis of ${}_{\Lambda}^{12}\text{C}$	97
6	Results and comparisons	103
6.1	R_p calculation	103
6.2	Experiments vs Theory	107
7	Conclusions	113
	List of Tables	115
	List of Figures	115

Introduction

Hypernuclear physics was born in 1953, when the Polish physicists M. Danysz and J. Pniewski [1] observed, in a stack of photographic emulsions exposed to cosmic rays at around 26 km above the ground, the first hypernucleus through its decay. Since the strange quark is not a normal building block of nucleons and nuclei, strangeness production is a powerful tool to study properties of hadronic matter. As in the study of any complex system, the inclusion of an “impurity” and the study of its subsequent propagation provides us with a way to reveal configurations or states that can not be reached otherways.

After the first evidence of hyperfragments in cosmic ray interactions with nuclei, starting from the end of the Sixties, the installation of beams of K^- mesons at particle accelerators made it possible to study the formation of hypernuclei in the laboratory. Starting from the Seventies, the study of hypernuclei was continued with K^- beams by means of counter techniques with magnetic spectrometers and the introduction of new particle detectors (multiwire proportional chambers and drift chambers). The identification of well defined excited hypernuclear levels, by means of the kinematical analysis of the production reaction, was one of the most important results of a first series of experiments started at CERN and continued at Brookhaven (USA).

In the Eighties, a new technique for hypernucleus production was introduced at the Brookhaven laboratory, by means of intense beams of high energy π^+ . The interest in these new data has triggered the attention of the nuclear physics community and, in the last few years, different laboratories around the world have started a hypernuclear physics program: COSY at

Jülich in Germany, TJNAF at Newport News in USA, Nuclotron in Dubna (Russia). In particular the Italian hypernuclear project, the FINUDA experiment (acronym of FIsica NUcleare a DAΦNE) at the Laboratori Nazionali di Frascati of INFN has just concluded his second data taking.

FINUDA is the first example of a nuclear physics experiment, which is typically a fixed target experiment, carried out at a collider. The main purposes of the experiment are the high resolution spectroscopy of Λ hypernuclei and the study of their non mesonic weak decay.

Non Mesonic Weak Decay (NMWD) of hypernuclei provides the only practical tool of exploring the four fermion, strangeness-changing $N\Lambda \rightarrow NN$ weak interaction. Furthermore the large momentum transfer in the non mesonic decay process suggests a way to probe short distance aspects of the interaction, possibly revealing baryon substructure effects.

The study of the NMWD with the FINUDA data, collected during the first and the second data taking, is the subject of this thesis. After a description of the production method of Λ hypernuclei and an explanation of the importance of the NMWD process, the FINUDA experiment is briefly described. Then I will describe the analysis tools employed in the data analysis thus showing the experimental results I obtained. Finally a comparison with the theoretical expectation and previous experimental results is presented.

Chapter 1

Λ hypernuclei

1.1 Introduction

A hypernucleus is a nucleus in which one or more nucleons have been replaced by hyperons. Hyperons (Λ , Σ , Ω , Ξ) have lifetime of the order of 10^{-10} sec (apart from the Σ^0 , which decays into $\Lambda\gamma$) and they decay weakly, with a mean free path $\lambda \sim c\tau = O(10\text{cm})$.

The more known and studied hypernuclei from longtime (54 years) are Λ -hypernuclei, in which one Λ hyperon replaces a nucleon of the nucleus; they are indicated by the suffix Λ preceding the usual notation of nuclei: ${}^A_{\Lambda}Z$. Hypernuclei are stable at the nuclear time scale (10^{-23} s) since the Λ particle, the lightest of the hyperons, maintains its identity even if embedded in a system of other nucleons; the only strong interaction which conserves strangeness and is allowed is, in fact, elastic scattering. When a Λ hyperon replaces one of the nucleons, the original nuclear structure changes to a system composed by the hyperon and the *core* of the remaining nucleons. The Λ -*core* system is rearranged in order to generate a bound state maximizing the binding energy B_{Λ} , so the depth of the Λ potential hole is different from the one of a nucleon within the nuclear medium.

In Fig.1.1 the mass number dependence of measured values of B_{Λ} is showed thus revealing that the binding energy saturates at a value of 25 MeV. Once a hypernucleus is formed, the Λ is not subject to *Pauli principle*: this is due to the strangeness of the Λ particle, which gives it one degree of free-

dom more and makes it distinguishable from the other nucleons; hence the hyperon inside the hypernucleus can be used as a unique probe to investigate the interior of the nucleus. The existence of hypernuclei gives a new dimension to the traditional world of nuclei (states with new symmetries, selection rules, etc). They represent the first kind of *flavoured nuclei*, in the direction of other exotic systems (charmed nuclei and so on).

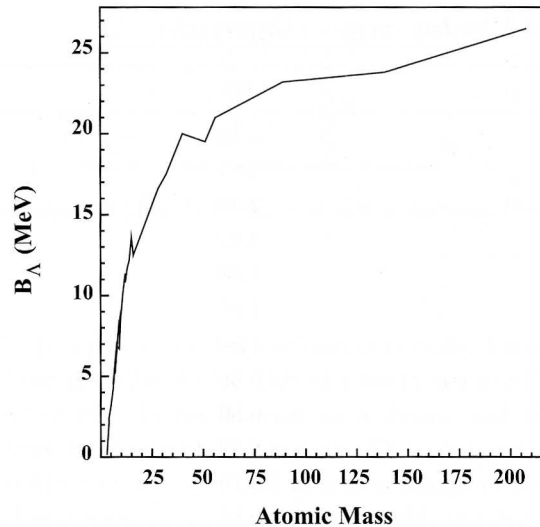


Figure 1.1: Mass number dependence of the Λ binding energy [2] .

1.2 Production of Λ hypernuclei

In the first stage of Hypernuclear Physics (1953-1972), experiments were carried out with visualizing techniques and no special care was devoted to the quality or the energy of the incident beam. The main requirement was that the incident particle would have enough energy to produce a Λ , which could eventually stick to one of the fragments of the nucleus disintegrated by the projectile. This fact was also the reason for which Hypernuclei were often called "Hyperfragments".

From 1972 two-body reactions producing Λ 's on a nuclear target were

studied. The two-body reactions that led to practically all the present bulk of experimental information are:

1. The ‘‘Strangeness Exchange’’ reaction:



exploited mainly in the $K^- + n \rightarrow \Lambda + \pi^-$ charge state, for evident reasons of easiness for spectroscopizing the final state π . The reaction can be seen as a transfer of the s -quark from the incident meson to the struck baryon.

2. The ‘‘Associated Production’’ reaction



This reaction can be seen as a creation of a $(s\bar{s})$ pair by the incident meson.

From 1972 the major part of experimentalists involved in Strange Nuclei Physics had a formation and an approach typical of Nuclear Physics. Quite recently a third kind of reaction, the electroproduction of Strangeness on protons in the very forward direction was exploited:



In these kinematical condition the virtual photons associated to the reaction (1.3) can be regarded as quasi-real and (1.3) is often rewritten as a two-body photoproduction reaction:



It must be noticed that, whereas with reactions (1.1) and (1.2) it is possible to replace a neutron in the target nucleus by a Λ , with reaction (1.3) a proton is replaced by a Λ , and the neutron-rich mirror Hypernucleus is obtained out from the same nuclear target. Just for example, with reaction (1.1) and (1.2) on a ^{12}C target $^{\Lambda}_{12}\text{C}$ is produced, with reaction (1.3) $^{\Lambda}_{12}\text{B}$.

Experiments performed with projectiles different than those needed for reactions (1.1), (1.2) and (1.3), like protons [3], antiprotons [4] or relativistic Ions were also performed, but they did not supply systematic series of results.

Each of the aforesaid reactions has its own characteristics in the elementary cross-section, internal quantum numbers transfer, momentum transfer, absorptions of incoming and outgoing particles in nuclear matter.

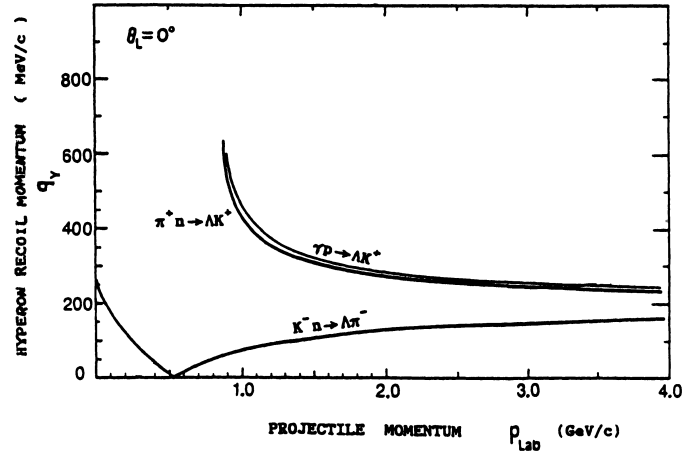


Figure 1.2: Kinematics of the reactions (1.1), (1.2) and photoproduction for forward Λ emission ($\theta_L=0^\circ$). The momentum transferred to the hyperon is plotted as a function of the incoming particle (K^- , π^+ or e) in the Laboratory system.

However, the most important parameter in determining the selectivity of the different reactions is the momentum transfer. Fig. 1.2 shows the momentum transferred to the Λ hyperon, q_Λ , as a function of the momentum of the projectile in the laboratory frame, p_{Lab} , for reactions (1.1) and (1.2), as well as for photoproduction at $\theta_{Lab} = 0^\circ$.

A striking kinematical difference appears: for (1.1), which is exoenergetic, there is a value of p_{Lab} (505 MeV/c, called also “the magic momentum” [5]) for which q_Λ vanishes and recoilless production takes place; for (1.2), which is endoenergetic, q_Λ decreases monotonically with p_{Lab} , staying always at values exceeding 200 MeV/c. A further degree of freedom in selecting q_Λ is given by the detection angle of the produced meson. It is also quite interesting to notice that q_Λ for (1.1) with K^- at rest is of the same order of magnitude as for (1.2).

In order to get insight on how the features of the elementary reaction affect the production of Hypernuclei in well defined states the impulse ap-

proximation may be used. The two-body reaction t -matrix in the nuclear medium is replaced by the free-space t -matrix at the same incident momentum and the differential cross-section for the reaction:

$$\left. \begin{array}{l} K^- \\ \pi^+ \end{array} \right\} + {}^A_Z \rightarrow {}^A_{\Lambda}Z + \left\{ \begin{array}{l} \pi^- \\ K^+ \end{array} \right. \quad (1.5)$$

may be written as

$$d\sigma(\theta)/d\Omega_L = \xi [d\sigma(\theta)/d\Omega_L]_{\text{free}} N_{\text{eff}}(i \rightarrow f, \theta). \quad (1.6)$$

In (1.6) $d\sigma(\theta)/d\Omega_L$ is the laboratory cross-section for the production of the Hypernucleus ${}^A_{\Lambda}Z$ in a given final state f , ξ a kinematic factor arising from two-body to many-body frame transformation, $[d\sigma(\theta)/d\Omega_L]_{\text{free}}$ the cross section for the elementary (or free) reactions (1.1) and (1.2) and $N_{\text{eff}}(i \rightarrow f, \theta)$ the so-called “effective nucleon number”.

Eq. (1.6), quite simple and understandable at first sight, was used by Bonazzola *et al.* [6] for the first time to describe the production of Λ -hypernuclei by the (K^-, π^-) reaction in flight. All the complications and difficulties related to the many-body strong interaction system are obviously contained in the term $N_{\text{eff}}(i \rightarrow f, \theta)$ (the Nuclear Physics “black box”). In the simplest plane wave approximation (PWA) $N_{\text{eff}}(i \rightarrow f, \theta)$ can be furthermore written as

$$N_{\text{eff}}(i \rightarrow f, \theta) = (\text{Clebsch} - \text{Gordan coefficients}) \times F(q), \quad (1.7)$$

in which $F(q)$ is a form factor. It is possible to see in the frame of the Independent Particle Model that $F(q)$ is related to q by simple relationships.

Eqs. (1.6), (1.7) provide the essential features of reactions like (1.5) and corroborate the statement that the momentum transfer is the most important parameter determining the Hypernuclei production.

PWA is only a rough approximation for describing Hypernuclei production reactions and is unable to provide reliable values of the cross sections. A better insight is given by the Distorted Wave Impulse Approximation (DWIA). The K and π distorted waves are calculated separately by solving the Klein-Gordon equation with the use of appropriate optical potentials.

The meson potentials are conventionally taken to be proportional to the nucleon density. In its simplest form, DWIA is applied without inclusion of spin, neglecting multi-step processes (such as intermediate Σ production), and including off-shell effects. However, in order to apply DWIA, one must have knowledge of the elementary amplitudes for hyperon production, which is in general not well known.

DWIA calculations are quite successful in describing the shape of the angular distribution as well as the absolute value of the cross section (within $\sim 25\%$) and are generally used to determine the spin of the produced Hypernuclear final states. The DWIA approximates the production process, assuming that an incident projectile interacts with a nucleon in a specific, single-particle nuclear state, producing a hyperon which is then deposited in a specific, single particle hyperon state. In this formalism both the production and the spectra of hypernuclei can be considered in term of (particle, hole) states. Here a "hole" represents the removal of a nucleon from a nuclear states and is written as a "hole" wave function coupled to the nuclear core. The "hole" has the quantum number of the nucleon which was removed. This is a further explanation of the strong influence of the reaction kinematic on the hypernuclear production.

Similar theoretical considerations may be applied also for describing the electroproduction of Hypernuclei by means of the elementary reaction (1.3), even though the relevant expressions are somehow complicated by the three-body final state kinematics and by the dynamics described by the electromagnetic interaction. The relevant relationships can be found, e.g., in [7] and [8].

It appears that, with the (K^-, π^-) reactions in flight, substitutional states of the Hypernucleus in which a neutron of the target nucleus is converted into a Λ hyperon in the same orbit with no orbital angular momentum transfer are preferentially populated. On the other hand the (π^+, K^+) and $(e, e'K^+)$ reactions, and also the (K^-, π^-) reaction at rest transfer a significant (200-300 MeV/c) recoil momentum to the Hypernucleus, and then several high spin hypernuclear states are simultaneously produced. This feature is of paramount importance for Hypernuclear Spectroscopy studies and also for investigations on the Weak Decay, which occurs mainly for Hypernuclei in

the ground state. Furthermore, since the spin-flip amplitudes in reactions (1.1) and (1.2) are generally small, they populate mainly non spin-flip states of Hypernuclei. On the contrary, since the amplitude for reaction (1.3) has a sizable spin-flip component even at zero degrees due to the spin 1 of the photon, both spin-flip and non spin-flip final Hypernuclear states may be populated in electroproduction. From the above considerations it appears that in principle we have at disposal all the tools needed for a complete study of all the Hypernuclei we wish to study. In practice the experimenters have to face many other constraints in designing their detectors. They are:

1. the values of the cross sections for producing Hypernuclei with reactions (1.1), (1.2) and (1.3)
2. the presence of physical backgrounds in which the signals due to Hypernuclei's formation could be blurred
3. the intensity and energy resolution of the beams of projectiles (K^- , π^+ , e)
4. the availability of the above beams at the different Laboratories, in competition with other experiments in Nuclear and Particle Physics.

A simple answer to question 1 is given by Fig.1.3

It must be noticed that the production of Hypernuclei by means of the (K^- , π) reaction with K^- at rest is reported too on a cross-section scale, which is formally wrong since the production by particles at rest is defined by a capture rate and not by a cross section. This information is inserted on the plot, with a suitable normalization on similar reactions. Unfortunately the intensities and the qualities of the beams scale inversely to the values of the production cross-sections. The electron beams were always excellent concerning the intensity and the energy resolution. Unfortunately in the past years the duty cycle of the machines was very low, and the smallness of the cross section joined to the need of measuring the e^- and K^+ from (1.3) in coincidence did not allow to study the production of Hypernuclei. Only the advent of TJNAF, a machine with an excellent duty cycle, allowed the

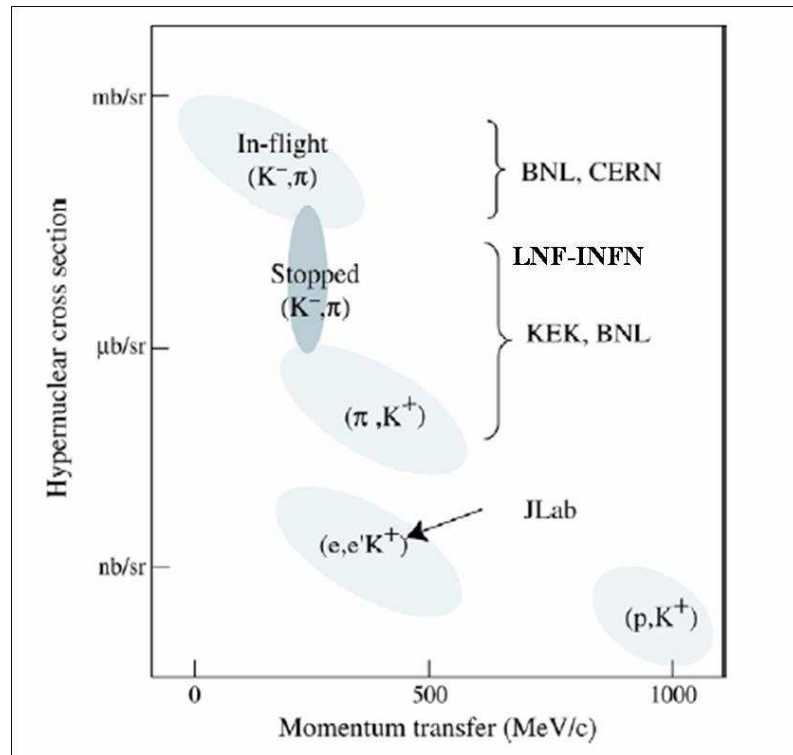
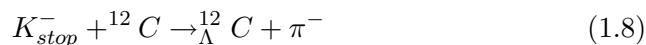


Figure 1.3: Hypernuclear production cross section for typical reactions versus momentum transfer.

start up of experiments on Hypernuclei. The best projectiles for producing Hypernuclei, and in general Strange Nuclei, are K^- . Unfortunately the intensity of such secondary beams is quite low, and even worse the quality (contamination by π^- , energy spread). For these reasons the magnetic spectrometers that were designed were quite complicated and the running times needed to obtain adequate statistics long. The powerful complex of machines J-PARC, that will be operational in two years, and for which Strange Nuclei and Atoms Physics will be one of the top priorities, will allow a real breakthrough in this field. Production of Hypernuclei by pion beams is midway concerning both the cross sections and the quality of the beams. For these reasons experiments using reaction (1.2) performed mostly at KEK with the SKS spectrometer produced the major part of experimental information in the last ten years by means of advanced state-of-art technologies at an old machine, the KEK 12 GeV ProtonSynchrotron. Overviews of the measurements done with the SKS can be found in Ref. [8]. A special discussion must be given in relation to the use of the (K^-, π^-) reaction at rest. This method seems the easier to exploit, since no experimental information on the momentum of the incoming particle is needed. Taking again as example the production of ${}_{\Lambda}^{12}\text{C}$ from a ${}^{12}\text{C}$ target with reaction (1.1) with K^- at rest:



at first sight one could think that the simple spectroscopy of the π^- coming from the hypernucleus formation should be enough to get information on the excitation spectrum of ${}_{\Lambda}^{12}\text{C}$. The fastest π^- should be those related to the formation of ${}_{\Lambda}^{12}\text{C}$ in the ground state. Unfortunately other processes following the capture of K^- at rest produce π^- with momenta even larger than those from reactions like (1.8). The more dangerous for hypernuclear spectroscopy is the capture of a K^- by a correlated (np) pair in the nucleus:



followed by the decay in flight of the Σ^- into $\pi^- + n$. This process leads to the production of π^- with a flat momentum spectrum extended beyond the kinematical limit due to the two-body production of Hypernuclei. This

drawback was clearly understood in the first series of experiments on Hypernuclei with K^- at rest performed at KEK laboratory.

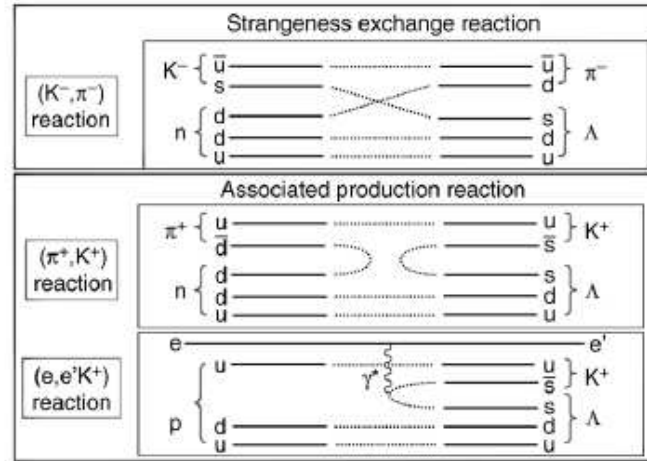


Figure 1.4: A schematic presentation of three strangeness producing reactions used to study hypernuclei.

1.3 Strangeness exchange production

In the (K^-, π^-) production reaction the incident K^- transforms the struck neutron into a Λ or Σ and a π^- is emitted with an energy spectrum which is directly related to the populated hypernuclear levels. *kaon* absorption generally leads to a Σ rather than a Λ hyperon, but the Σ and the Λ production are clearly distinguishable due to the different momentum of the emitted *pion*. The (K^-, π^0) reaction leads to neutral particles in the final states, making the experimental observation really hard, so I will focus on the (K^-, π^-) reaction. Depending on the momentum of the incident kaon we can have the *In-flight* reaction production or the *production with K^- at rest*. These two processes differ both in branching ratio for hyperon production and in kinematics.

1.3.1 In flight production

The in-flight (K^-, π^-) reaction was not the first used for hypernuclear production, but it was the reaction that introduced the modern era of accelerator-based investigations using magnetic spectrometers and electronic counters. In the early 1970's it was recognized that the incident momentum in the $n(K^-, \pi^-)\Lambda$ reaction could be chosen so that the momentum transferred to Λ could be zero and at the same time, separated beams of kaons at approximately 750 MeV/c could provide a maximum on the elementary cross-section. Thus a series of experiments using the in-flight (K^-, π^-) reaction was initiated at CERN and then at BNL. The spectra of light hypernuclei show peaks for substitutional states (a neutron replaced with a Λ with the same quantum number) for states near the nuclear surface.

This occurs because the strong nuclear absorption limits the K^- penetration of the nucleus, and the reaction has approximately zero angular momentum transfer. Thus, as the nuclear radius increases, the excitation of the core states decreases. In addition, the reaction yield to specific states also decreases with A , because for a given target thickness in g/cm^2 the number of target nuclei decreases with the first power of A , while the cross-section increases only as $A^{2/3}$, resulting in an overall decrease in strength of $A^{1/3}$. Since the Λ spin is 1/2, a substitutional state in which the hyperon simply takes the place of the nucleon involved in the production reaction is the only way to preserve the angular momentum. For this reason the production of hypernuclei in the ground state is practically impossible with this method.

Some results obtained with this method [9] are shown in Fig.1.5. Kaon momentum was (390 ± 8) MeV/c and π^- were detected in the forward direction; the Λ was almost at rest ($p_\Lambda \leq 80$ MeV/c). The collected statistics is very low, nevertheless these are still today the best published results concerning the ^{27}Al target.

1.3.2 Production with K^- at rest

Before separated beamlines, the ($K^-_{stopped}, \pi^-$) reaction was extensively used to produce hypernuclei. The stopped reaction proceeds when a kaon is absorbed from an atomic orbit into the nucleus. X-ray measurements of kaon

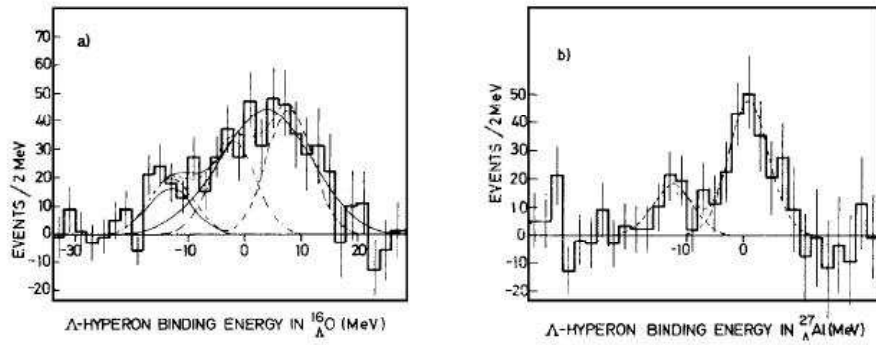


Figure 1.5: Excitation spectrum of ${}^{16}_{\Lambda}\text{O}$ (on left) and ${}^{27}_{\Lambda}\text{Al}$ (on right).

absorption on ${}^{12}\text{C}$, for example, indicate that 20% of all the kaons are captured from $3d$ orbits, while the remaining 80% are believed to be captured from low angular momentum, $l=0$ or 1.

During capture, a Λ is produced by the reaction $K^- + \mathcal{N} \rightarrow \Lambda + \pi$. Kaon absorption at rest provides momentum transfer approximately equal to Fermi momentum of a bound Λ (250 MeV/c) allowing the production of hypernuclear states in which a large variation of the angular momentum is involved. Furthermore that hypernucleus is formed without breaking the original nucleus. The Λ hypernucleus binding energy B_{Λ} can be defined as:

$$B_{\Lambda} = m_{core} + m_{\Lambda} - m_{hyp} \quad (1.10)$$

where

- $m_{core} = m_{(A-1)Z}$: mass of the nuclear core
- m_{Λ} : Λ hyperon mass
- $m_{hyp} = m_{(A-1)Z}^{\Lambda}$: measured mass of the produced hypernucleus

m_{core} and m_{Λ} are known quantities, so we only need to measure m_{hyp} . If we consider the (K_{stop}^-, π^-) reaction since both the kaons and the target nucleus are at rest, by applying the energy conservation, we obtain the following relation:

$$m_{targ} + m_{K^-} = \sqrt{m_{hyp}^2 + p_{hyp}^2} + \sqrt{m_{\pi^-}^2 + p_{\pi^-}^2} = \sqrt{m_{hyp}^2 + p_{\pi^-}^2} + E_{\pi^-} \quad (1.11)$$

where

- $m_{targ} = m_{AZ}$: mass of the target nucleus
- $p_{hyp} = p_{\Lambda^{(A-1)}Z}$: momentum transferred to the produced hypernucleus

The momentum conservation implies that $p_{hyp} = p_{\pi^-}$ and the hypernucleus mass can be evaluated directly from the π^- momentum

$$m_{hyp} = \sqrt{(m_{targ} + m_{K^-} - E_{\pi^-})^2 - p_{\pi^-}^2} \quad (1.12)$$

The experimental measurement of p_{π^-} is the result of the analysis of the momentum spectrum of emitted π^- , which is the convolution of several spectra due to the different reactions. In fig.1.6 the expected inclusive π^- momentum spectrum from nuclear absorption of K^- at rest is shown (taking into account the contribution of each physical process).

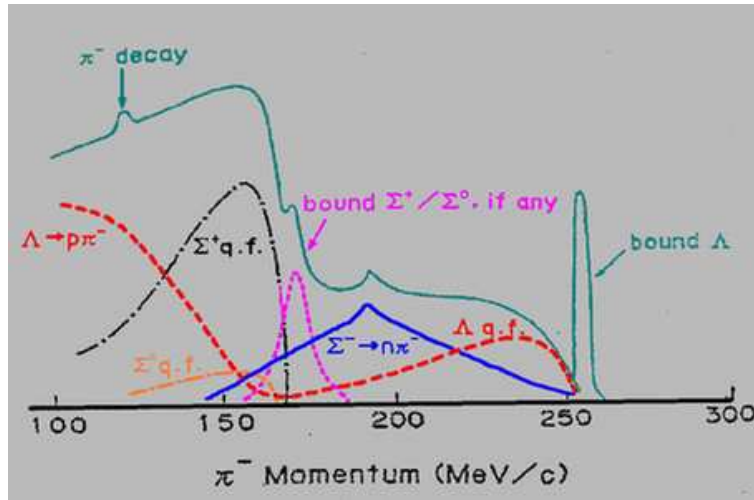


Figure 1.6: Theoretical spectrum: momentum of emitted π^- due to interaction between K_{stop}^- and nucleus [10].

Most recently a theoretical study of the in-medium modification of the KN interaction points out that the (K_{stop}^-, π^-) reaction can be used to better define the K^- optical potential at threshold. As previously discussed, the stopped reaction has higher momentum transfer than the in-flight reaction,

and is much less selective. In comparison the quasifree process is larger so it becomes difficult to resolve states near $B_\Lambda = 0$ due to this background. So the effectiveness of the reaction, particularly for the higher energy levels, is limited, even if the energy resolution is improved.

1.4 Associated production reaction

The (π^+, K^+) reaction was first exploited at the AGS in a series of investigations providing spectra across a wide range of hypernuclei, with typical resolution of 3-4 MeV. The reaction was then developed in detail at KEK with a dedicated beamline using a high resolution spectrometer, SKS, specifically built to detect the reaction kaons.

The associated production reaction has so far been the most productive of all hypernuclear reaction. While the cross section is lower than (K^-, π) reaction, the higher intensities of pion beams can more than compensate for this deficiency. More importantly, however, the selectivity of the reaction, and the penetrability of the projectiles allow the excitation of selected, deeply lying states. Counter experiments using magnetic spectrometers have generally provided hypernuclear spectra having energy resolutions ≥ 2 MeV. This is due to the intrinsic resolutions of secondary mesonic beam-lines, and to the target thickness required to obtain sufficient counting rates. The first excitation spectrum for the ^{89}Y was obtained at the AGS experiment through the (π^+, K^+) reaction (Fig.1.7), with a 4 MeV (FWHM) energy resolution.

A better result (Fig.1.8) was obtained at KEK by the E369 experiment. In this case the energy resolution is 1.65 MeV (FWHM).

The bump structures correspond to the orbital angular momentum of the major shells orbitals (s, p, d, f) in the bound region. The f orbital is split into two peaks. The presence of splitted levels for the p and the d orbitals is also suggested by this spectrum, due to the bumps width, which is significantly wider than the experimental resolution [12].

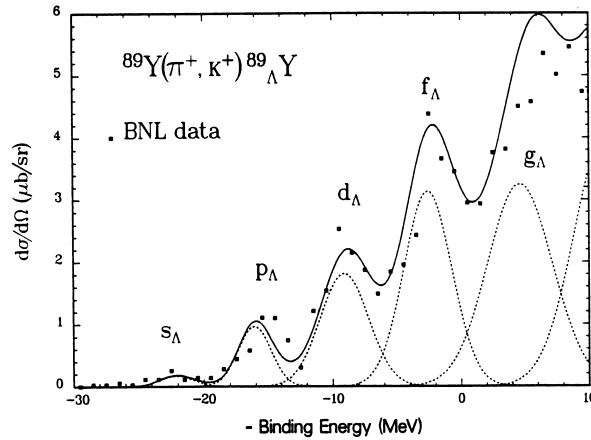


Figure 1.7: The excitation spectrum for the ${}^{89}\text{Y}(\pi^+, K^+)_{\Lambda}{}^{89}\text{Y}$ reaction at $p_{\pi} = 1.05 \text{ GeV}/c$ and $\theta_K = 10^\circ$, from the AGS experiment. The curves represent theoretical calculations. (From Ref. [11].)

1.5 Photoproduction reaction

Spectroscopy using electromagnetic probes is practical only by using the $(e, e'K^+)$ reaction since the yield rates and mass resolution necessary for spectroscopy cannot be achieved with real photon beams. An electron interacts with a target nucleus, emitting a virtual photon that hits a proton in the target and a hyperon and a kaon are associatively produced. A Λ hypernucleus is formed when the Λ hyperon is bound to the residual nuclear core with charge. In order to determine the hypernuclear mass experimentally, it is necessary to know the incident beam energy and to measure momenta of both the scattered electron and the kaon in coincidence.

The hypernuclear production cross section for the $(e, e'K^+)$ reaction can be expressed in terms of the elementary photo production process and the virtual photon flux.

From the experimental point of view, an important advantage of the $(e, e'K^+)$ reaction is that it has the potential to carry out hypernuclear reaction spectroscopy with sub-MeV mass resolution. A resolution of a few 100 keV can be achieved and will have great impact on hypernuclear reaction

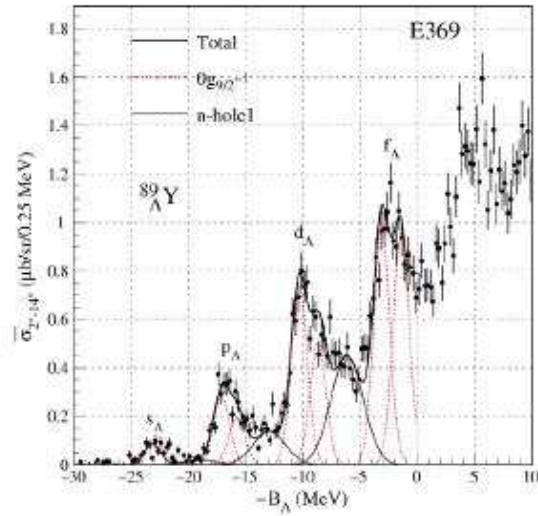


Figure 1.8: The excitation spectrum for the $^{89}\text{Y}(\pi^+, K^+)_{\Lambda}^{89}\text{Y}$ reaction obtained at KEK by E369 experiment [12]

spectroscopy. The expected resolution is comparable to spreading widths of hypernuclear states excited above the nucleon emission thresholds and to the excitation energies of many core excited states. Therefore, it becomes possible to identify a hyperon single-particle orbit more clearly, untangling core excited states.

Chapter 2

Weak Decay modes of Λ Hypernuclei

2.1 Introduction

A Λ hyperon, which carries out the 'strangeness' degree of freedom, can be used as a unique probe to investigate the interior of the nucleus since it does not suffer from Pauli's exclusion principle. In order to describe the structure of the hypernuclei the knowledge of the elementary hyperon-nucleon (YN) and hyperon-hyperon (YY) interactions is crucial.

Hyperon masses differ remarkably from the nucleonic mass, hence the flavour SU(3) symmetry is broken. The amount of this breaking is a fundamental question in order to understand the baryon-baryon interaction in the strangeness physics. Nowadays the knowledge of hypernuclear phenomena is rather good, but some open problems still remain. The study of this field may help in understanding some important question, related to:

- some aspects of the baryon-baryon weak interaction;
- the YN and YY strong interaction in the $J^P=1/2^+$ baryon octet;
- the possible existence of di-baryon particles;
- the renormalisation of hyperon and meson properties in the nuclear medium;

- the nuclear structure: for instance, the long standing question of the origin of the spin-orbit interaction and other aspects of the many-body nuclear dynamics;
- the role played by quark degrees of freedom, flavour symmetry and chiral models in nuclear and hypernuclear phenomena.

In particular the first item and the last one can be discussed and understood by investigating the hypernuclear weak decays.

The importance of such process was pointed out just at the first beginning of Hypernuclear Physics. As a matter of fact, Cheston and Primakov gave a quantitative discussion of the possibility that a Λ hyperon bound to nucleons might undergo non mesonic decay in 1953 [25]. In a nucleus the Λ can decay by emitting a nucleon and a pion (mesonic mode) as it happens in free space, but its weak interaction with the nucleons opens new channels indicated as non mesonic decay modes.

These are the dominant decay channels of medium-heavy nuclei ($A \geq 12$), where, on the contrary, the mesonic decay is disfavoured by Pauli blocking effect on the outgoing nucleon. In particular, one can distinguish between one-body and two-body induced decays, according whether the hyperon interacts with a single nucleon or with a pair of correlated nucleons.

2.2 Weak decay modes of Λ -Hypernuclei

Typical lifetimes for strong and electromagnetic interactions are much smaller than the ones for weak interaction, as shown in Tab. 2.1, then, even if a hypernucleus is formed in an excited state, it usually reaches its ground state by radiative processes before decaying through weak channels.

The two principal weak decay mechanisms inside a hypernucleus are [13]:

- **The mesonic weak decay**
- **The non-mesonic weak decay (NMWD)**

Interaction	Lifetime (s)
Strong	10^{-24}
Electromagnetic	10^{-16}
Weak	$10^{-10} \div 10^{-8}$

Table 2.1: Table of typical lifetimes for different interactions.

2.2.1 The mesonic decay

The mesonic mode is the main decay channel of a Λ in free space and it occurs following the processes described by:

$$\Lambda \rightarrow \pi^- p \quad (B.R. = 63.9 \times 10^{-2}) \quad (2.1)$$

$$\Lambda \rightarrow \pi^0 n \quad (B.R. = 35.8 \times 10^{-2}) \quad (2.2)$$

with a lifetime $\tau_{\Lambda}^{free} = \hbar / \Gamma_{\Lambda}^{free} = 2.632 \times 10^{-10}$ sec. Semi-leptonic and weak radiative Λ decay modes have negligible branching ratios:

$$\Lambda \rightarrow n\gamma \quad (B.R. = 1.75 \times 10^{-3}) \quad (2.3)$$

$$\Lambda \rightarrow p\pi^- \gamma \quad (B.R. = 8.4 \times 10^{-4}) \quad (2.4)$$

$$\Lambda \rightarrow pe^- \bar{\nu}_e \quad (B.R. = 8.32 \times 10^{-4}) \quad (2.5)$$

$$\Lambda \rightarrow p\mu^- \bar{\nu}_{\mu} \quad (B.R. = 1.57 \times 10^{-4}) \quad (2.6)$$

and will not be considered here.

The Λ hyperon is an isospin singlet ($I_{\Lambda} = 0$), while the πN system can be either in $I=1/2$ or in $I=3/2$ isospin states. The customary angular momentum coupling implies:

$$|\pi^- p\rangle = \sqrt{\frac{1}{3}} \left| \frac{3}{2}, -\frac{1}{2} \right\rangle - \sqrt{\frac{2}{3}} \left| \frac{1}{2}, -\frac{1}{2} \right\rangle \quad (2.7)$$

$$|\pi^0 n\rangle = \sqrt{\frac{2}{3}} \left| \frac{3}{2}, -\frac{1}{2} \right\rangle - \sqrt{\frac{1}{3}} \left| \frac{1}{2}, -\frac{1}{2} \right\rangle \quad (2.8)$$

Hence the ratio of amplitudes for $\Delta I = 1/2$ transitions yields:

$$\frac{\Gamma_{\Lambda \rightarrow \pi^- p}^{free}}{\Gamma_{\Lambda \rightarrow \pi^0 n}^{free}} \simeq \frac{|\langle \pi^- p | T_{1/2, -1/2} | \Lambda \rangle|^2}{|\langle \pi^0 n | T_{1/2, -1/2} | \Lambda \rangle|^2} = \left| \frac{\sqrt{2/3}}{\sqrt{1/3}} \right|^2 = 2 \quad (2.9)$$

while a $\Delta I = 3/2$ process should give:

$$\frac{\Gamma_{\Lambda \rightarrow \pi^- p}^{free}}{\Gamma_{\Lambda \rightarrow \pi^0 n}^{free}} \simeq \frac{|\langle \pi^- p | T_{3/2, -1/2} | \Lambda \rangle|^2}{|\langle \pi^0 n | T_{3/2, -1/2} | \Lambda \rangle|^2} = \left| \frac{\sqrt{1/3}}{\sqrt{2/3}} \right|^2 = \frac{1}{2} \quad (2.10)$$

Experimentally the above ratio turns out to be:

$$\left\{ \frac{\Gamma_{\Lambda \rightarrow \pi^- p}^{free}}{\Gamma_{\Lambda \rightarrow \pi^0 n}^{free}} \right\}^{Exp} \simeq 1.78 \quad (2.11)$$

which is close to 2 and strongly suggests the $\Delta I = 1/2$ rule on the isospin change. From the above considerations and from analysis of the Λ polarization observables it follows that the measured ratio between $\Delta I = 1/2$ and $\Delta I = 3/2$ transition amplitudes is very large:

$$\left| \frac{A_{1/2}}{A_{3/2}} \right| \simeq 30. \quad (2.12)$$

The $\Delta I = 1/2$ rule is based on experimental observations but its dynamical origin is not yet understood on theoretical grounds. It is also valid for the decay of the Σ hyperon and for pionic kaon decays (namely in non-leptonic strangeness-changing processes).

Actually, this rule is slightly violated in the Λ free decay, and it is not clear whether it is an universal characteristic of all non-leptonic processes with $\Delta S \neq 0$. The Q -value for free Λ mesonic decay at rest is

$$Q_{\Lambda} \simeq m_{\Lambda} - m_N - m_{\pi} \simeq 40 MeV. \quad (2.13)$$

Then taking into account energy-momentum conservation one has

$$m_{\Lambda} \simeq \sqrt{p_{\pi}^2 + m_{\pi}^2} + \sqrt{p_N^2 + m_N^2} \quad (2.14)$$

in the center-of-mass system and the momentum of the final nucleons turns out to be $p \simeq 100$ MeV. Inside a hypernucleus, the binding energies of the recoil nucleon and of the Λ tend to further decrease Q and hence p .

As a consequence, in nuclei the mesonic decay is disfavoured by the Pauli principle, particularly in heavy systems. It is strictly forbidden in normal infinite nuclear matter (where the Fermi momentum is $k_F^0 \simeq 270$ MeV), while in finite nuclei it can occur because of three important effects:

1. In nuclei the hyperon has a momentum distribution (being confined in a limited spatial region) that allows larger momenta to be available to the final nucleon;
2. The final pion feels an attraction by the medium such that for fixed momentum q it has an energy smaller than the free one and consequently, due to energy conservation, the final nucleon again has more chance to come out above the Fermi surface.

Indeed it has been shown [14][15] that the pion distortion increases the mesonic width by one or two orders of magnitude for very heavy hypernuclei ($A \simeq 200$) with respect to the value obtained without the medium distortion;

3. At the nuclear surface the local Fermi momentum is considerably smaller than k_F^0 , and the Pauli blocking is less effective in forbidding the decay.

In any case the mesonic width rapidly decreases as the nuclear mass number A of the hypernucleus increases.

Even though the Λ particle has a lifetime of the order of 10^{-10} s due to its stability against strong interaction, it is still so difficult to perform ΛN scattering experiments that the amount and accuracy of the data are limited. Therefore, to produce Λ hypernuclei and to investigate their structure has been the most practical approach to study the Λ -N interaction.

In the calculation starting from the realistic ΛN two-body interaction, the existence of a central repulsion in the hyperon-nucleus potential has been discussed by many authors. The strength of long-range attraction of the YN interaction is much weaker than that of the NN interaction and it is

almost counterbalanced by the short-range repulsion. Reflecting this situation, there remains inner repulsion also in the hyperon-nucleus potential which is constructed from the YN interaction using the folding procedure. This effect can be experimentally detected most distinctly in the case of very light ($A=4-5$) hypernuclear systems. A hyperon is pushed outward from a core nucleus due to this repulsion. Consequently, the overlap of the wave function of the hyperon with the nucleus is considered to be much reduced. The π -mesonic decay of hypernuclei, as said, undergoes Pauli suppression and the mesonic decay rate is thus sensitive to the extent of the overlap between the wave functions of Λ and core nucleus, which reflects the potential shape felt by Λ in nuclei. If the mesonic decay rate can be precisely measured, it is expected to be an essential complement of knowledge of the Λ single particle potential, the shape of which cannot be investigated from the Λ binding energy. Accurate measurements of the π -mesonic decay width of light s -shell Λ hypernuclei were performed at KEK with the SKS spectrometer in E462 experiment [20] and the existence of a inner repulsive core was established [16]–[19].

2.2.2 The non mesonic decay

In hypernuclei the weak decay can occur through processes which involve a weak interaction of the Λ with one or more nucleons. Sticking to the weak hadronic vertex $\Lambda \rightarrow \pi N$, when the emitted pion is virtual, then it will be absorbed by the nuclear medium, resulting in a non-mesonic process of the following type:

$$\Lambda n \rightarrow nn \quad (\Gamma_n), \quad (2.15)$$

$$\Lambda p \rightarrow np \quad (\Gamma_p), \quad (2.16)$$

$$\Lambda NN \rightarrow nNN \quad (\Gamma_2), \quad (2.17)$$

The total weak decay rate of a Λ -hypernucleus is then:

$$\Gamma_T = \Gamma_M + \Gamma_{NM} \quad (2.18)$$

where Γ_M and Γ_{NM} indicate, respectively, the mesonic and non mesonic decay widths and can be written as:

$$\Gamma_M = \Gamma_{\pi^-} + \Gamma_{\pi^0} \quad (2.19)$$

$$\Gamma_{NM} = \Gamma_1 + \Gamma_2 \quad (2.20)$$

$$\Gamma_1 = \Gamma_n + \Gamma_p \quad (2.21)$$

and the lifetime is $\tau = \hbar / \Gamma_T$. The channel (2.17) can be interpreted by assuming that the pion is absorbed by a pair of nucleons, correlated by the strong interaction. This term, often referred as "two-nucleon-induced decay" has been proposed in addition to the two-body reaction $\Lambda + \mathcal{N} \rightarrow \mathcal{N} + \mathcal{N}$ by theoretical considerations [65], but a convincing experimental evidence has not yet been put forward. Obviously, the non-mesonic processes can also be mediated by the exchange of more massive mesons than the pion as shown in Fig. 2.1

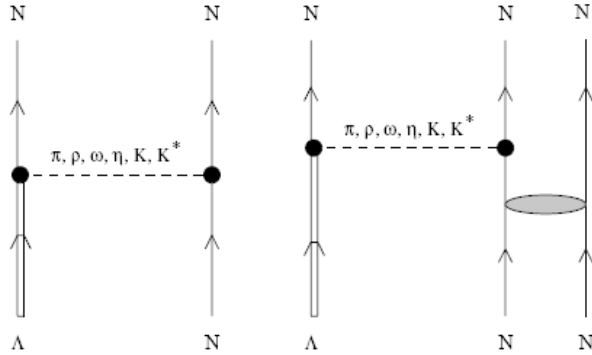


Figure 2.1: One nucleon (on left) and two-nucleons (on right) induced Λ decay in nuclei

The non-mesonic mode is only possible in nuclei and, nowadays, the systematic study of the hypernuclear decay is the only practical way to get information on the weak process $\Lambda N \rightarrow NN$ (which provides the first extension of the weak $\Delta S=0$ $NN \rightarrow NN$ interaction to strange baryons), especially on its parity-conserving part, which is masked by the strong interaction in the weak $NN \rightarrow NN$ reaction.

The final nucleons in the non-mesonic processes are emitted with large momenta: disregarding the Λ and nucleon binding energies and assuming the available energy $Q = m_\Lambda - m_N \simeq 176$ MeV to be equally splitted among the final nucleons, it turns out that $p_N \simeq 420$ MeV for the one-nucleon induced channels (Eqs 2.15 and 2.16) and $p_N \simeq 340$ MeV in the case of the two-nucleon induced mechanism (Eq.2.17).

Therefore, the non-mesonic decay mode is not forbidden by the Pauli principle: on the contrary, the final nucleons have great probability to escape from the nucleus. The non-mesonic mechanism dominates over the mesonic mode for all but the s-shell hypernuclei. Only for very light systems the two decay modes are competitive.

2.3 Theoretical Models

Several theoretical models have been developed in order to explain the weak decay mechanism of Λ hypernuclei ; the main differences between these models must be referred to the nature of the exchange potential.

The first calculations of the mesonic rate for light hypernuclei date at the end of the 50's [24]. The Pauli blocking effect for nuclear decay was estimated and used in order to assign the spin to the ground state of s-shell hypernuclei. As mentioned in Sec 2.1. the possibility of non-mesonic hypernuclear decay was suggested for the first time in 1953 [25] and interpreted in terms of the free space $\Lambda \rightarrow N\pi$ decay, where the pion was considered as virtual and then absorbed by a bound nucleon.

In the 60's Block and Dalitz [26] [27] developed a phenomenological model, which has been more recently updated [28] [29]. Within this approach, some important characteristics of the non-mesonic decays (for instance the validity of the $\Delta I = 1/2$ rule) of s-shell hypernuclei can be reproduced in terms of elementary spin-dependent branching ratios for the $\Lambda n \rightarrow nn$ and $\Lambda p \rightarrow np$ processes, by fitting the available experimental data.

After the first analysis by Block and Dalitz, microscopic models of the $\Lambda N \rightarrow nN$ interaction began to be developed. The first of these models was the One-Pion-Exchange (OPE) model. The OPE model is based on the

$\Lambda N\pi$ weak vertex followed by the absorption of the virtual pion by a second nucleon of the nuclear medium. The results of the decay width calculation for the one nucleon induced NMWD were not realistic also because the employed $\Lambda N\pi$ coupling was too small to reproduce the Λ free lifetime.

Afterwards, in order to improve the OPE model, mesons heavier than the pion were introduced as mediators of the $\Lambda N \rightarrow NN$ interaction. McKellar and Gibson [30] evaluated the width for a Λ in nuclear matter, adding the exchange of the ρ -meson and taking into account ΛN relative s -states only. They calculated the $\Lambda N\rho$ weak vertex assuming the $\Delta I = 1/2$ rule and made the calculation by using the two possible relative signs (being at the time unknown and not fixed by their model) between the pion and ρ potentials. It is important to note that for mesons heavier than the pion, no experimental indication supports the validity of the $\Delta I = 1/2$ rule for their couplings with baryons [31]. Some years later, Nardulli [32] determined the relative sign (-) between ρ and π exchange implementing the available information from weak non-leptonic and radiative decays. Refs.[30] [32] obtained a non-mesonic width in the $(\rho+\pi)$ exchange model smaller than the OPE one.

In 1986 Dubach *et al.* [33] extended the OPE model to the more complete OME (One Meson Exchange), in which different exchanged mesons (π , ρ , K , K^* , ω and η) were considered. For most of the OME calculation the $\Delta I = 1/2$ rule was assumed for the meson coupling with baryons. This assumption is justified for the $\Lambda N\pi$ weak vertex, but there is no experimental evidence to assume it for other vertices like $\Lambda N\rho$ which is not accessible experimentally.

Another theoretical approach to the short-range nature of the ΛN weak interaction is the quark current interaction model. Cheung, Heddele and Kisslinger [34][35] considered the hybrid quark hadron model for the non-mesonic decay. In this model the decay is explained by two separate mechanisms which have different interaction range: the long-range term ($r \geq 0.8$ fm) was described by OPE with $\Delta I = 1/2$ rule, whereas the short range interaction was described by a six-quark cluster model including both $\Delta I = 1/2$ and $\Delta I = 3/2$ contribution.

More recently Inoue *et al.* calculated the non mesonic decay width with a direct quark (DQ) model [36][37] where a four-quark interaction between

the constituent quarks of baryons caused the transition without exchanging mesons. The four-quark vertex was obtained from the low-energy effective Hamiltonian in the perturbative QCD theory which contains both $\Delta I = 1/2$ and $\Delta I = 3/2$ transitions. Those authors stressed that the DQ mechanism gives a significant $\Delta I = 3/2$ contribution in the $l=0$ channel. This model was further extended to combine with the OME calculation [38] in order to take into account the long-range interaction which is not included in the DQ mechanism.

All these theoretical efforts done in the last years were devoted to the solution of an important question concerning the weak decay rates. In fact the study of the NMWD was characterized by a longstanding disagreement between theoretical estimates and experimental determinations of the ratio Γ_n/Γ_p between the neutron- and the proton-induced decay widths.

It is worth recalling here that, up to short time ago, all theoretical calculations appeared to strongly underestimate the available central data measured in several hypernuclei:

$$\left\{ \frac{\Gamma_n}{\Gamma_p} \right\}^{Theory} \ll \left\{ \frac{\Gamma_n}{\Gamma_p} \right\}^{Exp}, 0.5 \leq \left\{ \frac{\Gamma_n}{\Gamma_p} \right\}^{Exp} \leq 2 \quad (2.22)$$

Nowadays it seems that hypernuclear physics is going toward a solution of the Γ_n/Γ_p puzzle in the non mesonic weak decay thanks also to the inclusion in the $\Lambda N \rightarrow nN$ transition potential of mesons heavier than the pion, the inclusion of interaction terms that explicitly violate the $\Delta I = 1/2$ rule and the description of the short range baryon-baryon interaction in terms of quark degrees of freedom, which automatically introduces $\Delta I = 3/2$ contributions.

In the next section the partial agreement obtained between the theoretical predictions and the experimental data is described.

2.4 Experimental results

Since the non-mesonic channel is characterized by a large momentum transfer, the details of the hypernuclear structure do not have a substantial influence (then providing useful information directly on the hadronic weak

interaction). On the other hand, the NN and Λ N short range correlations turn out to be very important.

In fact the large momentum transfer in non-mesonic decay processes implies that they probe short distances and might, therefore, elucidate the rôle of explicit quark/gluon substructure of the baryons. Furthermore, the fundamental question as to whether the $\Delta I = 1/2$ rule, which governs pionic decay, applies to the non-mesonic weak decays may also be addressed.

Recent review papers on this topic are due to Alberico and Garbarino [13] and to Ota [21]. The first observable that can be measured is the lifetime τ_Λ of a given hypernucleus for weak decay, otherwise referred as the lifetime of Λ in nuclei. Recently measurements of τ_Λ of reasonable quality (errors of $\sim 10\%$) were performed [3] [63] [64] and the results are summarized by Fig 2.2 .

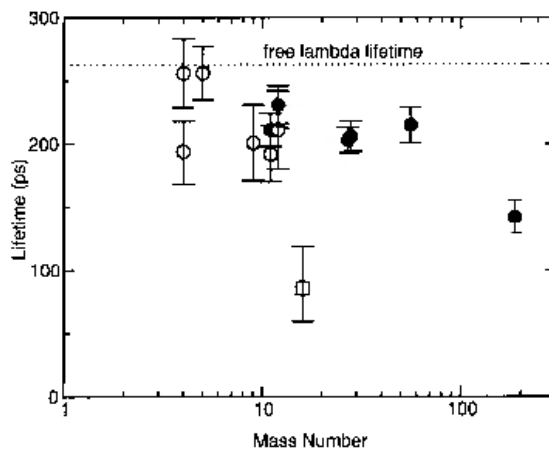


Figure 2.2: Lifetime of the Λ -hyperon as measured for several Λ -hypernuclei.

It should be noticed that all the experimental data points show a smoothly decreasing behaviour as a function of the mass number A , with the exception of the value for ^{16}O and that for the heavier targets (Bi, U). Whereas for all the experiments in agreement the hypernuclei were produced by means of reactions (1.1) and (1.2), the experiment on $^{16}_\Lambda\text{O}$ was performed using a beam of relativistic ^{16}O ions and that on the heavier targets by means of

delayed fission induced by protons.

The datum on ${}_{\Lambda}^{16}\text{O}$ is very likely affected by some experimental drawback, the datum for the heavy targets is quite recent and the experiment was carefully done. The conclusion is that for the medium A hypernuclei τ_{Λ} is about 80% that of the free Λ , falling at about 50% for the heaviest targets. Based on the results of lifetime measurements and mesonic decay branching ratio in the mass number range of $12 \leq A \leq 56$, the mass number dependence of the non-mesonic decay widths is plotted in Fig. 2.3

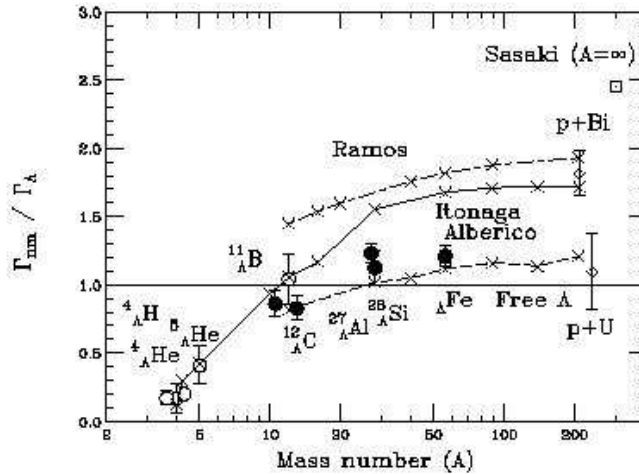


Figure 2.3: Total non mesonic decay widths of Λ -hypernuclei. For details see the text.

Closed circles are the data in E307 [45] and the open circles are previous experimental data in which the hypernuclear production was explicitly identified. The open diamonds are experimental data of lifetimes measurements for very heavy hypernuclei in the mass region of $A \sim 200$ with recoil shadow method on $p + \text{Bi}$ and $p + \text{U}$ reactions at COSY in which the production of strangeness was not explicitly identified. The plotted data around $A \sim 200$ in Fig. 2.3 were the ones converted from the results of lifetimes measurements, assuming that non mesonic decay occurs in heavy Λ -hypernuclei.

The solid line is a calculation by Itonaga et al. [39]. The dash-dotted line is a calculation by Ramos et al. [67] based on one-pion exchange potential in which the vertex renormalization effect in the nuclear medium and the

local density approximation are taken into account. Their results of the non mesonic decay widths are much larger than the experimental results and do not seem to saturate around $A = 56$. The dashed line is a calculation by Alberico et al. [68] (1N-induced decay only included); they updated Ramos calculation and obtained results closer to the present data by adjusting the Landau-Migdal parameter, which controls the short-range part of the pion potential. The open square shows a result with the direct quark exchange model in nuclear medium by Sasaki et al. [38].

As said, up to very recent times, the main challenge of hypernuclear weak decay studies has been to provide a theoretical explanation of the large experimental values for the ratio Γ_n/Γ_p between the neutron- and the proton-induced decay widths. Until recently, the large uncertainties involved in the extraction of the ratio from data did not allow to reach any definitive conclusion. The data were quite limited and not precise due to the difficulty of detecting the products of the non-mesonic decays, especially the neutrons. In Fig. 2.4 the Γ_n/Γ_p ratio of Λ -hypernuclei as function of the mass number A is reported.

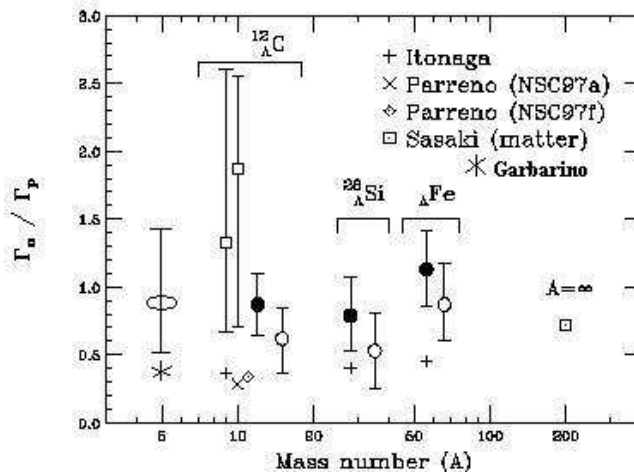


Figure 2.4: The Γ_n/Γ_p ratio of Λ -hypernuclei.

The closed and open circles are the results of the E307 experiment [45], assuming the "1N only" and "1N and 2N" processes, respectively. The open squares are previous experimental data by Szymanski et al. [42] and Noumi

et al. [43]. The experimental data on ${}^5_{\Lambda}He$ were obtained with SKS spectrometer at E307 experiment [45].

Theoretical calculations by Itonaga [39], Parreno [95], Sasaki [38] and Garbarino [100] are plotted in the same figure.

The direct quark current exchange model (DQ) was applied to explain the very short-range part of the non mesonic decay in light Λ -hypernuclei and nuclear matter, incorporating it with the contribution of π and K meson exchanges. Systematic studies were performed about various combinations of meson exchange potentials. It was also pointed out that two-nucleon induced non mesonic decay could play an important role in the non mesonic weak decay even if no experiment has so far explicitly measured the contribution of the two-nucleon process. The results of the non mesonic decay widths and the Γ_n/Γ_p ratios provide good criteria to test the short-range nature of the non mesonic decay, which is essentially important to understand its mechanism.

However, as shown in Fig. 2.3 and 2.4, there is no theoretical calculation that explains both the nonmesonic decay width and the Γ_n/Γ_p ratio consistently.

For instance, the quark-current exchange model gives the Γ_n/Γ_p ratio in nuclear matter comparable to the present experimental data, but overestimates the nonmesonic decay width. The conventional meson exchange models, in which the contribution of heavy mesons is included, provide larger Γ_n/Γ_p ratios than those by the one-pion exchange model, though the results of meson exchange models are still smaller than the experimental data.

As said among the mechanisms explored to remedy the puzzle, direct quark model approaches have been adopted [38] and the results of these calculations, which yield a large violation of the $\Delta I = 1/2$ rule, provide, on the contrary, significant larger values for the ratio $\Gamma_n/\Gamma_p \sim 0.4$. A similar experimental value of 0.4, though still affected by considerably high errors ($\sim 20\%$), was reported by very recent measurements at KEK, in which nucleon spectra in coincidence with the K^+ corresponding to the formation of the hypernucleus in the ground state produced by the (π^+, K^+) reaction were reported. Impressive, for the quality of the data, not for the statistics, are the data reported by Ref. [72] [73] and [74] for ${}^5_{\Lambda}He$ and ${}^{12}_{\Lambda}C$, in which

the spectra of both nucleons in coincidence were measured, applying also an angular correlation (quasi back-to-back) cut in order to eliminate events in which one of the nucleons suffered a final state interaction. Fig 2.5 shows the final experimental results for ${}^5_{\Lambda}He$ hypernucleus.

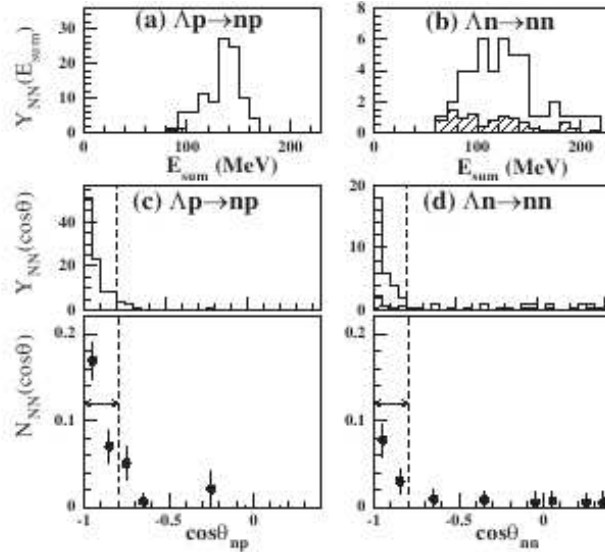


Figure 2.5: (a),(b): the yields of the np and nn coincidence events as a function of the energy sum of the pair nucleons. (c),(d): The upper panel shows the yields of the NN coincidence events plotted as function of the opening angle between the two nucleons. The lower panel depicts the normalized yields of the np and nn coincidence per NMWD.

Errors are still very large and the threshold on detection for proton is still quite high, avoiding a very precise comparison with theory. These circumstances did not allow to determine the decay width of the two-body process $\Gamma_2: \Lambda + (\mathcal{N}\mathcal{N}) = n + \mathcal{N} + \mathcal{N}$, which is predicted to amount up to $\sim 15\%$ of the total decay width [13].

More puzzling is still the situation concerning the nucleon spectra emitted in the non-mesonic weak decays, in particular those relative to the protons. An interesting series of measurements was recently performed by the SKS Collaboration [72] [74] [48], and the final results are summarised by Fig. 2.6. The proton spectra have a low energy cut at 35 MeV, due to the use

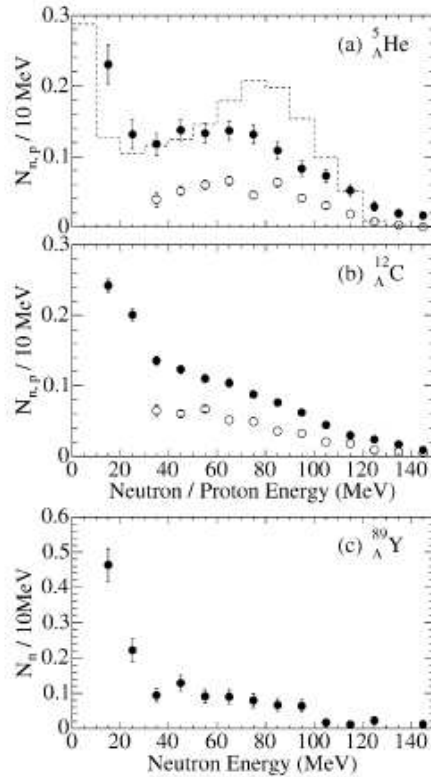


Figure 2.6: Neutron (filled circle) and proton (open circle) energy spectra per NMWD of (a) ${}^5_{\Lambda}\text{He}$ and (b) ${}^{12}_{\Lambda}\text{C}$ with the neutron spectrum of (c) ${}^{89}_{\Lambda}\text{Y}$. The errors are statistical. The dashed histogram in the top figure shows the the neutron spectrum per NMWD calculated by Garbarino et al. [100] in which FSI effect and the 2N-induced process were taken into account.

of quite thick targets in order to increase the counting rates. Obviously the neutron spectra did not suffer from such a drawback. All the measured nucleon spectra exhibit a smooth behaviour, without memory of an expected enhancement around 80 MeV, the energy of the nucleons from NMWD.

This effect is visible even for the light Hypernucleus ${}^5_{\Lambda}\text{He}$. The experimental spectrum does not agree with the spectrum calculated by Garbarino et al. [100], who takes into account both Final State Interactions and two-nucleon induced NMWDs. It is overlaid on the top of Fig.2.6 (dashed histogram) on the same scale. The observed spectrum was significantly different from the

calculated energy spectrum. The calculated spectrum still has its maximum at about $Q/2$, whereas the experimental spectrum levels off in the region from 20 to 80 MeV. The same authors calculate nucleon spectra emitted from heavier Hypernuclei, like ${}_{\Lambda}^{12}\text{C}$, in which the memory of the peak at 80 MeV is lost, due to the overwhelming effect of FSI.

The discrepancy between the theory and the experimental results on the proton spectra from the non mesonic weak decay mechanism suggests a more detailed study of this item and this is the subject of the present thesis.

Chapter 3

The FINUDA experiment

3.1 The DAΦNE collider

DAΦNE is an electron-positron collider operating at 1020 MeV energy in the centre of mass. The Φ meson (1.020 GeV) is produced by the annihilation of electrons and positrons, with an energy of 510 MeV each, circulating inside two separated rings which overlap in two straight sections as it can be seen in Fig.3.1. Electrons and positrons collide nearly head-on and the crossing angle can be varied between 10 and 25 mrad. The Φ particle main decay channels are:

$$\phi \rightarrow K^+K^- \quad (49.1 \pm 0.8)\%. \quad (3.1)$$

$$\phi \rightarrow K_S K_L \quad (34.1 \pm 0.6)\%. \quad (3.2)$$

$$\phi \rightarrow \rho\pi \rightarrow \pi^+\pi^-\pi^0 \quad (15.5 \pm 0.7)\%. \quad (3.3)$$

The DAΦNE collider design has been optimized in order to achieve high luminosity. This parameter is a typical figure of merit of a collider since it is proportional to the number of interactions available per unit of time. This quantity is given by the following expression:

$$L = NL_0 = Nf \frac{n_1 n_2}{4\pi\sigma_x\sigma_y}. \quad (3.4)$$

where L_0 is the single bunch luminosity and N is the total number of the stored bunches. n_1 and n_2 are the number of particles in the two bunches

which collides, f is the revolution frequency, and σ_x and σ_y are the bunch geometrical cross sections.

Considering the cross section of the $e^+ e^- \rightarrow \Phi$ process ($\sim 3.2 \mu\text{barn}$) and a typical integrated luminosity of $10\text{pb}^{-1}/\text{day}$, $\sim 170 (K^+, K^-)$ pairs per second are expected. Since the Φ is produced at rest the kaons are characterized by low momentum ($\sim 126 \text{ MeV}/c$) and high monochromaticity.

The DAΦNE collider consists of two almost circular rings that overlap in two straight sections (two interaction regions); electrons and positrons coming from the DAΦNE accumulator are injected separately in the two rings. The machine was designed in order to work in multi-bunches mode with a number of bunches up to 120. The geometrical parameters of the beam in the FINUDA interaction region are:

σ_x : 2mm;

σ_y : $20\mu\text{m}$;

σ_z : 30mm.

The length of each ring is $L \sim 100$ m and the duration of the single bunch is $\Delta t \sim 0.1\text{ns}$ (corresponding to a bunch length $\Delta s \sim 3\text{cm}$). The machine duty-cycle is $\sim 36\%$. The maximum value for the beam crossing frequency, set by the machine radiofrequency, is 368.25 MHz, then the minimum time interval between two contiguous bunches is about 2.72 ns.

beam energy range	(0.250 ÷ 0.750) GeV
$\theta/2$ (crossing angle)	(10 ÷ 25) mrad
single bunch luminosity	$4 \cdot 10^{30} \text{ cm}^{-2} \text{ s}^{-1}$
# of bunches per ring	(1 ÷ 120)
# of particles per bunch	$8.9 \cdot 10^{10}$
maximum design luminosity	$5 \cdot 10^{32} \text{ cm}^{-2} \text{ s}^{-1}$
crossing frequency	up to 368.25 MHz

Table 3.1: DAΦNE design values

The beam crossing angle leads to a boost outwards the main rings, thus changing the momentum of the kaons ($\sim 10\%$ along the x axis).

During the first FINUDA data taking period (from October 14th, 2003 to

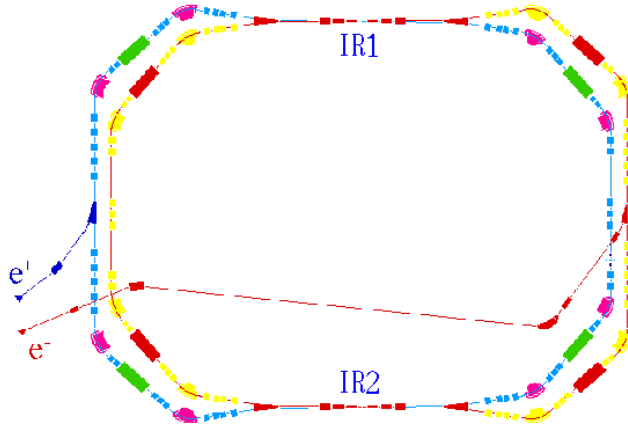


Figure 3.1: Geometrical design of the DAΦNE main rings (top view).

March 22th, 2004) a $7 \cdot 10^{31} \text{ cm}^{-2} \text{ s}^{-1}$ maximum luminosity was reached, with 100 bunches per ring. The average integrated luminosity per day was about 2 pb^{-1} , and a total integrated luminosity of 250 pb^{-1} was collected. An overall statistics of $3 \cdot 10^7$ events was collected (see Fig. 3.2). The second FINUDA data taking started on October, 2006 and ended on June, 2007. During the second data taking period an increased peak luminosity of $1.4 \cdot 10^{32} \text{ cm}^{-2} \text{ s}^{-1}$ was reached. The average integrated luminosity per day was about 7 pb^{-1} , and a total integrated luminosity of 964 pb^{-1} was collected (see Fig. 3.3).

Given the cross section for ϕ production in the e^+e^- reaction as $\sigma = 3.26 \mu\text{b}$, and the branching ratio for the $\phi \rightarrow K^+K^-$ decay, 49.1%, the number of K^+, K^- pairs collected integrating $\sim 1 \text{ fb}^{-1}$ is approximately:

$$N_{K^+K^-} = \mathcal{L} \cdot \sigma \cdot BR = 1.6 \times 10^9. \quad (3.5)$$

3.2 Experimental setup for the first data taking

The FINUDA spectrometer was designed in order to operate into one of the two interaction points of DAΦNE. The spectrometer can be described as composed by three main regions as in Fig.3.4:

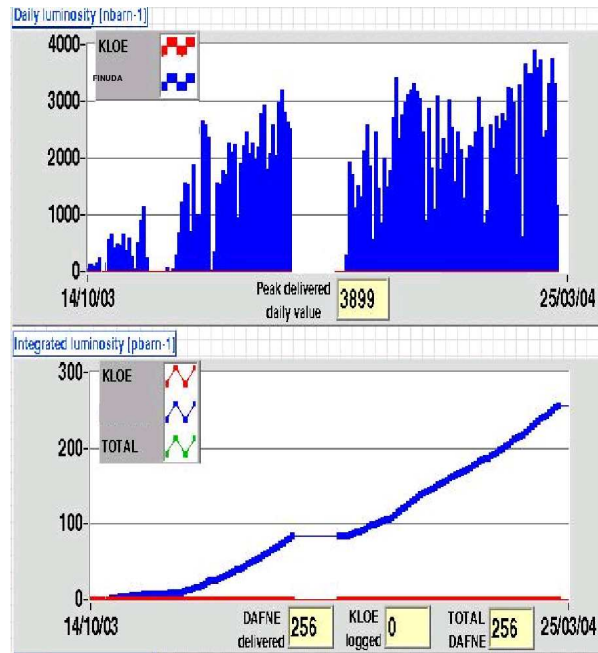


Figure 3.2: DAΦNE statistics during the first FINUDA data taking.

1. Vertex region:

- Beam Pipe
- TOFINO (central cylindrical scintillators array)
- ISIM (Inner Silicon Microstrips)
- Targets (8 targets and 5 different materials used for the first data taking)

2. Tracking region:

- OSIM (Outer Silicon Microstrips)
- Two layers of LMDs (Low Mass Drift Chamber)
- Six layers of stereo STBs (Straw tubes)

3. TOFONE (outer cylindrical scintillator array)

4. Magnet

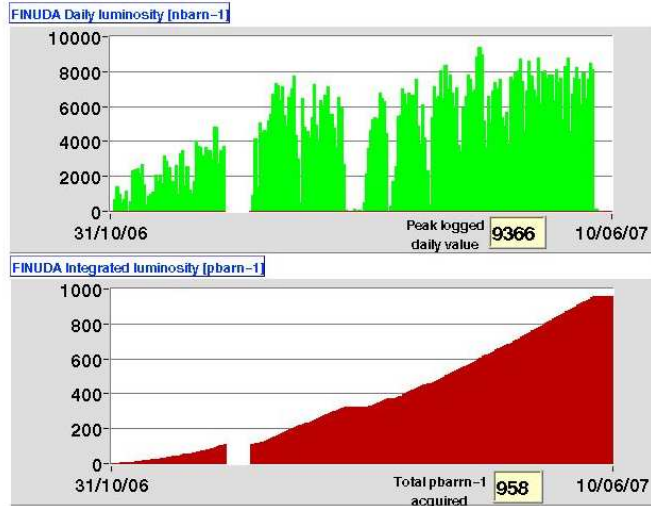


Figure 3.3: DAΦNE statistics during the second FINUDA data taking.

All the components are installed in the FINUDA main mechanical structure, called clepsydra.

3.2.1 The vertex region

This region of the spectrometer was designed in order to detect K^+K^- pairs, identify hypernuclear events and the interesting physical processes occurring within the beam interaction vertex (mainly Bhabha events and back-to-back K^+K^- events).

The highly ionizing K^+K^- pairs are detected by a barrel of 12 thin scintillator slabs (TOFINO), with a time resolution for a single mean timed slab of $\sigma \sim 250$ ps. The TOFINO detector is assembled just around the beam pipe, that is a 500 μm thick beryllium cylinder. The TOFINO provides the reference time for the electronics of the whole spectrometer, and its outputs signals are used by the trigger logic, hence high time resolution and high efficiency are required.

Target

In order to avoid the multiple scattering of particles produced by the interaction between the stopped K^- and the target nucleus, kaons must stop as

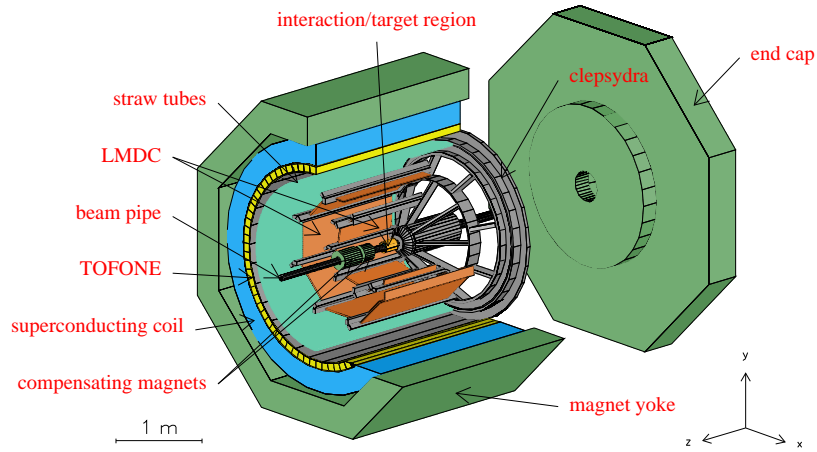


Figure 3.4: Layout of the FINUDA apparatus.

close as possible to the external surface of the target.

During the first data taking three ^{12}C targets were placed in different positions of the spectrometer in order to have calibration data to be compared with those of other experiments. In fact the $^1_{\Lambda}^{12}\text{C}$ is still the most extensively studied hypernucleus and it is useful to improve the precision of the measurement on all the observables for this hypernucleus.

Two ^6Li targets and one ^7Li target were used for the study of weak decays and for hypernuclear spectroscopy. In particular the ^6Li targets are really useful for the observation of hyperfragments. In fact the $^6_{\Lambda}\text{Li}$ is unstable for proton emission and it decays in 10^{-22} s into $^5_{\Lambda}\text{He}+p$ or into the hyperfragments $^4_{\Lambda}\text{He}+p+n$ and $^4_{\Lambda}\text{H}+p+p$, via the Coulomb assisted mechanism.

Finally the ${}^6\text{Li}$ target could offer the possibility to observe neutron-rich hypernuclei, following the reaction $K_{stop}^- + {}^6\text{Li} \rightarrow {}^6_\Lambda\text{He} + \pi^+$. In order to inspect medium-heavy hypernuclei, a ${}^{27}\text{Al}$ target and a ${}^{51}\text{V}$ target were added. These targets were arranged around ISIM as shown in Fig.3.6.

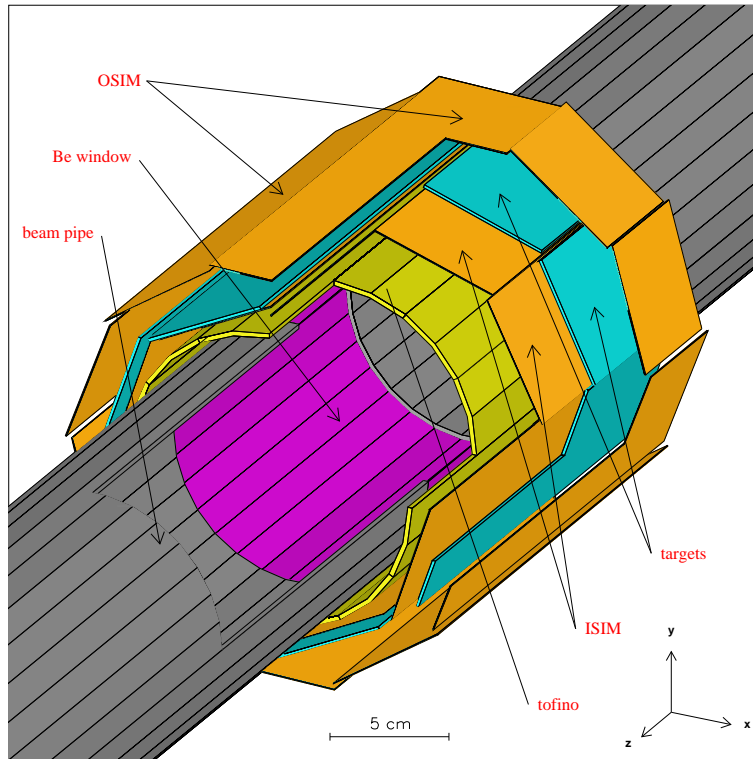


Figure 3.5: FINUDA vertex region.

ISIM

This detector is an array of eight double-sided silicon microstrip modules mounted as the faces of an octagonal prism with an apothem of about 6.5 cm. Each hit on one of these detectors is identified by its geometrical position; the Main Reference System position can be easily computed by taking into account the (x, y, z) position of the fired module.

Another information coming from the hit is the charge measured by the ADC modules, which is proportional to the energy deposited by the incident particle inside each strip $(\Delta E/\Delta x)$. Hence ISIM is used for the K^+ and

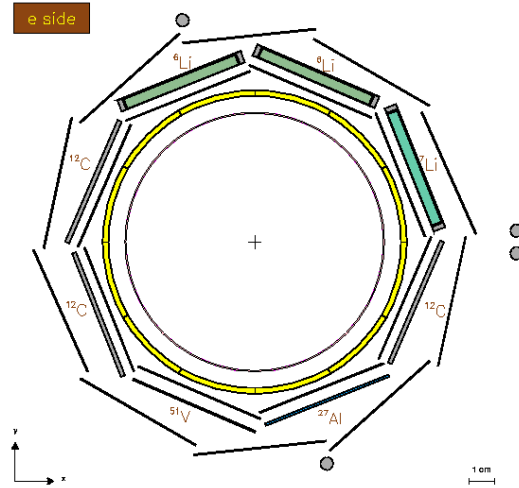


Figure 3.6: FINUDA target set-up used during the first data taking.

K^- trajectories extrapolation, for the Particle IDentification, and for the evaluation of the stopping point of each kaon.

3.2.2 The tracking region

OSIM

The OSIM microstrip array is composed by ten modules. These modules are identical to those of ISIM, but they are used for different purposes: OSIM is external to the FINUDA targets and it gives the first point for the reconstruction of each track inside the spectrometer.

The energy loss information provided by OSIM, along with the spectrometer momentum reconstruction, allows to discriminate pions, protons and deuterons.

Low Mass Drift Chamber (LMDs)

In the middle of the FINUDA tracking region two layers of drift chambers are installed. Each layer consists of eight LMDs forming an octagonal prism [49]. The spatial resolution is $100 \mu\text{m}$ along the x local axis and less than 1% of the wire length along the z axis (the wire length is 930 mm for the

inner layer and 1570 mm for the outer layer).

The drift volume is delimited by two planes of cathodic wires; the same voltage is applied to the closing field wire and to the last cathodic wire of the cell, while an increasing potential is applied to the other cathodic wires. The evaluation of the z coordinate is performed by the charge division method [50]; this led to the choice of resistive anodic wires ($\rho \sim 1900\Omega/\text{m}$). For what concerns the choice of the gas mixture, our LMDs works with a mixture of He - iC_4H_{10} (70% - 30%).

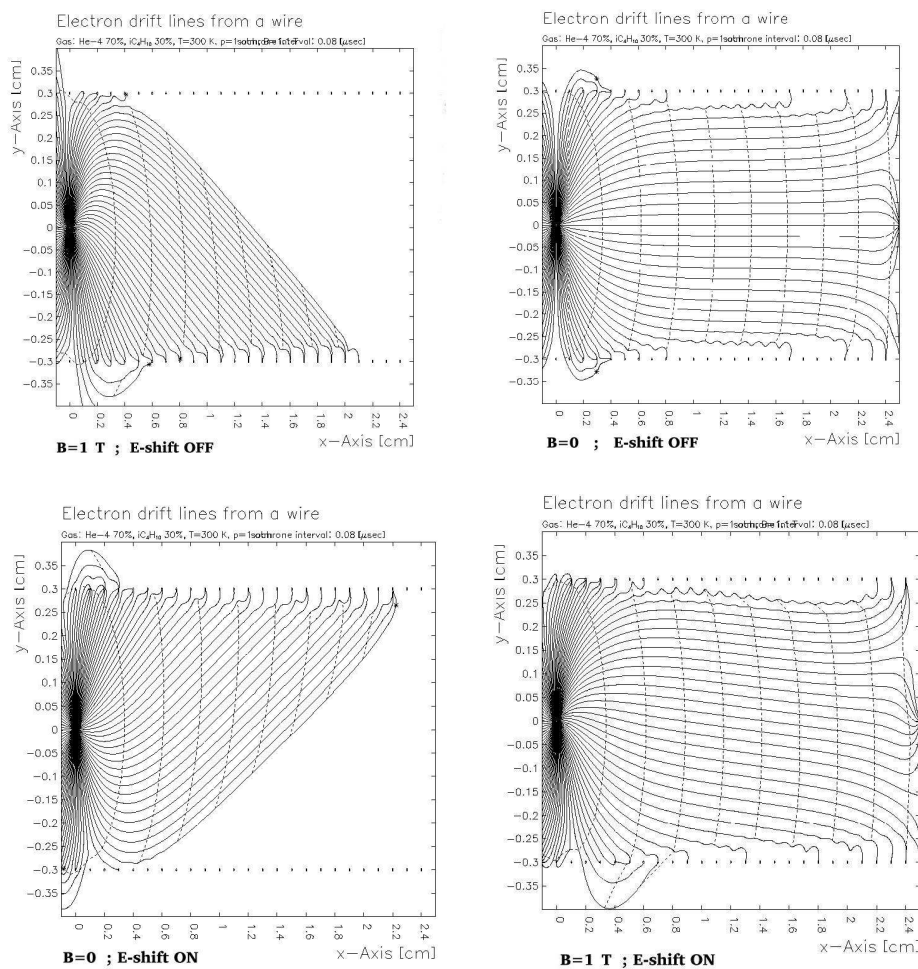


Figure 3.7: Garfield simulation results for LMDs drift cells.

In fact the Helium gas is the best candidate to minimize the multiple scattering and the degradation of used materials; moreover due to the low Z it is less sensitive to the electromagnetic background. The drift velocity corresponding to the chosen mixture is about $34 \mu\text{m}/\text{ns}$. Each LMD was designed in order to work within a 1 T magnetic field.

For this reason it was necessary to evaluate the effect of the magnetic field on the Lorentz angle and the solution was found shifting the potential along the x axis. Thanks to this technique it is possible to compensate the effect of the magnetic field on the electrons drift path. The reliability of this compensation method was tested with the *Garfield* software: results are shown in Fig.3.7.

The straw tubes array (STB)

This is the most peripheral detector of the tracking region of the FINUDA spectrometer and it consists of 2424 tubes (255 cm length) arranged in three groups of two stereo layers [51],[52]. The radius of the cylindrical region occupied by the STB array goes from 110 cm to 126 cm.

In each group each layer is rotated by 15° with respect to the contiguous one, so that the crossing point of incident particles can be extrapolated by the respective triplet of fired tubes.

In order to avoid eventual left-right ambiguities on the reconstructed point a second triplet is needed and this is the reason why six layers of straw tubes were installed. Thanks to this technique the z coordinate of the tracked particle can be measured with $\sim 500\mu\text{m}$ resolution.

3.2.3 The outer scintillator array

The TOFONE consists of 72 scintillator barrels, 255 cm long and 10 cm thick, which are placed in order to form a 127 cm radius cylinder coaxial to the beam. The detector is very important for the evaluation of the Time Of Flight of tracked particles and for the detection of neutrons. The design time resolution is 700 ps (FWHM) and the neutron detection efficiency is about 10% for a neutron energy range over an interval $[40 \div 150\text{MeV}]$.

3.2.4 The Magnet

The FINUDA magnet is a superconducting solenoid designed to provide a 1.T magnetic field with the magnetic axis parallel to the DAΦNE beam. The solenoid wraps the whole experimental apparatus. The superconducting material used for the coil wire is NbTi/Cu, isolated by a glass fiber tape. The main features of the magnet are summarized below.

Parameter	Value
Maximum Magnetic field	1.1 T
Total lenght	3800 mm
Total height	4200 mm
Iron yoke weight	230 tonn
Cryostat and coil weight	7.7 tonn
Cryostat internal radius	1385 mm
Cryostat external radius	1700 mm
Coil internal radius	1460 mm
Coil external radius	1490 mm
Coil wire total lenght	$\sim 6.1Km$
Total number of loops	1700 mm
Circulating current (1 T field)	2786 A
Discharge (quench)time	20 s
Integral field	2.67 T·m

Table 3.2: FINUDA magnet main features

3.3 FINUDA Experimental setup for 2006/2007 data taking

The difference in the experimental setup of FINUDA for 2006 data taking stands only in the inner region, where a new target assembly was inserted to substitute the older one, and a new odoscope for time-of-flight measurements (TOFINO) was placed, with thinner slabs and different light collection

system.

A scheme of the present shape of the FINUDA internal region is shown in Fig. 3.8.

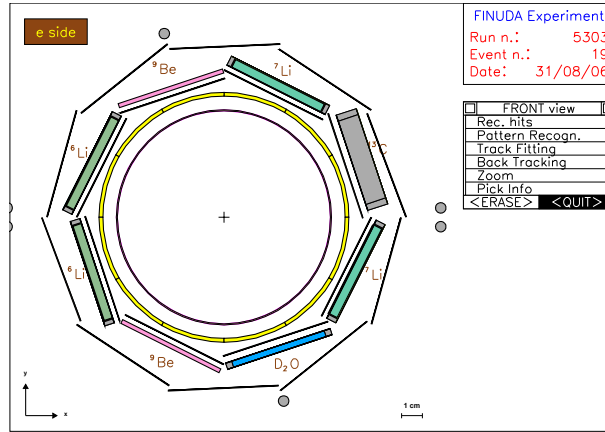


Figure 3.8: Layout of FINUDA internal region: coaxial to the beam axis (perpendicular to the picture) several layers of sensitive detectors are located. From the center outwards: beryllium beam pipe, TOFINO (12-slab thin scintillator array), Si microstrip modules inner array (ISIM), targets, Si microstrips outer array (OSIM). The labels close to the targets indicate their composition.

The TOFINO hodoscope consists always of 12 slabs, as in the FINUDA first data taking. However, its thickness was reduced to 1.8 mm, to be compared with the 2.3 mm of the old detector. The older TOFINO needed to be substituted because of the aging of the HPD's used for light collection in the first data taking. The decision to resort to ordinary Hamamatsu PM's instead allowed to reshape the detector to a more flexible geometry and to employ thinner scintillator slabs, assuring a better response and efficiency and less energy and reflection losses.

Due to the presence of the boost which affects the ϕ momentum as a consequence of the crossing angle between the beams, the internal basket containing the targets and the vertex detectors can be conventionally divided into two halves. The ϕ boost is directed in the direction of the positive abscissas: the left half of the basket is addressed as "boost side", the left

half, on the other hand, is the "antiboost" one. The K^- produced in the ϕ decay along the direction of the ϕ acquire about 13 MeV/ c of momentum, while for those emitted in the opposite hemisphere this momentum must be subtracted from the nominal one they would have were they coming from a decay at rest. The thickness of the targets in the boost half must be accurately evaluated so to allow maximum stopping of slightly faster kaons.

The ${}^6\text{Li}$ and ${}^7\text{Li}$ targets have the same structure as in the previous FINUDA data taking: they are made of Lithium tiles, 17.6 cm long, 4.75 cm wide and 4 mm thick, vacuum-sealed by aluminized composite poly films in order to prevent the contact of Lithium with air, and its prompt oxydation, and to offer mechanical stiffness. The poly foils are constituted by three film layers, the first of polyester (12 μm thick), the second of aluminum (10 μm), the third of polypropylene (75 μm), glued together to form a unique foil, for a total thickness of $\sim 110 \mu\text{m}$. The lithium core is wrapped once in a poly bag, and two more poly foils screen the rear part for the target, to allow for optimum vacuum sealing. An aluminum frame gives lateral mechanical support to this bag. Two more poly foils wrap the frame and lithium bag to improve the sealing.

The Lithium targets whose position was chosen in the ϕ -boost direction (namely, the two ${}^7\text{Li}$ ones) are moreover screened by a mylar degrader, whose thickness was properly evaluated in order to slow down kaons before they cross the target, to allow for the interaction in the material volume of the largest part of the impinging kaon beam. The optimum thickness was evaluated to be 420 μm . For Lithium targets placed on the antiboost side the presence of the degrader is not necessary, as the kaons are slow enough to be stopped, mainly, in the target volume (as well as, for about the 10%, in the ISIM silicon modules).

The Beryllium targets are stiff enough and do not to require a container or a rigid support to sustain them. However, as the material is poisonous, accidental contacts with it must be avoided, therefore two aluminum supports are used to screw the tiles to the internal flange. The Beryllium tiles are 2 mm thick, with a length of 20 cm and a width of 5.26 cm.

The position of the two ${}^9\text{Be}$ targets, as well as of the ${}^6\text{Li}$ ones, symmetric with respect to the horizontal axial plane of the inner region basket, on the

anti-boost side, was chosen in order to allow for maximum homogeneity, as far as the boost contribution is concerned, for the kaons impinging to two homologous targets.

The deuterated water target is placed in the downmost position in order to minimize possible damages to the silicon detectors in the case of water leaks. The water is contained in two contiguous 3 mm thick vessels constituted by aluminum frames closed by 110 μm poly walls. The whole length of the target is 19 cm, and its width 4.66 cm.

The ^{13}C target was assembled by filling with ^{13}C powder a vessel featuring the same structure of the water container, namely two contiguous aluminum frames with 110 μm poly closing windows. The target is 1 cm thick (allowing 2 mm tolerance at the center due to gravitational deformation of the soft content), 19 cm long in total and 4.2 cm wide. The density of the ^{13}C powder was measured to be 0.350 g/cm^3 . The target is placed in the boost side of the inner basket to exploit the possibility to measure $K^+\text{N}$ charge-exchange interactions on ^{13}C with kaons having over-threshold momentum.

Chapter 4

Offline software and simulation method

This chapter is dedicated to the description of the analysis tools employed to carry out the study of the NMWD with the FINUDA spectrometer.

The analysis was performed for three different hypernuclei (${}^5_{\Lambda}\text{He}$, ${}^7_{\Lambda}\text{Li}$ and ${}^{12}_{\Lambda}\text{C}$) studying respectively the data collected for the ${}^6\text{Li}$, ${}^7\text{Li}$ and ${}^{12}\text{C}$ targets.

In particular the search of the NMWD events implies the following requests:

- study of the π^- momentum spectrum for the identification of the momentum region corresponding to the hypernucleus formation;
- selection of the NMWD events in which a π^- and a proton are emitted from the same K^- vertex; this means that a π^- and a proton are emitted in coincidence;
- study of the energy spectra of the protons detected in coincidence with a π^- in the momentum region corresponding to the formation of the hypernucleus in its ground state;
- search of the possible background sources to the π^- momentum spectrum looking for the competitive reactions that can occur when a K^- is absorbed at rest;
- acceptance correction of the proton spectra due to the geometrical acceptance of the FINUDA spectrometer and to the algorithm used

for the data reconstruction.

In order to fulfill these requirements I took advantage of the FINUDA reconstruction program and FINUDA MonteCarlo simulation.

4.1 The FINUDA Off-line software

4.1.1 General framework and tools

The offline software of the FINUDA experiment may be divided into two main logical parts, which also correspond to two separate program modules: the FINUDA Monte Carlo simulation program “fidamc” and the FINUDA Reconstruction Program “fidarc”.

Most part of the offline code is written in FORTRAN77 language, apart from a few dedicated routines devoted to special tasks as the input-output of the data and the access to the Data Base or some particular applications aimed at detector calibration or alignment, which are written in C++ language.

The Monte Carlo simulation program is based on the simulation package GEANT3.21 [55] developed at CERN for the simulation of high energy physics experiments.

Indeed, an appropriate procedure triggered at the installation time, produces a *geometry* file containing all the information concerning the geometrical description of the apparatus, the material composition and properties of the different volumes, the elementary particle properties, the detector definitions as well as several graphical pictures of cross sections of the apparatus at different scales in the format of an RZFILE. In the Monte Carlo program a number of different tasks were accomplished:

- the detailed description of the geometrical structure of the apparatus with material composition and properties;
- the generation of simulated physical events or interactions: Bhabha events (e^+e^- elastic and anelastic scattering), $\phi(1020)$ decays accounting for the e^+e^- colliding beam properties, the hypernucleus formation

with emission of π^- , the hypernucleus mesonic and non-mesonic decays and cosmic rays;

- tracking of the produced particles in the apparatus accounting for the geometry of the different detectors and supporting structures, the mapped magnetic field produced by the superconducting solenoid, the physical interactions both electromagnetic and hadronic with the constituent materials, the particles decay;
- the simulation and digitization of the response of the different detectors with appropriate resolutions to particle hits;
- production of a simulated Raw Data Tape to submit as input to the Reconstruction Program

The Simulation program has been used for performing calculations at different stages of the apparatus development and data analysis:

- calculation of main performances of the apparatus, acceptance, resolutions, rates, at the stage of the mechanical and general design of the experiment. Optimization of the design after several tests of different possible configurations;
- calculation of trigger efficiencies, rejections and rates;
- production of a simulated Raw Data Tape (together with generated quantities) for different types of events: cosmic rays, Bhabha events, hypernuclear events to be used in the Reconstruction Program to develop and test the reconstruction algorithms;
- production of populations of events simulating physical processes and backgrounds to compute apparatus efficiencies.

The Reconstruction Program must be able to process different types of events selected by the FINUDA trigger conditions:

- Cosmic rays with and without magnetic field are used for detector calibration, for example for checking the calculated drift cell structure for the LMDC and for the Straw tubes or for the calculation of the

reference time (T-bar) for the Straw Tube drift cells, and for the mechanical alignment of the apparatus. Cospicuous data takings with cosmic rays are performed at the beginning and at the end of a long period of run to monitor also the stability of the apparatus.

- Bhabha events recorded at the commissioning of the machine and during the data taking are used to monitor the machine parameters, to evaluate the machine instantaneous Luminosity and to monitor the apparatus performances.
- The hypernuclear events which are used for the analysis on the Physics Program items. The hypernuclear trigger selects events where a K^- has stopped inside a target and a prompt track has crossed the spectrometer within the coincidence time.

These different types of events are recognized, inside the Reconstruction Program, by the appropriate trigger pattern unit code, with very little contaminations due to their very different topologies, and they are processed by separated Pattern Recognition procedures.

4.1.2 General Event Reconstruction procedures.

Data input Data are read-in into the program from three different sources. Simulated data from the Monte Carlo program, real data from the RDT produced by the data-acquisition on disk and real data from a socket of the data stream produced on-line for on-line monitoring of the data taking.

In the initialisation phase, the program reads in the geometry file produced by the Monte Carlo program in a dedicated procedure, which contains all the initialisation banks of GEANT: materials, tracking media, volumes, rotation matrices, detector's sets, particles, drawing banks. In this way, the geometrical and physical structure of the apparatus, as described in the Monte Carlo program, are reproduced inside the Reconstruction Program, making directly available all the GEANT tools for reference system change and (back)tracking in the event reconstruction in the apparatus geometry. In particular, the GEANE transport package can be linked and used for tracking and backtracking of tracks and for vertex reconstruction. In the following

I will describe briefly the reconstruction procedure for hypernuclear events only.

Pattern Recognition for K^+K^- pairs and Vertex Determination.

The hypernuclear events are triggered by requiring two fired slabs in TOFINO, with signal amplitude above an energy threshold accounting for the high ionization of kaons, together with a fast coincidence within a narrow time gate on TOFONE (≤ 10 ns).

The Pattern Recognition procedure for hypernuclear events starts with the recognition of the K^+K^- pair generated by the ϕ decay. The recognition is based on the presence of two hits on the internal microstrip (ISIM) slabs, whose dE/dX values are compatible with the energy release of a kaon, inside the azimuthal angle sectors covered by the TOFINO slabs and with signal amplitudes above the threshold which discriminate MIPS and Kaons. When two such signals are found in the triggered event, they may correspond to the crossing points on ISIM of the K^+K^- pair.

Using only the geometrical positions of these two high ionization signals on ISIM, a procedure for the reconstruction of the ϕ decay point is applied. As said before, due to the beam crossing angle (~ 12.5 mrad) at the interaction point, the ϕ meson is not produced at rest, but with a boost momentum of the order of 10% of the momentum of the emitted charged kaons from its decay, *i.e.* 12.3 MeV/ c . Due to the boost, the K^+/K^- from the ϕ decay (B.R. = 49.2%) have different momenta, therefore the helices of their trajectories in the magnetic field have different curvature radii. The importance of knowing exactly the momentum of each of the emitted kaons stands in the fact that they are subsequently tracked down to the target, and here the stopping point is evaluated by means of an algorithm based on the calculation of the energy loss of the particle in the traversed medium. It's clear that the position of the stopping point, in this calculation, depends crucially on the entrance momentum vector of the kaon in the target. The exact localization of the stopping point is mandatory to get a reliable determination of the momentum of the tracks emitted from this vertex, upon which most of the physics analyses of the processes following a kaon capture are based. Besides the *a priori* knowledge of the boost magnitude and

direction (both of which can be considered as fixed in each event), the only piece of information to get insight on the momentum of the kaons and on the location of the decay vertex is the position of the kaon hits on the ISIM modules facing the TOFINO slab whose firing, beyond a given energy loss threshold, gave part of the trigger signal. For each pair of ISIM hits on the correct ISIM moduli, a solution for the kinematic problem of determining the momenta of the kaons, whose trajectories are helices passing through these points, can be found. The problem has a kinematical constraint, since the sum of the two momenta in the laboratory should be equal, at the decay vertex, to the ϕ boost momentum.

Once the kaon starting points and their momenta and directions are known, using a forward tracking procedure based on GEANE, each kaon is tracked toward the target through the different interposed volumes, beryllium beam pipe, TOFINO slab, ISIM slab, taking into account the energy loss in the different materials and the presence of the magnetic field, in order to evaluate whether the kaon has stopped inside a target, or inside the ISIM slab or in other volumes. This procedure allows to calculate the position of its stopping point. The measured positions of the ISIM hits are appropriately taken into account. The accuracy of the procedure has been tested by Monte Carlo calculations and tuned by comparison with the experimental data; it amounts, on average, on some hundreds of microns in the radial direction for the position of the stopping vertices of K^+ and K^- . The efficiency of the K^+/K^- reconstruction algorithm is around $95\pm 3\%$.

Pattern Recognition for tracks in hypernuclear events Event by event all the hits in the FINUDA apparatus are inspected trying to connect them each other in order to construct the trajectories of the tracked particles. The track pattern recognition procedure is based on nested loops on hits on the different layers of detectors. A circle connecting three hits in x,y plane is searched for using information from:

1. STRAW - DCH2 - DCH1
2. STRAW - DCH2 - OSIM
3. STRAW - DCH1 - OSIM

4. DCH2 - OSIM - ISIM

5. OSIM - ISIM - ISIM

within selected spatial tolerances. The following step in the procedure is the association of the K^- or K^+ vertex to the track. The xy distance between the K^+/K^- vertices and the center of the circle is calculated and its compatibility with the circle's radius is checked. A linear fit is done and the fit goodness is checked to verify the zeta alignment. If both vertices are consistent with the track origin, the zeta alignment check is done and the vertex associated with the better fit is accepted. A raw helix track fitting procedure is then started using the connected hits. After that the assignment of the right kaon vertex is done again calculating the distance between fitted helix and the vertex. Possible hit connection ambiguities on OSIM/DCH1/DCH2 are solved by the iteration of the procedure and by the dE/dx check. The connection of additional I/OSIM hits in the case (1) or ISIM hits in the (2) and (3) cases is then checked. After all these procedure the track charge is assigned on the basis of the track curvature and the ETOF hits (if any) are connected to the track using the helix crossing point in TOFONE slabs.

These procedure allows to find tracks with at least three points.

The Four hits patterns are composed by the following combinations:

1. ISIM-DCH1-DCH2-STRAW
2. ISIM-OSIM-DCH1-DCH2
3. OSIM-DCH1-DCH2-STRAW
4. ISIM-OSIM-DCH1-STRAW
5. ISIM-OSIM-DCH2-STRAW
6. ISIM-ISIM-OSIM-STRAW

The Three hits patterns:

1. ISIM-DCH1-DCH2

2. ISIM-OSIM-DCH1
3. ISIM-OSIM-DCH2
4. OSIM-DCH1-DCH2
5. OSIM-DCH1-STRAW
6. OSIM-DCH2-STRAW
7. ISIM-ISIM-OSIM

We can define two different type of tracks according to their length. *Short tracks* are the particle trajectories which do not reach the straw tubes layers because they have escaped the tracking volume acceptance or spiralize inside the spectrometer.

A typical hypernuclear event reconstructed as *short tracks* is reported in Fig. 4.1. In this figure the tracks hits on the detectors are highlighted in red and the fired wires of the drift chambers are green.

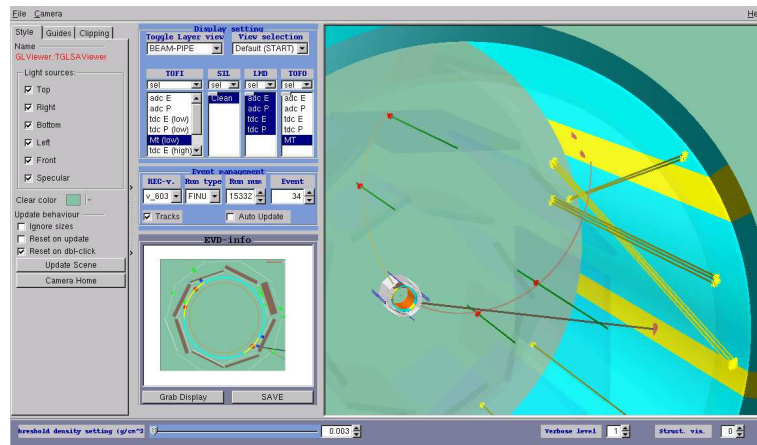


Figure 4.1: An event in which a *short track* is reconstructed in the FINUDA spectrometer using the track pattern recognition with 3 points.

Long tracks, instead, are tracks in which a hit on straw tubes layers is present and in Fig4.2 a *long track* candidate is showed with one hit on both the two layers of drift chambers (blue coloured) and one hit on the straw tube detector (yellow coloured).

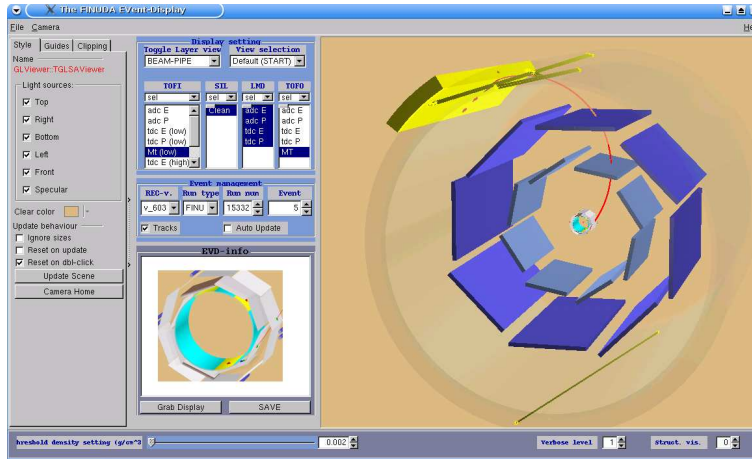


Figure 4.2: A typical *long track* reconstructed in the FINUDA spectrometer using the track pattern recognition with 4 points.

The longer tracks with four points exploit the best resolution. The tracks reconstructed with 3 points only have a worse resolution but increase the apparatus acceptance and the efficiency of the reconstruction algorithm.

Track fitting procedures. Owing to the high transparency of the apparatus the momentum of the particle can be considered constant and a spline track fitting method [56] can successfully be employed. However, the spline track fitting method requires the knowledge of the coordinates of points in the space with their uncertainties, which is the case only for the I/OSIM microstrip. For DCH1 and DCH2 chambers, the crossing point of the track trajectory on the intermediate plane of the chamber, in the (ρ, ϕ) plane projection, can only be reconstructed using the measured drift time, the time-space relationships for the drift cell calculated by GARFIELD and an estimation of the angle of the track direction relative to the chamber plane. The z coordinate of the measured point along the wires can be obtained, with a rough precision of about 1 cm, with the charge division method.

For the ST detector the spatial information produced is very different from a simple three coordinate spatial point. The information on the hit position in the z coordinate along the ST longitudinal wires cannot be provided by charge or time division, but must be obtained by exploiting the

timing information of the skewed superlayers of straw tubes. In principle, the skew angle of $\pm 12^\circ$ allows for a precision in the z coordinates of about 0.5 mm.

The particular features of the FINUDA layers of detectors requires an iterative procedure to perform the best fitting of tracks. The FIRST FIT is done using information of the connected hits. For long tracks, using the results of this first fitting, the L/R ambiguity on Longitudinal straw tubes (LOST) is solved (when possible) using multiple hits on the LOST. In both the long and short cases the points on the chambers (if any) are adjusted following the track crossing angle. Then a SECOND FIT is performed using the adjusted informations. An ITERATIVE fitting procedure is performed to find the best fitting value. At each iteration the (x,y) points on the chambers(if any) are adjusted and for long tracks the value of the zeta coordinate at LOST using the information from stereo tubes is determined too.

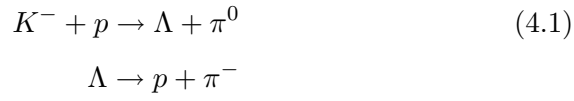
A mass recognition procedure based on dE/dX in OSIM (if any) is done. If the fitting procedure is successful and the kaon stopping point is in ISIM or TARGET the backtracking (with the GEANE package) is performed to the plane containing the kaon vertex and parallel to the target surface. This procedure allows to correct the value of the track momentum in the spectrometer (extrapolated tracks).

4.2 The FINUDA MonteCarlo simulation

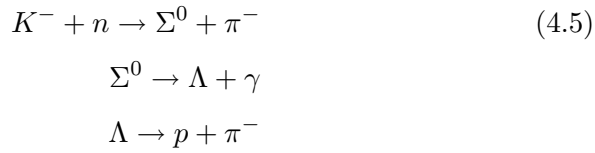
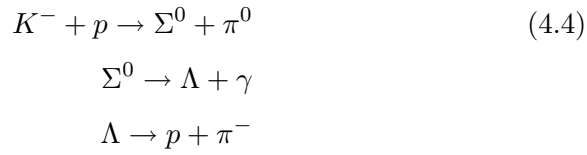
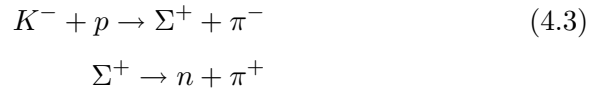
The MonteCarlo simulation of the FINUDA experiment was conceived, as said, in order to simulate all the physical channel opened when a K^- is absorbed at rest on a target: Λ hypernuclei formation and decay, Σ hypernuclei production and the background reactions related to the interaction between the K_{stop}^- and the target nucleus.

All these reactions do not form hypernuclei but involve a K_{stop}^- and nucleons such as to form π^+ or π^- in the final state. All the reactions coded in the program and producing a π^\pm in the final states are the following:

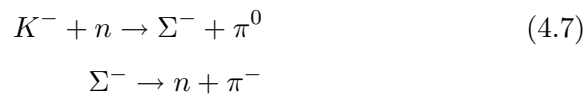
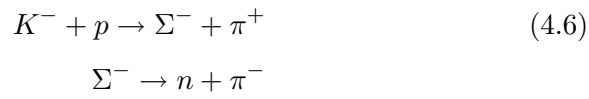
- Production of quasi-free Λ :



- Production of quasi-free Σ^+ and Σ^0 :



- Production of quasi-free Σ^- :



- Production of quasi-free Σ^- or Σ^0 or Σ^+ following the absorption of K^- on two nucleons :

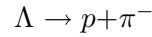
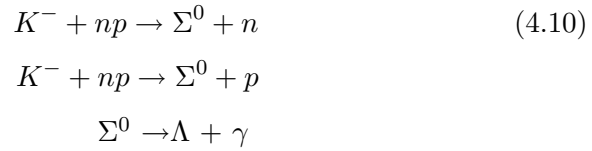
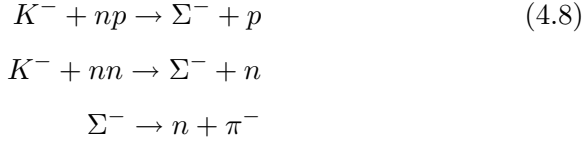


Fig.4.3 shows the result of the phase space distribution of the negative pions directly emitted from the hyperons produced through the reactions listed above when a K^- is stopped in a ^{12}C target.

In Fig. 4.3 the different background contributions are characterized by different colors and suggest that in the π^- momentum spectrum we can distinguish three different components: the lower momentum region ($p_{\pi^-} \leq 150\text{MeV}/c$) is dominated by the π^- from the decay of quasi-free Λ ; in the region from 150 MeV/c to 250 MeV/c the larger contribution is given by negative pions associated to the production of Σ^+ or Σ^- ; instead in the higher momentum region ($p_{\pi^-} \geq 250\text{MeV}/c$) the dominating contribution is given by π^- from the quasi-free production of Λ 's and from the in-flight decay of the Σ^- .

The momentum distribution of the π^- , coming from the Σ^- decay, is the

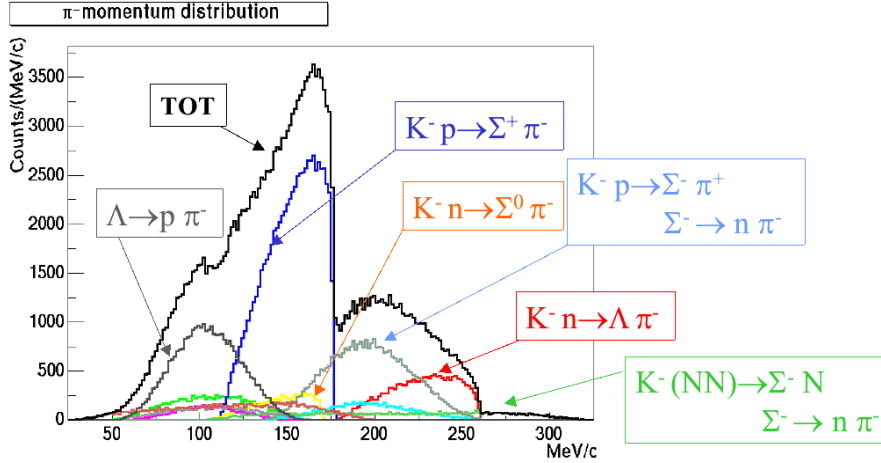


Figure 4.3: Simulated π^- inclusive spectrum for background reactions occurring at the K^-_{stop} vertex.

broadest one, due to the bigger Σ^- momentum and it extends from 250 MeV/c until 300 MeV/c, where the π^- coming from hypernuclear formation are expected to lie.

4.3 FINUDA acceptance calculation

As said in the introduction of this chapter a part of the analysis performed for the study of the NMWD consists in the calculation of the proton acceptance of the FINUDA spectrometer to correct the energy proton spectra.

For this purpose 40 millions of events were simulated; the simulation code was conceived in order that for each K^- stopped in a target a proton is generated. The protons are emitted isotropically in the FINUDA spectrometer and with a momentum extending from 100 MeV/c to 600 MeV/c. This range was chosen to calculate a correction for all the momentum range involved in the data analysis of the proton spectra and it corresponds to an energy range which extends until a maximum energy value of 180 MeV.

In Fig.4.4 the injected proton momentum spectrum is shown for one target of ${}^6\text{Li}$ and in Figs 4.5 and 4.6 the momentum spectra (on the left) and the energy spectra (on the right) filtered by the FINUDA reconstruction pro-

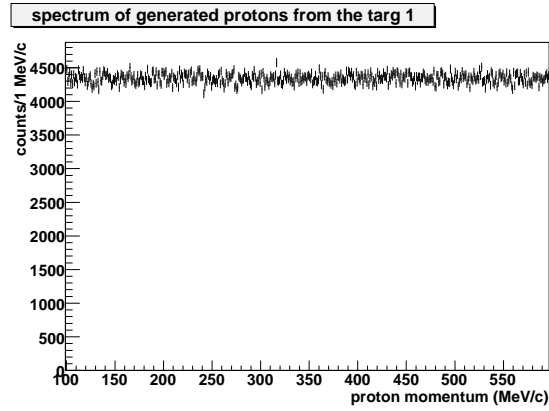


Figure 4.4: Injected proton momentum spectrum for the proton acceptance calculation of the FINUDA spectrometer.

gram are reported. The spectra were reconstructed and analyzed using the same track selection criteria that will be used for the analysis of the real data.

The track types used for the acceptance calculation and in all the analysis that will be described in the following include both the *short tracks* and the *long tracks*. In particular they are:

- Four hits pattern:
 - ISIM-OSIM-DCH1-DCH2
 - OSIM-DCH1-DCH2-STRAW
 - ISIM-OSIM-DCH1-STRAW
 - ISIM-OSIM-DCH2-STRAW
- Three hits pattern:
 - OSIM-DCH1-DCH2
 - ISIM-OSIM-DCH1
 - ISIM-OSIM-DCH2

The shown spectra are referred to a ${}^6\text{Li}$ target and a ${}^7\text{Li}$ target employed in the second data taking and the same procedure of acceptance calculation was followed for the ${}^{12}\text{C}$ targets of the first data taking.

The acceptance function η depends on:

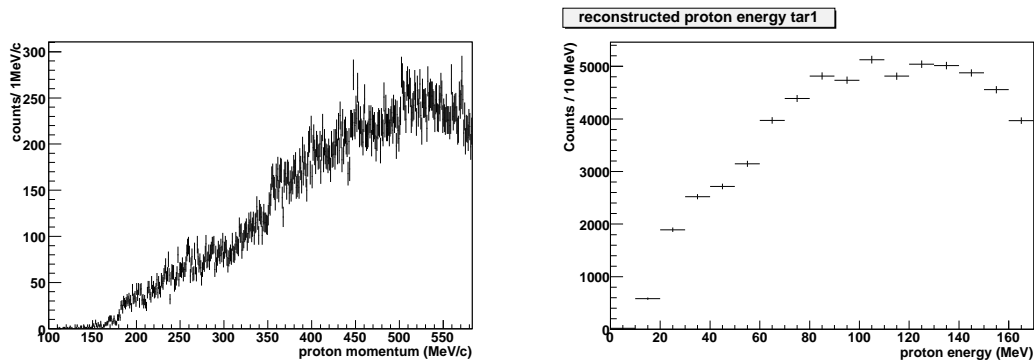


Figure 4.5: Reconstructed spectra (momentum on the left and energy on the right) of the simulated protons for the target 1 (${}^6\text{Li}$).

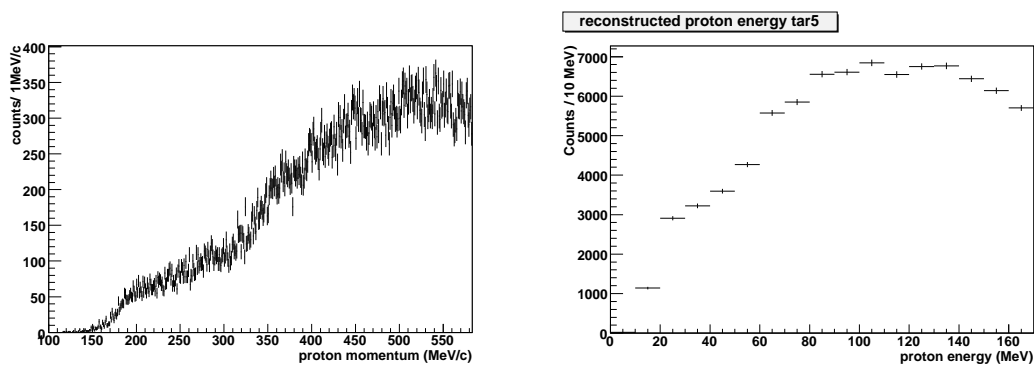


Figure 4.6: Reconstructed spectra (momentum on the left and energy on the right) of the simulated protons for the target 5 (${}^7\text{Li}$).

1. geometrical effects
2. efficiency of the FINUDA pattern recognition
3. trigger request and quality cuts.

and it is defined as the ratio between the number of generated events N_g in each energy bin and the number of reconstructed events N_{rec} for the same bin after having applied the same trigger request and quality cuts applied to the real events ($R=N_{rec}/N_g$).

The acceptance functions for a ${}^6\text{Li}$ target (target 1) and a ${}^7\text{Li}$ target (target

5) are reported in the Figs.4.7 and 4.8 and they are normalized to one in the momentum region where the acceptance is basically constant. It is possible to notice that the acceptance is constant from 80 MeV while the correction becomes bigger for the lowest energy values; this is due to the fact that in the low energy momentum the number of reconstructed events is very low respect to the generated ones.

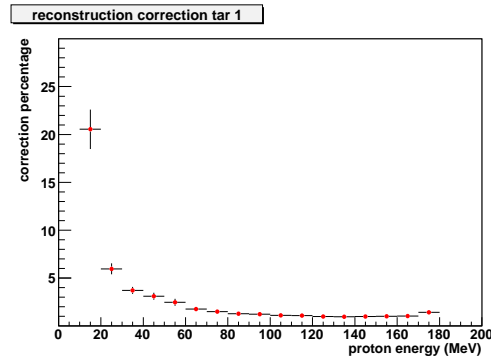


Figure 4.7: Results of the FINUDA acceptance calculation for target 1. The same criteria have been used for all the other targets employed in the data analysis.

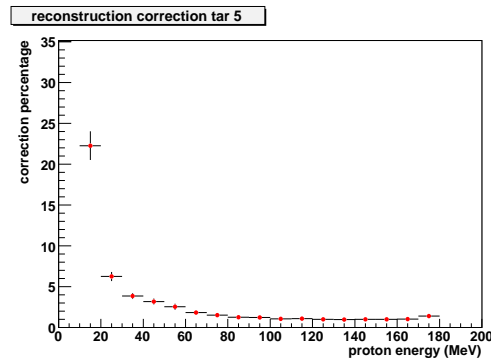


Figure 4.8: Results of the FINUDA acceptance calculation for target 5.

The statistical error on the acceptance calculation for each bin was estimated taking into account the number of simulated events and the number of reconstructed events applying the following formula:

$$\sigma(R) = \left(\frac{1}{N_g}\right) \sqrt{N_{rec} \left(1 - \frac{N_{rec}}{N_g}\right)} \quad (4.11)$$

4.4 FINUDA Particle IDentification

In order to analyze the energy spectra of the protons coming from the Non Mesonic Weak Decay the clearest proton identification is necessary.

In Figs. 4.9 the scatter plot of the specific energy loss (dE/dx in arbitrary units) in the OSIM detector is shown, measured by means of the charge amplitude information from the double-sided microstrip detectors versus the momentum calculated in the spectrometer. The energy release in the OSIM detector is evaluated by the arithmetic mean of the charge amplitude information read at the two ends of the detector.

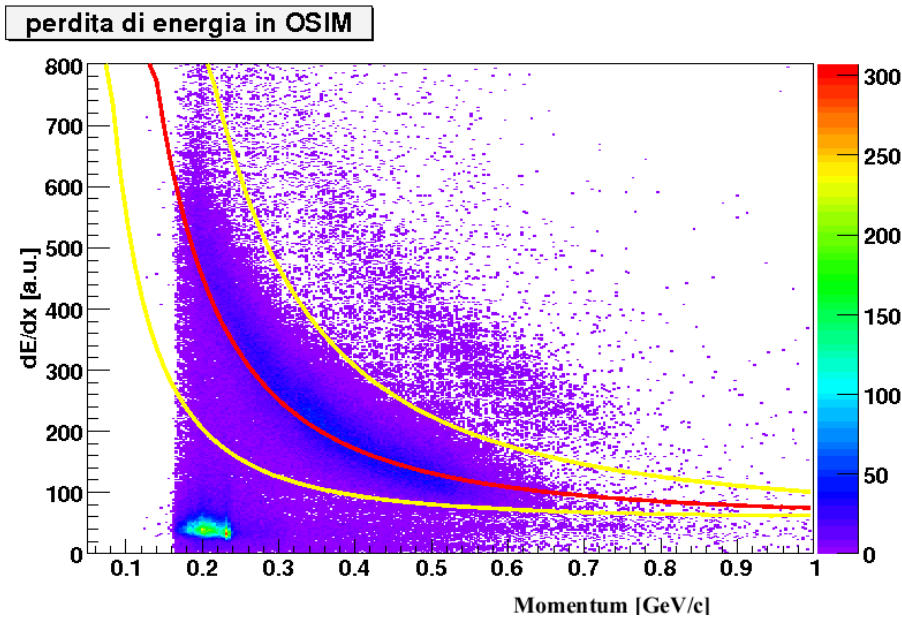


Figure 4.9: Energy loss of the particle crossing the first layer of the FINUDA silicon microstrips (OSIM).

In the plot only positive particles were selected; the red curve represents the Bethe-Bloch curve calculated for a particle having the proton mass, in-

stead the yellow curves indicate the lower and the upper limits of the region selected to identify protons.

The same measurement can also be performed, though with less precision, using the information from the drift chambers layers.

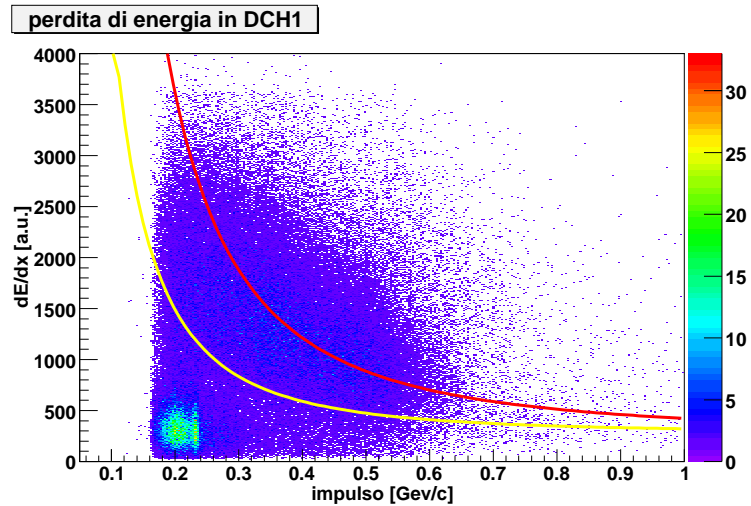


Figure 4.10: Energy loss of the particle crossing the inner layer of FINUDA Low Mass Drift Chamber.

The information on dE/dx on the three sensitive layers can therefore be matched to refine the proton selection.

In Figs. 4.10 and 4.11 the scatter plot of the energy release, measured respectively in the inner and outer layer of drift chamber is shown. It is evaluated by the geometrical mean of the charge amplitude information read at the two ends of the anode wire of each cell of the chamber as function of the momentum calculated in the spectrometer. The red curve is the Bethe-Bloch function for the proton while the yellow one allows MIPs from the NON-MIPs to be separated.

Concerning the data analysis, that will be presented in the next chapter, the proton identification was performed asking the coincidence of protons identified by the outer layer of the vertex detector (OSIM) and at least by one of the two layers of drift chambers.

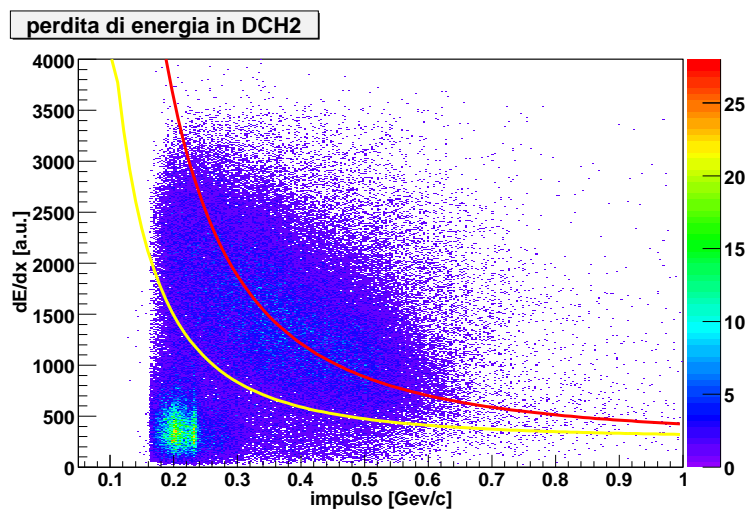


Figure 4.11: Energy loss of the particle crossing the outer layer of FINUDA Low Mass Drift Chamber.

Chapter 5

Data Analysis

The study of the Non Mesonic Weak Decay of Λ -Hypernuclei is one of the main purposes of the FINUDA experiment and, as stressed before, it is nowadays, one of the more interesting items of Hypernuclear Physics. In the following I will describe the analysis performed to study the proton-induced NMWD of three different hypernuclei: ${}^5_{\Lambda}\text{He}$, ${}^7_{\Lambda}\text{Li}$ and ${}^{12}_{\Lambda}\text{C}$.

In particular the study of ${}^{12}_{\Lambda}\text{C}$ was performed by analyzing the data collected in the first FINUDA data taking, whereas the results obtained for the ${}^5_{\Lambda}\text{He}$ and the ${}^7_{\Lambda}\text{Li}$ were achieved by analyzing the data collected in the second data taking period.

The first step of the analysis of NMWD is the identification of the ground state of the studied hypernucleus. The ground state is defined as the hypernuclear state in which the $(A-1)$ nucleons are in their lowest energy configuration and the hyperon Λ is in the $1s$ state.

In the production of hypernuclei, the populated states may be highly excited, above one or more threshold energies for nucleon or heavier nucleon clusters (d , α) decays. These states are mainly unstable with respect to the emission of a hyperon, of photons and nucleons. The spectroscopic studies of strong and electromagnetic de-excitations give information on the hypernuclear structure which are complementary to those from excitation functions and angular distribution studies.

When the hypernucleus is in its ground state (*g.s.*) it is stable with respect to electromagnetic and strong processes. In this configuration the Λ particle

can only decay via a strangeness-changing weak interaction.

In FINUDA the hypernucleus is formed, as already mentioned, through the *strangeness exchange reaction* with $K_{stopped}^-$ with the emission of a prompt π^- . The decay of the hyperon can then follow.

In this way a proton induced NMWD event with the FINUDA spectrometer can be identified "*looking for*" a π^- coming out from the target, where K^- stops, in coincidence with the emission of a positive track identified as a proton and coming from the same K^- vertex. The prompt π^- of the production reaction, has a defined momentum value which corresponds to the formation of the hypernucleus in its ground states.

According to the well known formula of the two-body reaction kinematics, the π^- momentum p_{π^-} can be calculated as a function of the hypernucleus mass as follows:

$$p_{\pi^-} = \sqrt{\left[\frac{(m_{K^-} + m_A)^2 + m_{hyp}^2 - m_{\pi^-}^2}{2(m_{K^-} + m_A)} \right]^2 - m_{hyp}^2} \quad (5.1)$$

where m_{hyp} is given by the equation (1.12), m_{π^-} is the negative pion mass and $(m_{K^-} + m_A)$ is the sum of the K^- and the target nucleus mass corresponding to the energy of the $A+K^-$ system at rest. The analysis was performed for 6Li , 7Li and ${}^{12}C$ targets and in particular when a K^- is stopped in a 6Li nucleus it forms a ${}^6_{\Lambda}Li$ hypernucleus; this hypernucleus has the peculiar feature of being unstable by nucleon emission.

In fact the ${}^6_{\Lambda}Li$ *g.s.* is *proton unbound* and it immediately decays according to



This means that after the identification of the ${}^6_{\Lambda}Li$ ground state formation we can extract information about the NMWD of the ${}^5_{\Lambda}He$.

The π^- momentum values calculated by Eq 5.1 for each of the studied target, and the corresponding Λ binding energy of the hypernucleus *g.s.* are listed in Tab. 5.1

The ground state of a hypernucleus gives a signature in the overall π^- momentum spectrum corresponding usually to the peak at highest momentum. Of course one has to keep in mind that the FINUDA spectrometer was

Target material	Hypernucleus	B_{Λ} (MeV)	π^{-} momentum (MeV/c)
${}^{12}\text{C}$	${}^{12}_{\Lambda}\text{C}$	10.8	272.72
${}^6\text{Li}$	${}^5_{\Lambda}\text{He}$	4.3	275.15
${}^7\text{Li}$	${}^7_{\Lambda}\text{Li}$	5.4	276.81

Table 5.1: π^{-} momentum corresponding to the Λ binding energy (B_{Λ}) of the hypernucleus ground state. The B_{Λ} values have been calculated or extrapolated from experimental values ([57] and [58]).

designed for the study of Λ -Hypernuclei production and decay optimizing the detection and the reconstruction of negative tracks with a momentum of about 270 MeV/c. The NMWD events which we are interested in were selected applying the following general requirements:

- identification of a $K^{+} K^{-}$ pair produced from the ϕ decay;
- K^{-} stopped in the target;
- at least two tracks coming from the K^{-} vertex;
- tracks with a successful fitting and extrapolation to the target.

5.1 First analysis of ${}^{12}_{\Lambda}\text{C}$

In this section the analysis of the data collected during the first data taking for the three carbon targets will be described. The analysis started with a study of the excitation energy spectrum of all the ${}^{12}\text{C}$ targets and performed requiring:

1. a negative track (negative pion candidate) connected to the K^{-} stopping point;
2. track reconstructed by fitting 4 points measured in the spectrometer: *long tacks*;
3. strict requirement of a good χ^2 out of the track fitting procedure.

The π^- momentum spectrum obtained under these conditions is shown in Fig. 5.1.

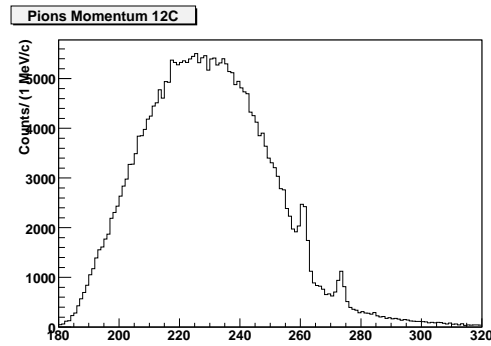


Figure 5.1: Inclusive momentum spectrum of π^- emitted from ^{12}C targets. The spectrum is the sum of the data collected from the three ^{12}C targets employed in the first data taking.

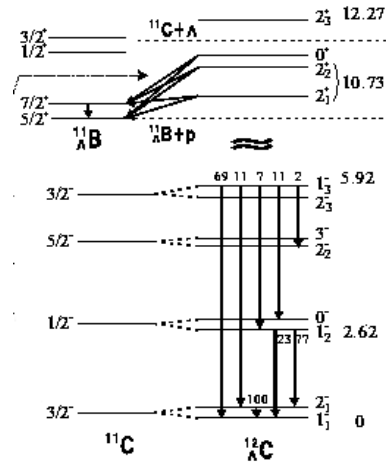


Figure 5.2: Level scheme of the $^{12}_{\Lambda}\text{C}$ bound state.

One can note a physical background extending beyond the kinematical limit of the reaction (273 MeV/c) which is due to the K^- absorption reaction described in the section 4.2 and there are two peaks which correspond, respectively, to the formation of the $(^{11}_{\Lambda}\text{B} + \text{p})$ (262 MeV/c) in its ground state and of the ground state of the $^{12}_{\Lambda}\text{C}$ hypernucleus (272.7 MeV/c).

The scheme of the energy levels, obtained from experimental results, for ${}_{\Lambda}^{12}\text{C}$ is presented in the Fig.5.2. In Fig. 5.3 the π^{-} spectrum is shown, with the additional requirement of a proton in coincidence. The spectrum filled in grey in Fig. 5.3 is the π^{-} spectrum obtained from the simulation of the reaction $K^{-} + np \rightarrow \Sigma^{-} + p$ followed by the in-flight decay $\Sigma^{-} \rightarrow n + \pi^{-}$ filtered through the same selection criteria as used for the real data and fitted to the tail shape beyond 275 MeV/c.

As showed in Fig. 4.3, the K^{-} absorption process from a np pair is the only background channel for this momentum region. The agreement between the data and the simulation in the overlap region is quite good: the χ^2 test gives a value $\chi^2/d.o.f= 1.2$.

The area filled in black correspond to the momentum region identified as the ground state ($g.s.$) of the ${}_{\Lambda}^{12}\text{C}$ and it extends from 270 MeV/c to 275 MeV/c.

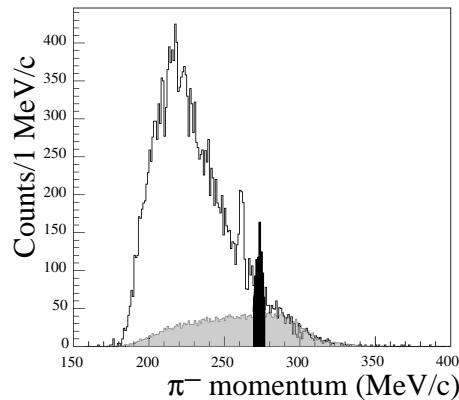


Figure 5.3: Momentum spectrum of the π^{-} with the additional requirement of a proton in coincidence. The grey spectrum represents the π^{-} spectrum from K^{-} absorption by two nucleons. The black area of the peak at 273 MeV/c represents the ${}_{\Lambda}^{12}\text{C}$ $g.s.$

The spectrum of the proton from the ${}_{\Lambda}^{12}\text{C}$ NMWD has been obtained selecting events in the black region of Fig. 5.3 and requiring the identification of an additional proton. In the spectrum all the proton tracks identified as *long* were included, summing the events from the three ${}^{12}\text{C}$ targets. The result, after the acceptance correction, is presented in Fig.5.4.

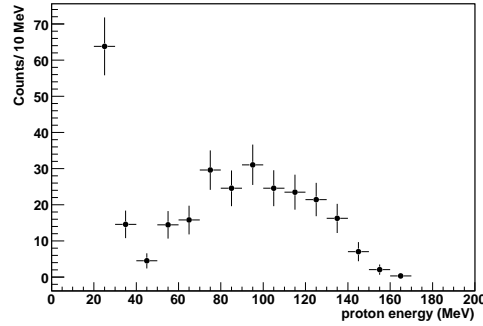


Figure 5.4: Energy spectrum, acceptance corrected, of the protons emitted in coincidence with a π^- in ${}^{12}\text{C}$ *g.s.* region.

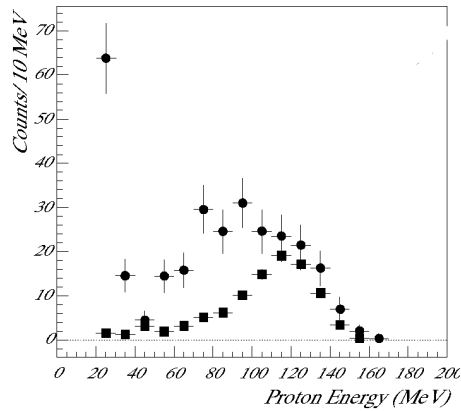


Figure 5.5: Dots: energy spectrum of the protons emitted in coincidence with a π^- in ${}^{12}\text{C}$ *g.s.* region. Squares : energy spectrum of the protons, from the K^- absorption by two nucleons, emitted in coincidence with pions of the *g.s.*

The proton spectrum is characterized by a bump around an energy value of 80 MeV which is half of the Q value of the NMWD reaction (~ 150 MeV) and by a tail beyond 100 MeV that is due to the contribution of the background protons.

In order to subtract the background from the real data energy spectrum a MonteCarlo simulation of the K^-np absorption reaction was done, and

events with a π^- of momentum corresponding to the ${}_{\Lambda}^{12}\text{C}$ *g.s.* region was selected: the spectrum of the proton detected in coincidence with these π^- 's was then used to model the background contribution.

In Fig.5.5 the real data energy spectrum (dots) and the simulated one (squares) are reported; Fig. 5.6 shows the result of the subtraction. The simulated spectrum was normalized to the experimental one fitting the tail beyond 100 MeV and it was acceptance corrected.

The latter is as the proton spectrum expected from a simple $\Lambda n \rightarrow np$ weak decay reaction in nuclear matter. The bell shaped spectrum, centered around 80 MeV is well explained by the Fermi momentum of the interacting baryons in the nucleus giving a spread of ~ 60 MeV. The errors for each bin are statistical only and they were calculated taking into account both the statistical error on the data and the statistical error on the MonteCarlo Simulation. 4×10^6 events were simulated and the simulated events were selected with the same criteria of the real data in order to have for the simulated spectrum an error of one order of magnitude lower than those on the measured spectrum.

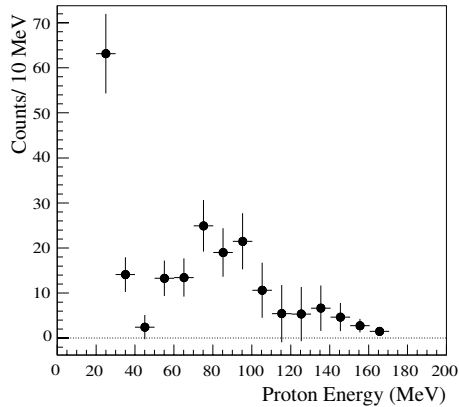


Figure 5.6: Difference of the two spectra of Fig.5.5

The low energy rise can be explained both by the Final State Interaction (FSI) due to the proton rescattering in the nucleus and by the opening of the two nucleon induced NMWD channel ($\Lambda np \rightarrow nnp$). For this reason it

is interesting to notice that FINUDA, thanks to the use of very thin targets, has lowered the proton energy threshold down to ~ 20 MeV, as compared with 40 MeV at least of previous experiments, thus providing more information about the influence of the FSI in the NMWD process and giving us the possibility to have a cleaner comparison with the theoretical calculations. This last point will be discussed in the next chapter together with a comparison with other experimental results obtained at KEK laboratory. The results about the study of the proton weak decay of the ${}^7_{\Lambda}\text{C}$ *g.s.*, described above, has been presented at the HYP2006 Conference in Mainz and they have been published on September, 2007 [59] .

5.2 NMWD of the ${}^7_{\Lambda}\text{Li}$

In order to study the NMWD of the ${}^7_{\Lambda}\text{Li}$ hypernucleus all the data collected during the second FINUDA data taking for the two ${}^7\text{Li}$ targets were analyzed.

In the analysis of the π^- momentum spectra the same requirements described for the ${}^{12}\text{C}$ targets were adopted with the addition of a cut on the distance between the π^- extrapolated track point and the K^- vertex.

This last requirement has been adopted in order to select only the negative pions that come from the primary vertex, thus optimizing the signal to background ratio of the spectrum.

In fact, as already underlined, the main background contribution to the π^- momentum distribution in the *g.s.* region comes from Σ^- in-flight decay. Due to the Σ^- mean life time of $(1.479 \pm 0.011) \times 10^{-10}$ s, the π^- can be produced several mm apart from the K^- stopping point. On the contrary the π^- following the Λ -Hypernuclei formation is produced at the same point in which the K^- is absorbed at rest.

As already stressed in Chapter 4, the reconstruction algorithm extrapolates the tracks from the hit on ISIM/OSIM to the vertex of the stopped K^- , which determines the pion origin point. In order to have the better compromise between the bigger fraction of signal and the smaller one of background all that events with a distance between the π^- extrapolated track point and the K^- vertex less than 0.3 cm were included in the analysis thus increasing

the signal-to-background ratio of a factor 2. In Fig.5.7 the inclusive π^- momentum spectrum is reported obtained summing the two different targets of ${}^7\text{Li}$. The spectrum is characterized by a peak centered at a momentum value of ~ 275 MeV/c that corresponds to the formation of the ${}^7_{\Lambda}\text{Li}$ hypernucleus in its ground state. This value is in agreement with the calculated one, reported in Tab.5.1. The red selection range extends from 272 MeV/c to 278 MeV/c and it corresponds to the interval that I chosen for *g.s.* region of the ${}^7_{\Lambda}\text{Li}$ formation.

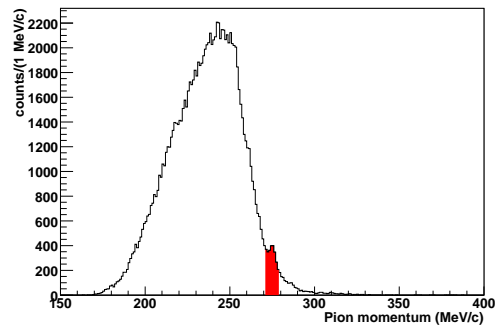


Figure 5.7: Inclusive momentum spectrum of π^- emitted from ${}^7\text{Li}$ targets. The spectrum is the sum of the data collected from the two ${}^7\text{Li}$ targets employed in the first data taking.

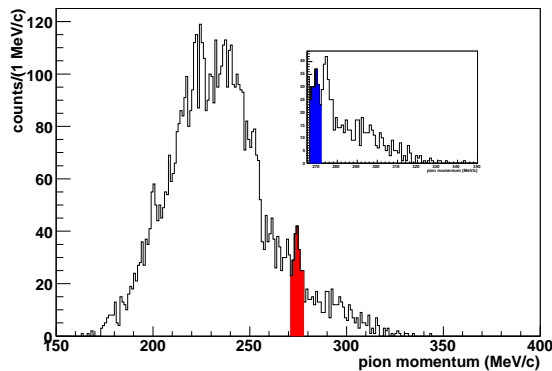


Figure 5.8: Momentum distribution of negative pions detected in coincidence with a proton. The red region corresponds to the ${}^7_{\Lambda}\text{Li}$ *g.s.*.

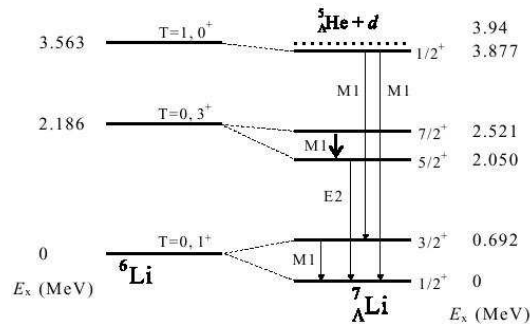


Figure 5.9: Level scheme of the ${}^7_{\Lambda}\text{Li}$ bound state. Corresponding level of ${}^6\text{Li}$ are also shown. From [77]

After the experimental identification of the *g.s.*, for each K^- stopped inside the two ${}^7\text{Li}$ targets a proton was required in coincidence. The π^- are *long tracks* only, while the protons were identified asking:

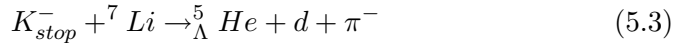
1. a positive track (proton candidate) connected to the K^- vertex in the target
2. reconstructed tracks by fitting at least 3 points in the spectrometer (*short* and *long tracks*)
3. particle identification of the proton through the method described in Sec. 4.4.

The π^- tracks are *long tracks* only because π^- identified as *short tracks* have a momentum lower than 200 MeV/c and this means that their inclusion in the π^- spectrum analysis does not improve the statistic in the *g.s.* momentum region which we are interested in. Fig. 5.8 shows the momentum spectrum of the π^- for the events with an additional proton. Close to the ${}^7_{\Lambda}\text{Li}$ *g.s.* peak (red region), a second peak appears at a lower momentum centered at ~ 269 MeV/c. In the inset of the figure a zoomed view of the spectrum region in which the blue peak is selected is shown.

Since this second unexpected peak appears just asking for the proton coincidence, the source of this signal in the π^- spectrum was investigated searching all the possible hypernuclear systems which can be a source of

proton decay in the ${}^7\text{Li}$ target.

The hypernuclear systems that can be produced, stopping a K^- in a ${}^7\text{Li}$ target, are the following : ${}^7_{\Lambda}\text{Li}$, (${}^6_{\Lambda}\text{He} + \text{p}$), (${}^5_{\Lambda}\text{He} + \text{d}$), (${}^4_{\Lambda}\text{He} + \text{t}$), (${}^4_{\Lambda}\text{H} + {}^3_{\Lambda}\text{He}$), (${}^3_{\Lambda}\text{H} + \alpha$) and all the others channels in which d may be replaced by p+n, t by d+n or p+p+n and so on. Apart from the ${}^7_{\Lambda}\text{Li}$, with a mass $m_{{}^7_{\Lambda}\text{Li}} = 6711,60$ MeV, the lowest hypernuclear mass is found for the (${}^5_{\Lambda}\text{He} + \text{d}$) system with $m_{{}^5_{\Lambda}\text{He}+\text{d}} = 6715,57$ MeV. Therefore the "blue" peak can be assigned to the following reaction:



The maximum momentum of the π^- emitted in the reaction (5.3) was evaluated considering the case in which the π^- is emitted in a back-to-back configuration respect to the system ${}^5_{\Lambda}\text{He} + \text{d}$. Using the formula (5.1), a momentum value equal to $p_{\pi^-} = 272,67$ MeV/c was found.

Looking to the inset of the Fig. 5.8 the end point of this second peak is at 272 MeV/c. Furthermore, calculating the difference, in binding energy, between the (${}^5_{\Lambda}\text{He} + \text{d}$) and ${}^7_{\Lambda}\text{Li}$ formation with the emission of a π^- which has respectively 269 MeV/c and 275 MeV/c of momentum (central values of the two peaks in the experimental spectrum) a value $\Delta B_{\Lambda} = 3.98$ MeV was obtained. This value is fully consistent with the one experimentally measured [88] and reported in Fig. 5.9. This means that studying the spectrum of the protons emitted in coincidence with the pion belonging to the momentum region of the "blue" peak we have the chance to analyze the proton weak decay of ${}^5_{\Lambda}\text{He}$. In Fig.5.10 (left) the energy spectrum of the protons detected in coincidence with a π^- of the ${}^7_{\Lambda}\text{Li}$ *g.s.* and coming from the NMWD of the ${}^7_{\Lambda}\text{Li}_{g.s.}$ is shown.

This spectrum is the sum of the contributions of the two ${}^7\text{Li}$ targets and it is not acceptance corrected yet. It presents, as expected, a peak around 80 MeV and a tail to higher energy values due to the K^- np absorption process. The inclusion of tracks obtained by fitting three measured points only, namely the *short tracks* (without hits on straws), allows the spectrum to extend down to 15 MeV, a region never studied before.

Using the MonteCarlo acceptance calculation described in Sec.4.3 the

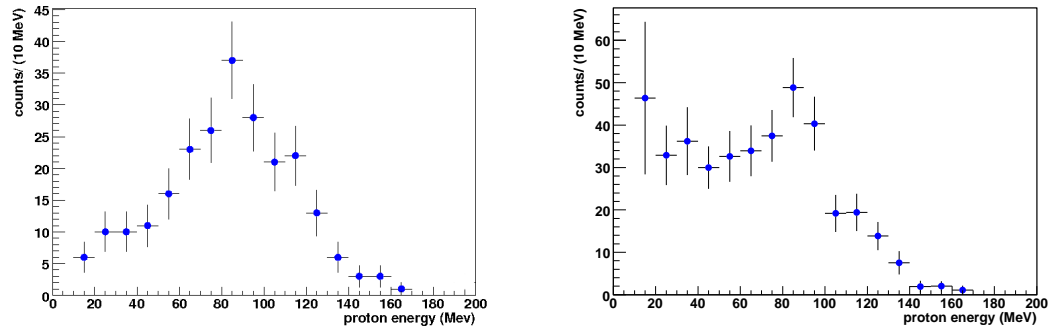


Figure 5.10: Left: Energy spectrum, not acceptance corrected, of the protons emitted in coincidence with a π^- in ${}^7_\Lambda\text{Li}$ *g.s.* region; right: energy spectrum obtained after the acceptance correction for the ${}^7_\Lambda\text{Li}_{g.s.}$

spectrum was acceptance corrected thus obtaining the result shown in Fig. 5.10 (right). Also after the acceptance correction the peak at around 80 MeV is clearly visible and a further enhancement appears in the low energy region (below ~ 40 MeV) due to the proton rescattering effect inside the ${}^7\text{Li}$ target (Final State Interaction in the following) and/or to the multi-nucleon induced processes, among which the most sizeable contribution at low energy is given by the two nucleons induced non mesonic decay.

The errors were calculated taking into account the statistical error on the data, on the Monte Carlo simulation and the corresponding statistical error on the acceptance calculation. The error evaluation on the acceptance was carried out as described in Sec 4.3. The very low energy part of the proton energy spectrum has a very limited acceptance therefore the errors on the first bins are quite sizeable.

After the acceptance correction the background contribution to the energy spectrum was evaluated. Since in the momentum region beyond the bound states (that corresponds to momentum values larger than 278 MeV/c), as said before, only the $K^- + np \rightarrow \Sigma^- + p$ absorption reaction is effective (with the subsequent Σ^- decay and/or conversion) a MonteCarlo simulation of this reaction also for the two ${}^7\text{Li}$ targets was performed.

In the simulation the K^- is assumed to interact on a np correlated pair in

${}^7\text{Li}$ nucleus. The ${}^7\text{Li}$ nucleus is assumed at rest, while to the nucleons a momentum according to the Fermi distribution is assigned. The simulated data were selected applying the same criteria and cuts used for the real data. Fig. 5.11 shows in red the background contribution fitted to the π^- momentum tail beyond 278 MeV/c.

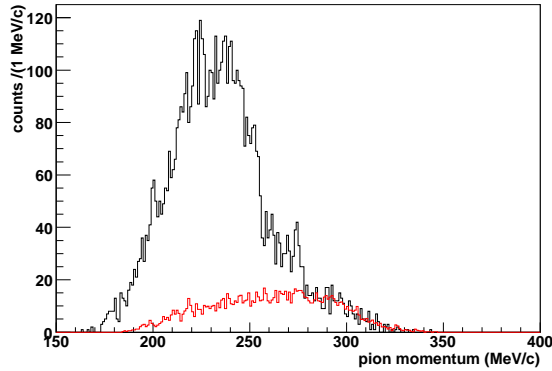


Figure 5.11: π^- momentum spectrum for events with an additional proton track and superimposed (red histogram) the contribution to the spectrum of the K^-np channel, normalized to the spectrum tail.

Considering the overlap region of the two distribution I have evaluated the agreement between the data and the simulation founding a $\chi^2/d.o.f$ value equal to 1.3, thus revealing a quite good evaluation of the background contribution to the data. The background subtraction from the proton energy spectrum is therefore possible selecting the protons in coincidence with a π^- coming from the np absorption mechanism. The background subtraction is performed for the events whose π^- momentum falls in the fixed ground state interval. In Fig. 5.12 the comparison between the real data proton spectrum and the protons coming from the simulation is shown and the result of the background subtraction can be seen. Looking to this last spectrum we can observe the rise of the spectrum in the low energy region as demonstration of FSI effects, an enhancement at around 80 MeV and beyond this energy value a rapid fall. It seems that the FSI contribute to the proton induced NMWD but its contribution is not so strong to eliminate the signal at 80 MeV.

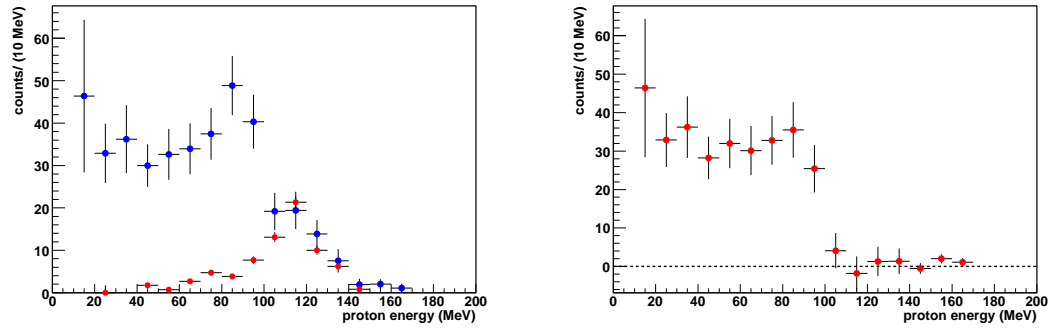


Figure 5.12: Left: (blue points) protons coming from the weak decay of ${}^7_{\Lambda}Li_{g.s.}$; red points: energy spectrum of the protons coming from the background reaction emitted in correspondence of the $g.s.$. Right: proton spectrum from the NMWD of the ${}^7_{\Lambda}Li_{g.s.}$ after the subtraction of the background contribution

5.3 NMWD of ${}^5_{\Lambda}He$

5.3.1 Proton weak decay of ${}^5_{\Lambda}He$ from 7Li targets

A first analysis of the proton weak decay of ${}^5_{\Lambda}He$ was carried out extracting the energy spectrum of the protons emitted in coincidence with a π^- belonging to the momentum region selected in blue in Fig.5.8. The proton spectrum, thus obtained, is shown in Fig 5.13 (on the left) together with the result of the acceptance correction of the energy proton spectrum (on the right). The energy spectrum looks quite different from the one obtained for the ${}^7_{\Lambda}Li_{g.s.}$ and this difference is probably due to the contribution of the deuteron in the system (${}^5_{\Lambda}He + d$). The background source of the proton spectrum is the same described for the ${}^7_{\Lambda}Li_{g.s.}$ case and its contribution has been evaluated performing the same simulation study done for ${}^7_{\Lambda}Li$. Fig 5.14 shows (on the left) the acceptance corrected proton spectrum of ${}^5_{\Lambda}He$ in blue and the protons coming from the simulation of the K^- absorption process in red; on the right of the figure the result of the background subtraction is reported.

This last proton spectrum is characterized by a bump around 80 MeV

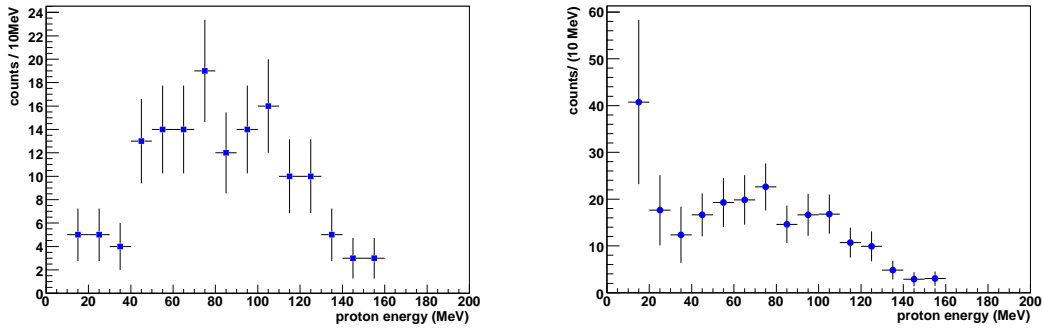


Figure 5.13: Left: energy spectrum, non acceptance corrected, of the protons emitted in coincidence with a π^- emitted after the formation of the ${}^5_{\Lambda}\text{He}$ with the ${}^7\text{Li}$ target; right: result of the acceptance correction of the proton spectrum shown on the left of this figure.

that does not appear so clearly in the proton energy spectrum of the ${}^7_{\Lambda}\text{Li}_{g.s.}$ and the contribution of the FSI is always present. The next step in the study of the proton-induced NMWD of ${}^5_{\Lambda}\text{He}$ is the analysis of the two ${}^6\text{Li}$ targets and the comparison of the energy spectrum thus obtained with the one extracted from the analysis of the ${}^7\text{Li}$ targets.

5.3.2 Proton weak decay of ${}^5_{\Lambda}\text{He}$ from ${}^6\text{Li}$ targets

In the following the analysis of the NMWD of the ${}^5_{\Lambda}\text{He}$ hypernucleus produced in the two ${}^6\text{Li}$ targets employed in the second run will be described. The starting point of the analysis is the study of the inclusive momentum proton spectrum for ${}^6\text{Li}$ (two targets) and the comparison of this spectrum with the one obtained for the ${}^7\text{Li}$ (two targets). This comparison is useful in order to see if any difference appears in the proton spectrum when a K^- is captured in a ${}^7\text{Li}$ or a ${}^6\text{Li}$ due to the fact that the ${}^6\text{Li}$ can be considered as a $(d + \alpha)$ cluster.

The events included in the two spectra, reported in Fig. 5.15, were selected applying for the proton identification and selection the same criteria adopted in the proton spectrum analysis of ${}^7_{\Lambda}\text{Li}$.

The proton momentum spectra are not acceptance corrected. The ac-

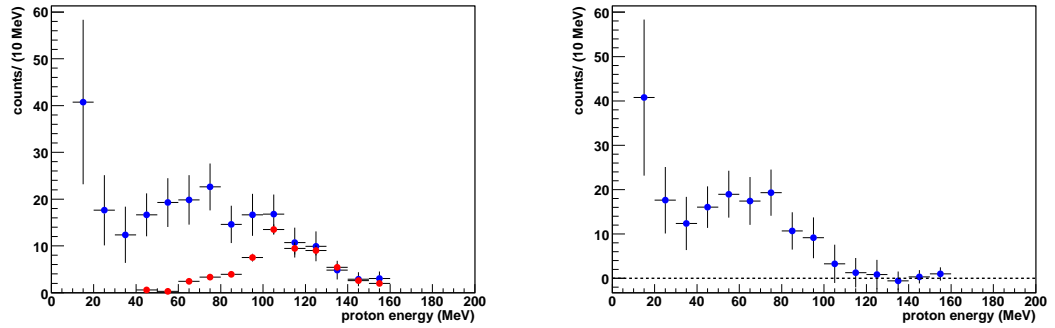


Figure 5.14: Left: proton spectrum coming from the background absorption process (red dots) superimposed to the acceptance corrected proton spectrum obtained from the data (blue dots); right: proton energy spectrum of ${}^5_{\Lambda}\text{He}$ after the background subtraction

ceptance correction is effective only in the low momentum region, where it is a monotonic rising function, and does not affect the region beyond 400 MeV/c, where it is almost constant. The spectrum in Fig 5.15 for ${}^7\text{Li}$ (on the right) shows a distribution with a lower cut at 150 MeV/c due to the momentum acceptance for proton identified as *short tacks* and the peak emerging at about 370 MeV/c is due to the quasi-free reaction $K^-n \rightarrow \Lambda\pi^-$ and other spurious dips emerge in the spectrum as a consequence of the shadowing effect of some apparatus mechanical supports.

The spectrum of ${}^6\text{Li}$ shows, in addition, a prominent structure peaked at about 500 MeV/c. This peak is the signature of a two nucleon K^- absorption, with Σ^-p in the final state [90]. The signature is more evident in ${}^6\text{Li}$ nucleus and this suggests that the K^- absorption may occur more easily on ${}^4\text{He}$ or, most probably, on a deuteron inside the nucleus (therefore with its own Fermi momentum). The two-cluster structure of ${}^6\text{Li}$ is a well known feature and it emerges by the $(\pi^+, 2p)$ reactions in flight [89] [91] and $(\pi^+, 2n)$ reactions at rest [92] [93]. The same behavior holds also for ${}^4\text{He}$, which can be understood as a cluster of two deuterons. This evidence is extremely important in order to better understand the ${}^6\text{Li}$ proton spectrum of NMWD and above all to evaluate the background contribution to the proton energy

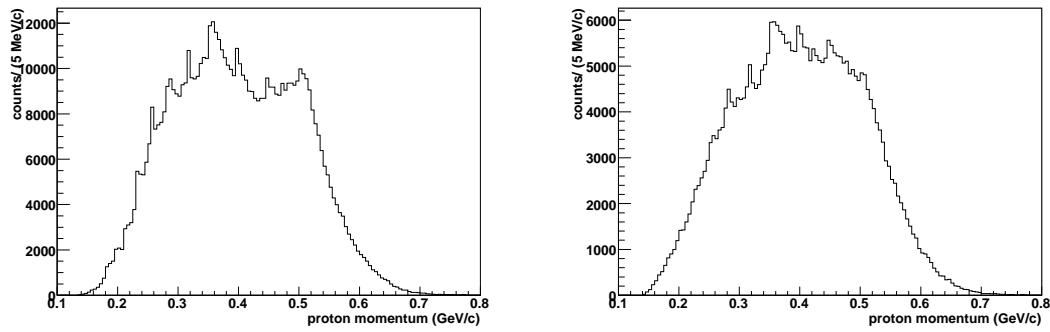


Figure 5.15: Inclusive proton spectra measured following the K^- capture at rest from ${}^6\text{Li}$ (left) and ${}^7\text{Li}$ (right).

spectrum.

As for the ${}^7\text{Li}$ case, the first step of the proton-induced NMWD analysis is the study of the π^- momentum inclusive spectra measured for the two ${}^6\text{Li}$ targets and the experimental identification of the ${}^5_{\Lambda}\text{He}$ formation. The events included in the π^- momentum inclusive spectra were selected using the same criteria chosen for the analysis of ${}^7\text{Li}$ and the result of the sum of the two ${}^6\text{Li}$ targets contribution is shown in Fig. 5.16.

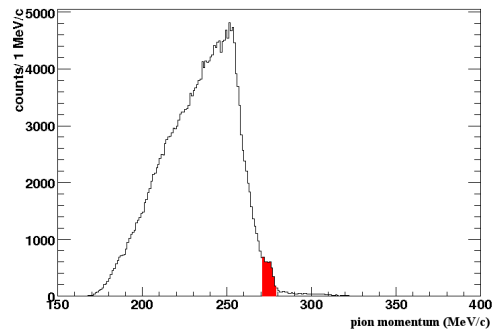


Figure 5.16: Total π^- inclusive spectrum obtained as the sum of the two ${}^6\text{Li}$ targets contribution .

The inclusive π^- spectrum shows a knee at a momentum value of 275 MeV/c. This value corresponds to the formation of the ${}^5_{\Lambda}\text{He}$ and it is fully

consistent with the value reported in Tab.5.1. The region selected in red in Fig.5.16 goes from 272 MeV/c to 278 MeV/c and it evidences the interval chosen for the *g.s.* region identification. Furthermore, it is important to notice that using, in the selection of the events, the cut on the distance between the K^- interaction vertex and the extrapolated π^- track point requiring a distance less than 0.3 cm the signal to background ratio was increased of a factor 3.

Requiring for all the events a positive track, identified as a proton in the spectrometer, emitted from the same vertex of the negative pion the spectrum in Fig.5.17 is obtained.

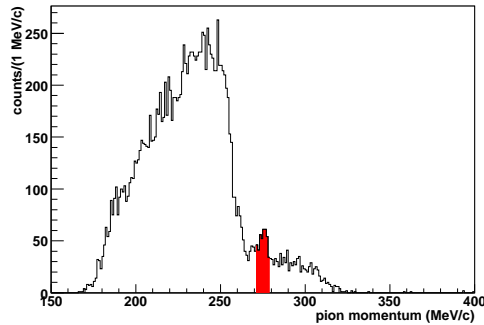


Figure 5.17: π^- spectrum for events with an additional proton track, from the two ${}^6\text{Li}$ targets.

By the request of an additional proton a clear peak can be observed in the bound region of the π^- momentum spectrum corresponding to the formation of the ${}^5_\Lambda\text{He}$ hypernucleus (red area), which subsequently decays following the non-mesonic decay mode.

The energy spectrum, not acceptance corrected, of the protons coming from the NMWD of ${}^5_\Lambda\text{He}$ is shown in Fig. 5.18 (top); the spectrum is the sum of the protons coming from the two ${}^6\text{Li}$ targets and shows a camel-back double humped structure, with a second maximum around 120 MeV. About 370 events populate the spectrum.

After the acceptance correction one gets the spectrum of Fig. 5.18 (bottom): the signal at ~ 80 MeV emerges and the region in the 20-40 MeV interval rises considerably, as a consequence of the FSI and of the two-nucleons

induced non mesonic weak decay process.

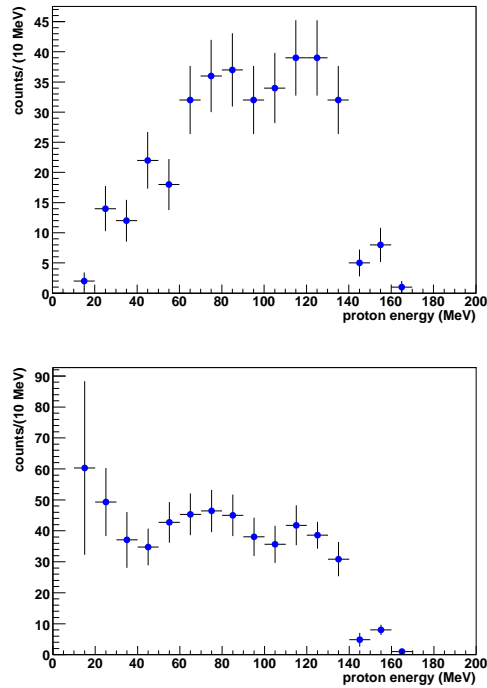


Figure 5.18: Top: energy spectrum, non acceptance corrected, of the protons emitted in coincidence with a π^- emitted after the formation of the ${}^5_{\Lambda}\text{He}$ with the ${}^6\text{Li}$ target; bottom: energy spectrum, acceptance corrected, of the protons coming from the NMWD of the ${}^5_{\Lambda}\text{He}$.

Comparing the proton spectra obtained for the ${}^7_{\Lambda}\text{Li}_{g.s.}$ and the ${}^5_{\Lambda}\text{He}$ one realizes that the background shapes for the two proton spectra may be very different. This difference can be addressed to the different absorption reactions which can occur, in the ${}^6\text{Li}$ case, on a cluster substructure.

Taking into account this last remark, for the background evaluation it was necessary to simulate the stopped K^-np absorption process taking into account the peculiar cluster (α - d) structure of the ${}^6\text{Li}$ nucleus.

In fact, by simply using the MonteCarlo calculation of the interaction of a K^- stopped with an uncorrelated np pair it is not possible to reproduce the background shape of the spectrum in Fig 5.17.

The study of the background was carried out implementing, in the FIN-

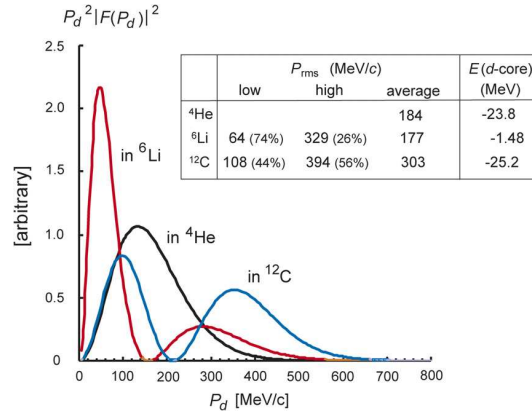


Figure 5.19: Momentum distribution of a quasi- d in typical light nuclei: ${}^4\text{He}$, ${}^6\text{Li}$ and ${}^{12}\text{C}$. The binding energy of quasi- d in these nuclei and the rms momenta are shown in the inset. This calculation is taken from [94].

UDA simulation code, a MonteCarlo generator that takes into account the momentum distribution of a deuteron inside a ${}^6\text{Li}$ nucleus. The nucleus is assumed to be at rest and the direction of the deuteron is chosen randomly, while the deuteron momentum is extracted sampling the function reported in Fig.5.19. From the picture one sees that in the case of the ${}^6\text{Li}$ nucleus the momentum distribution of a deuteron cluster has two peaks: one at low momentum (≤ 100 MeV/c) due to a single deuteron, and another at higher momentum (~ 300 MeV/c) determined by the "quasi"-deuteron contained in the α cluster ("quasi" here indicates a few-nucleon cluster in a composite nucleus). The events simulated using this MonteCarlo generator were filtered through the FINUDA reconstruction program and analyzed with the same criteria applied to the data. The result achieved in this way is showed in Fig. 5.20. The spectrum of Fig.5.20 represents the comparison between the data (black) and the simulation (red). The red momentum distribution was obtained normalizing as always on the spectrum tail beyond the selected $g.s.$ region of the ${}^5_\Lambda\text{He}$ ($p_{\pi^-} \geq 278$ MeV/c).

Extracting the spectrum of the protons emitted in coincidence with a π^- from the simulation data we can evaluate the background contribution to the proton spectrum; the two proton spectra obtained from the data analysis and the simulation, superimposed, are showed in Fig. 5.21. They are

acceptance corrected and the errors are calculated as statistical only. In particular, using the simulation for the background evaluation and simulating a number of events (4 millions) which is very much higher than the events that populates the data spectrum, a very small error on the determination of the events in each bin is obtained.

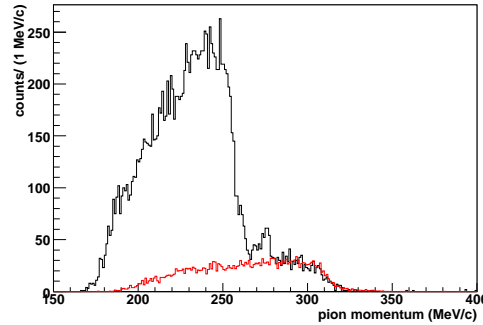


Figure 5.20: π^- momentum spectrum for events with an additional proton track (in black) and superimposed (red histogram) the contribution to the spectrum from the $K^- np$ channel.

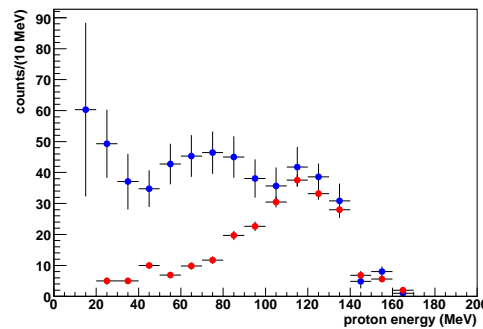


Figure 5.21: Energy spectrum of the protons coming from the background absorption process (red dots) superimposed to the acceptance corrected proton spectrum obtained from the data (blue dots) for the ${}^5_{\Lambda}\text{He}$.

Subtracting the red proton spectrum from the blue one we obtain the spectrum of Fig. 5.22. A further step of the analysis was the test of the

compatibility between the proton energy spectrum of ${}^5_{\Lambda}\text{He}$ obtained from ${}^7\text{Li}$ targets analysis (on right of Fig.5.14) and the last one obtained with the analysis of ${}^6\text{Li}$ targets (Fig. 5.22) in order to verify if the two spectra can be added. The two ${}^5_{\Lambda}\text{He}$ proton spectra were normalized to area beyond 15 MeV in order to have spectra *normalized per proton-induced decays* and to test their agreement in shape. The result of the normalization is reported in Fig. 5.23, where the blue dots represent the proton energy spectrum coming from ${}^7\text{Li}$ targets and the red squares indicate the proton spectrum obtained from ${}^6\text{Li}$ targets.

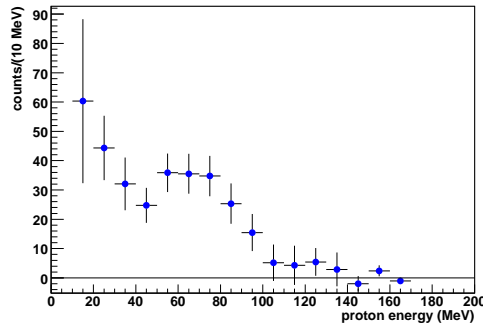


Figure 5.22: Proton energy spectrum coming from the NMWD of ${}^5_{\Lambda}\text{He}$ after the background subtraction.

In order to estimate the compatibility of the spectra of Fig. 5.23 the Kolmogorov-Smirnov test was applied to the data. This test is used to determine whether two one-dimensional distributions differ and it is one of the most useful and general nonparametric methods for comparing two samples, as it is sensitive to differences in both location and shape of the compared distributions. The application of this test returns a probability of compatibility between the two histograms. A value close to one indicates very similar histograms and a value near to zero means that it is very unlikely that the two arose from the same parent distribution.

The Kolmogorov-Smirnov test applied to the data shown in Fig.5.23 gives a value of probability $P=0.89$ at a confidence level of 95% and this means that the two ${}^5_{\Lambda}\text{He}$ proton spectra are fully compatible and they can be added.

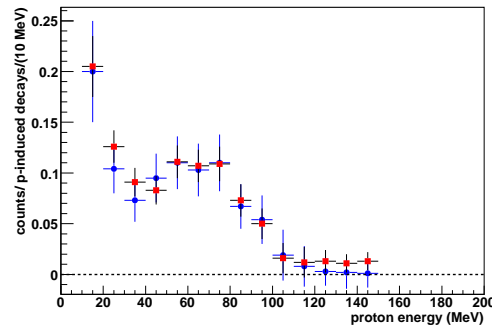


Figure 5.23: Proton energy spectrum of ${}_{\Lambda}^5\text{He}$ obtained from ${}^7\text{Li}$ targets analysis (blue dots) and the one obtained with the analysis of ${}^6\text{Li}$ targets (red squares). The two spectra are normalized to area beyond 15 MeV.

The sum of the two spectra is shown in Fig. 5.24.

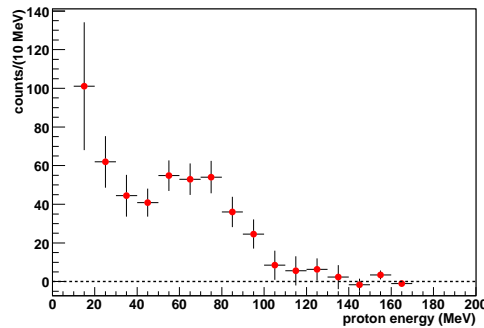


Figure 5.24: Total proton energy spectrum of ${}_{\Lambda}^5\text{He}$ obtained adding the spectrum obtained from ${}^7\text{Li}$ targets analysis (on right of Fig.5.14) and the one obtained with the analysis of ${}^6\text{Li}$ targets (Fig. 5.22).

5.4 New analysis of ${}_{\Lambda}^{12}\text{C}$

The analysis of the data collected during the second FINUDA data taking was carried out using the analysis tools described in the Cap.4 and developed after the period in which I analyzed the ${}_{\Lambda}^{12}\text{C}$ reaching the results described in Sec. 5.1. In particular the main differences between the two analyses are:

- the new pattern recognition for tracks that do not reach the straw tubes crown (the so-called *short tracks*); this implementation gives the opportunity to improve the acceptance of the spectrometer, as well as the efficiency of the reconstruction algorithm;
- a more precise Particle IDentification method for the proton selection (described in Sec. 4.4);
- the introduction of the quality cut on the distance between the π^- extrapolated track point and the K^- vertex; in particular in the analysis described in the following for the ^{12}C targets all the events in which the distance is less than 0.3 cm were selected obtaining an improvement of the signal to background ratio of a factor 3.

Using the new selection criteria listed above the inclusive π^- momentum spectrum of each ^{12}C target of the first data taking was analyzed in order to identify the momentum region related to the *g.s.* formation of the $^{12}_{\Lambda}\text{C}$.

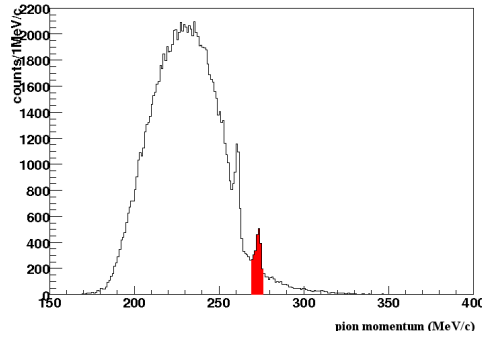


Figure 5.25: Total π^- inclusive momentum spectrum obtained as the sum of the three ^{12}C ; the red region corresponds to the $^{12}_{\Lambda}\text{C}_{g.s.}$.

In Fig. 5.25 the sum of the three ^{12}C is shown; in the π^- spectrum two peaks corresponding to the formation of the $^{11}_{\Lambda}\text{B}$ (262 MeV/c) in its ground state and of the ground state of the $^{12}_{\Lambda}\text{C}$ (272.7 MeV/c) appear clearly. Furthermore it is possible to notice that there is a low background contribution in the region beyond the kinematical limit of the $^{12}_{\Lambda}\text{C}$ formation reaction (beyond 276 MeV/c) and this is the effect of the cut on the distance between

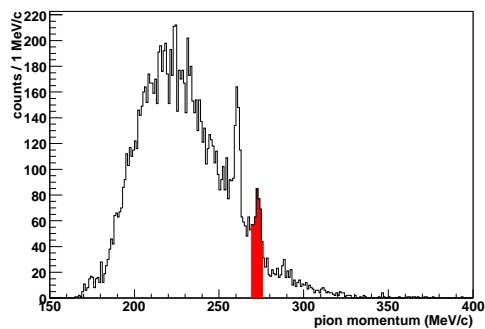


Figure 5.26: $^{12}_\Lambda C$ momentum spectrum for the events in which a π^- is detected in coincidence with a proton from the same K^- vertex. Red region: $^{12}_\Lambda C_{g.s.}$ momentum interval.

the π^- extrapolated track point and the K^- vertex. The red region of the π^- momentum spectrum corresponds to the momentum interval chosen for the $^{12}_\Lambda C_{g.s.}$ and it extends from 270 MeV/c to 276 MeV/c. Then for the events in the selected region (*g.s.*) a proton was required for each K^- vertex in the target. As for ^7Li and ^6Li analysis the π^- are *long tracks* only, while the protons can be either *long* or *short tracks*.

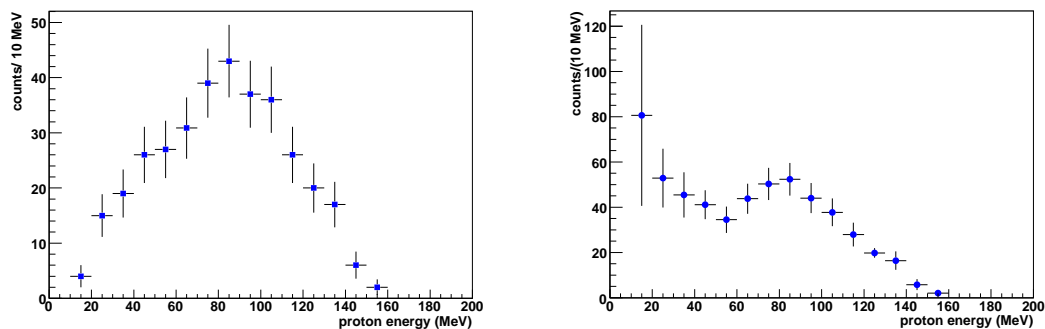


Figure 5.27: Left: energy spectrum, non acceptance corrected, of the protons emitted in coincidence with a π^- coming from the $^{12}_\Lambda C$. s.; right: result of the acceptance correction applied to the proton energy spectrum showed on the left of this figure.

The spectrum of Fig. 5.26 shows the π^- momentum spectrum after the coincidence requirement and it corresponds to the sum of the three ^{12}C targets data.

Selecting the protons emitted in coincidence with a π^- from the $g.s.$ region the spectrum on the left of Fig 5.27 is obtained and after the acceptance correction I got for the three ^{12}C targets the spectrum on the left of Fig 5.27. The spectrum carried out with this second analysis, performed using a new pattern recognition code, gives as result a proton energy spectrum in which the signal at 80 MeV is always present and the rise of the lower proton energy part appears as consequence of the FSI and multinucleons induced effects. The errors reported in the spectrum are statistical only and determined taking into account the contribution of the statistical errors on the data and the error due to the acceptance evaluation. The shape of the spectrum is more similar to that of the ${}^7_{\Lambda}\text{Li}_{g.s.}$ than that of the ${}^5_{\Lambda}\text{He}$.

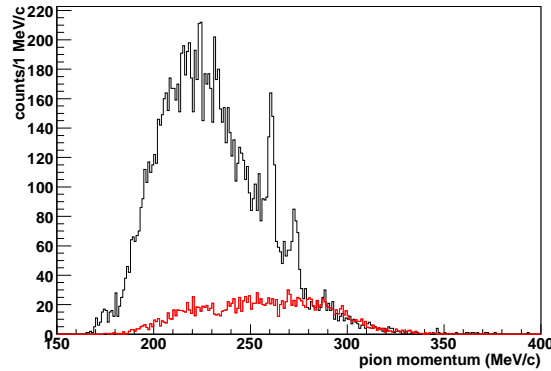


Figure 5.28: ${}^{12}_{\Lambda}\text{C}$ momentum spectrum for π^- detected in coincidence with a proton (black) and in (red) the simulated spectrum of the Knp absorption reaction.

The evaluation of the background was performed, like for all other analyses, performing a MonteCarlo simulation of the $K^- + np \rightarrow \Sigma^- + p$ absorption reaction using the same program used for the reconstruction of the data. In the simulation one assumes that the K^- interacts on a np pair extracted, with Fermi momentum, out of a ^{12}C nucleus at rest. In Fig. 5.28 we find, in black, the momentum spectrum of the π^- detected in coincidence with a

proton and in red, superimposed, the π^- simulated spectrum obtained after the application of the same selection criteria adopted for the real data and normalized beyond 276 MeV/c.

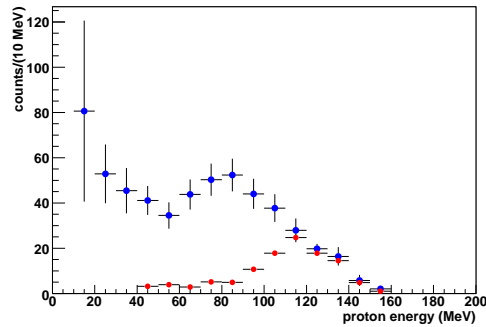


Figure 5.29: Blue dots: proton energy spectrum, acceptance corrected, of ${}_{\Lambda}^{12}\text{C}$ *g.s.*; red dots: proton energy spectrum from simulation of the K^- absorption by two nucleons, emitted in coincidence with pions in the *g.s.* range (270 MeV/c–276 MeV/c)

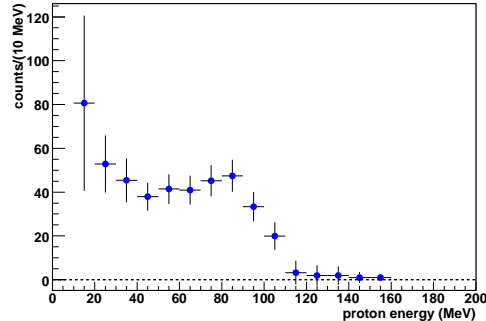


Figure 5.30: Energy spectrum of the protons coming from the NMWD of ${}_{\Lambda}^{12}\text{C}$ in its *g.s.* after the background subtraction.

The background subtraction from the proton energy spectrum of Fig. 5.27 is performed selecting the protons in coincidence with a π^- , coming from the np absorption mechanism evaluated by the MonteCarlo simulation. In Fig. 5.29 the comparison between the proton data and the simulated protons is shown, while in Fig 5.30 the result of the background subtraction

is reported.

Chapter 6

Results and comparisons

The first part of this last chapter is dedicated to the calculation of the ratio R_p of the total number of protons with energy larger than 15 MeV to the total number of produced Hypernuclei for the ${}^5_{\Lambda}\text{He}$, ${}^7_{\Lambda}\text{Li}$ and ${}^{12}_{\Lambda}\text{C}$ hypernuclei with a comparison of the Γ_p values determined by other experiments and calculated by the theoreticians. After this calculation a comparison of the FINUDA proton spectra with the theoretical expectations and the KEK spectra is presented in order to draw my conclusions.

6.1 R_p calculation

The evaluation of the ratio R_p of the total number of protons with energy larger than 15 MeV to the total number of produced Hypernuclei comes out as follows:

- definition of the region of interest in each inclusive π^- spectrum;
- evaluation of the number of hypernuclei produced in the region of interest;
- extraction of the number of protons emitted in the NMWD and detected in coincidence with a π^- coming from the hypernucleus formation;

The regions of interest in each inclusive π^- spectrum of the three studied hypernuclei was defined as the momentum interval corresponding to the

formation of the hypernucleus in its *g.s.*. The regions of interest chosen for each target and employed in the analysis of this thesis are listed in Tab. 6.1.

Target material	Hypernucleus	region of interest (MeV/c)
^{12}C	$^{12}_{\Lambda}\text{C}$	270-276
^6Li	$^5_{\Lambda}\text{He}$	272-278
^7Li	$^7_{\Lambda}\text{Li}$	272-278

Table 6.1: Momentum interval corresponding to the formation of the studied hypernuclei.

Integrating the number of π^- , detected in the momentum regions reported in Tab.6.1, it is possible to estimate the number of produced hypernuclei. For the subtraction of the background contribution to the *g.s.* I took advantage of the simulation of the K^-np absorption process performed for each studied target and widely discussed in the data analysis chapter. The result of this calculation is reported in Tab. 6.2.

Target material	Hypernucleus	Number of π^-
^{12}C	$^{12}_{\Lambda}\text{C}$	1274 ± 40
^6Li	$^5_{\Lambda}\text{He}$	1848 ± 46
^7Li	$^7_{\Lambda}\text{Li}$	1176 ± 36
^7Li	$^5_{\Lambda}\text{He}$	1176 ± 36

Table 6.2: Number of π^- detected in the region of the *g.s.* of each studied hypernucleus; the statistical errors are also reported.

Finally the number of protons coming from the the NMWD was evaluated considering the total number of protons detected in coincidence with a π^- coming from the defined region of interest and subtracting the contribution due to the background reaction.

The protons coming from the background reaction were extracted from the

MonteCarlo simulation done for each hypernucleus and also used for the evaluation of the π^- background. The values thus estimated are shown in Tab. 6.3.

Target material	Hypernucleus	Number of protons
^{12}C	$^{12}_{\Lambda}\text{C}$	217 ± 16
^6Li	$^5_{\Lambda}\text{He}$	164 ± 14
^7Li	$^7_{\Lambda}\text{Li}$	159 ± 14
^7Li	$^5_{\Lambda}\text{He}$	90 ± 11

Table 6.3: Number of proton coming from the NMWD of the different studied hypernuclei when they are in their *g.s.*

Taking into account the previous calculations it is possible to estimate the ratio R_p using the following relation:

$$R_p = \frac{N_p^{NMWD}}{N_{hyp}} \quad (6.1)$$

where N_p^{NMWD} indicates the number of protons coming from the NMWD and N_{hyp} is the total number of hypernuclei produced. These two quantities are deduced respectively from the following equations:

$$N_p^{NMWD} = \frac{N_p^{detected}}{\epsilon'_p} \quad (6.2)$$

$$N_{hyp} = \frac{N_{hyp}^{detected}}{\epsilon_{\pi^-}} \quad (6.3)$$

$N_p^{detected}$ and $N_{hyp}^{detected}$ indicate respectively the number of protons and hypernuclei derived from the experimental spectra and reported, respectively in Tab.6.3 and Tab.6.2; ϵ'_p is the global acceptance of the FINUDA apparatus for the protons detected in coincidence with a π^- and consequently can be written as the product of the proton acceptance and the negative pion acceptance $\epsilon'_p = \epsilon_p \epsilon_{\pi^-}$. The relations (6.2) and (6.3) can be inserted in the equation 6.1 thus obtaining:

$$R_p = \frac{N_p^{detected}}{(N_{hyp}^{detected})(\epsilon_p)} \quad (6.4)$$

the value of ϵ_p was estimated by means of the Monte Carlo simulation, described in Sec 4.3, followed by the reconstruction of the simulated events using the same reconstruction algorithm used for the real data. The results obtained for the estimation of R_p are listed in Tab. 6.4. The R_p values of ${}^5_\Lambda\text{He}$, obtained studying the NMWD for ${}^6\text{Li}$ and ${}^7\text{Li}$ targets, are compatible within the errors. In the last row of Tab. 6.4 a single value of R_p for ${}^5_\Lambda\text{He}$ is reported and it is the weighted mean of the two values of R_p found for the ${}^6\text{Li}$ and ${}^7\text{Li}$ targets.

Target material	Hypernucleus	R_p (energy ≥ 15 MeV)
${}^{12}\text{C}$	${}^{12}_\Lambda\text{C}$	0.43 ± 0.07
${}^6\text{Li}$	${}^5_\Lambda\text{He}$	0.28 ± 0.09
${}^7\text{Li}$	${}^7_\Lambda\text{Li}$	0.37 ± 0.09
${}^7\text{Li}$	${}^5_\Lambda\text{He}$	0.21 ± 0.12
weighted mean of ${}^6\text{Li}$ and ${}^7\text{Li}$	${}^5_\Lambda\text{He}$	0.25 ± 0.07

Table 6.4: R_p values calculated by means the relation (6.4) for the proton induced NMWD of the studied hypernuclei. The errors reported in the table are statistical only.

Concerning the value of R_p found for the ${}^7_\Lambda\text{Li}$ hypernucleus this is the first absolute measurement ever done before. Furthermore it is important to notice that the values measured for the ${}^5_\Lambda\text{He}$ analyzing both the ${}^7\text{Li}$ target and the ${}^6\text{Li}$ target are fully compatible within the statistical errors.

These values of R_p are a guess of the Γ_p decay rate which can be determined only when FSI and two-nucleon induced weak decays contribution can be completely neglected. Due to the fact that the proton spectra from NMWD of ${}^5_\Lambda\text{He}$, ${}^7_\Lambda\text{Li}$, and ${}^{12}_\Lambda\text{C}$, show a low energy rise, due to the final state interactions (FSI) and/or to two nucleon induced weak decays it is possible to calculate the number of proton emitted respect to the produced hypernuclei

(R_p). The values of R_p can be compared with some theoretical evaluation and experimental results published in [95] and listed in Tab.6.5. The theoretical values were calculated by the authors in the framework of the one-meson-exchange (OME) model including the π , $\pi+K$ and all mesons contributions. In each calculation different values of the NNK coupling constants are implemented through the NSC97a [96] and NSC97f [96] model, indicated in Tab.6.5 respectively as a and f .

${}^5_{\Lambda}\text{He}$	Γ_p	
	a	f
π	0.390	0.391
$\pi + K$	0.211	0.157
all	0.317	0.218
exp	0.21±0.07 [97]	
${}^{12}_{\Lambda}\text{C}$	Γ_p	
	a	f
π	0.707	0.696
$\pi + K$	0.403	0.308
all	0.564	0.414
exp	0.31 $^{+0.18}_{-0.11}$ [98]	

Table 6.5: Previous theoretical and experimental evaluation of the Γ_p value considered in order to have a comparison for the FINUDA experimental measurements.

Comparing the experimental values, achieved for R_p , for ${}^{12}_{\Lambda}\text{C}$ and ${}^5_{\Lambda}\text{He}$, with the theoretical values of Γ_p listed in 6.5 the suggestion is that the FINUDA experimental values are well estimated including in the calculation the contribution of all the meson and using the NSC97f model.

6.2 Experiments vs Theory

The more recent experimental results concerning the study of the NMWD of Λ -hypernuclei have been achieved in various experiments performed at

the KEK laboratory with the SKS spectrometer.

In particular, in a recent paper Okada et al. [99] published high statistics proton spectra for the ${}^{12}_{\Lambda}\text{C}$ and ${}^5_{\Lambda}\text{He}$. In Fig. 6.1 the comparison between the FINUDA spectrum obtained for ${}^{12}_{\Lambda}\text{C}_{g.s.}$ (red squares) and the KEK proton spectrum (blue dots) is shown, while in Fig. 6.2 the comparison for ${}^5_{\Lambda}\text{He}$ is reported. The FINUDA ${}^5_{\Lambda}\text{He}$ proton spectrum is the sum of the ${}^5_{\Lambda}\text{He}$ proton spectra extracted from the analysis of ${}^7\text{Li}$ and ${}^6\text{Li}$ targets (total spectrum of Fig. 5.24).

Concerning the results obtained for the ${}^7_{\Lambda}\text{Li}$ there is no possibility of making a comparison with other experimental spectra because the spectrum reported in this thesis is the first one measured for this hypernucleus.

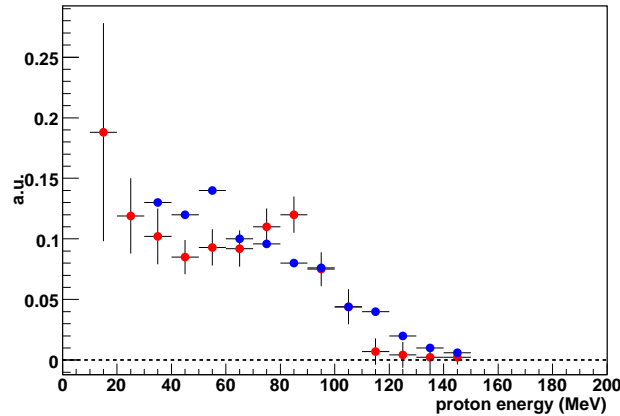


Figure 6.1: Red dots: FINUDA proton spectrum from proton-induced NMWD for ${}^{12}_{\Lambda}\text{C}_{g.s.}$; blue dots: result achieved for the ${}^{12}_{\Lambda}\text{C}_{g.s.}$ at the KEK experiment; the two spectra are normalized to area beyond 35 MeV.

The proton spectra of Figs. 6.1 and 6.2 were carried out normalizing the spectra to area beyond 35 MeV and it is possible to notice two main differences : first of all ${}^{12}_{\Lambda}\text{C}_{g.s.}$ proton spectra obtained at KEK is quite flat in the region where one expects the maximum (~ 80 MeV) and on the contrary the FINUDA spectrum shows the bulk of the signal around 80 MeV, moreover both the KEK proton spectra have a high kinetic energy proton threshold of ~ 35 MeV due to the use of thick target and the energy loss inside the

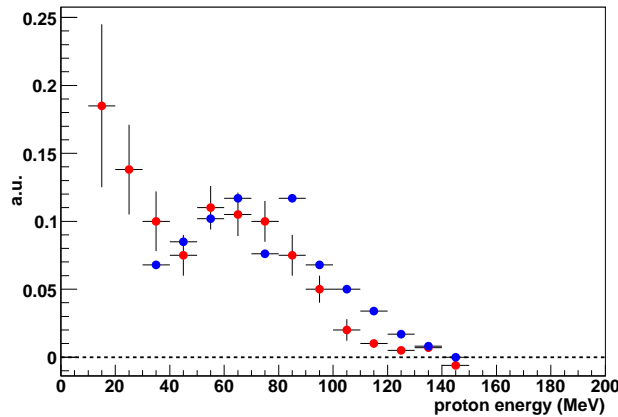


Figure 6.2: Red dots: FINUDA proton spectrum from proton-induced NMWD for ${}^5_{\Lambda}\text{He}$; blue dots: result achieved for the ${}^5_{\Lambda}\text{He}$ at the KEK experiment; the two spectra are normalized to area beyond 35 MeV.

detector that prevent to do realistic consideration about the contribution of the FSI to the NMWD process. At the contrary the FINUDA proton spectra have a very low proton energy threshold (~ 15 MeV) thus giving the possibility to explore experimentally, for the first time, the contribution of the FSI in the low energy region of the proton spectra.

In order to estimate the compatibility between FINUDA and KEK proton spectra coming from the one-proton induced NMWD the Kolmogorov-Smirnov (K-S) test was applied to the data. For the ${}^{12}_{\Lambda}\text{C}_{g.s.}$ the K-S test gives a confidence level of 20%, while for the ${}^5_{\Lambda}\text{He}$ I found a value of confidence level of 75%.

These results indicate that there is a higher compatibility between the KEK ${}^5_{\Lambda}\text{He}$ data and the ${}^5_{\Lambda}\text{He}$ spectra obtained from the analysis described in this work respect to the ${}^{12}_{\Lambda}\text{C}_{g.s.}$ proton spectra.

In the last years, besides a big effort on the experimental side, the study of NMWD was characterized by a lot of activity also on the theoretical side. In a quite recent review Garbarino *et al.* [100] presented a systematic study of the non mesonic weak decay of ${}^{12}_{\Lambda}\text{C}_{g.s.}$ and ${}^5_{\Lambda}\text{He}$. This theoretical work is based on a nuclear matter formalism extended to finite nuclei via the local density approximation (LDA) and on the one-meson exchange (OME) weak

transition potential to describe both the one- and two-nucleon induced decays.

In addition the contribution of the FSI was considered through an inter-nuclear cascade simulation in order to have an estimation of the nucleon propagation inside the residual nucleus.

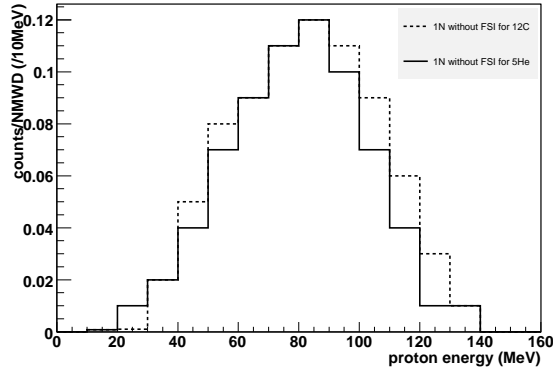


Figure 6.3: proton kinetic energy spectra corresponding to the decay of $^5_{\Lambda}\text{He}$ (continuous line) and $^{12}_{\Lambda}\text{C}$ (dashed line) obtained without the contribution of the FSI.

Fig. 6.3 shows the proton kinetic energy spectra corresponding to the decay of $^5_{\Lambda}\text{He}$ (continuous line) and $^{12}_{\Lambda}\text{C}$ (dashed line) obtained when the FSI is not implemented in the calculation; the distribution of the one-nucleon induced primary protons shows a peak around 80 MeV mainly due to the kinematics of the weak decay protons, without any distortion in the low energy part of the spectrum.

The inclusion, in the calculation, of nucleon FSI provide the results given in Figs. 6.4 and 6.5. In these figures the theoretical calculations compared with the FINUDA experimental results is reported (red dots).

The dotted lines of Figs. 6.4 and 6.5 correspond to the theoretical calculation of the one nucleon induced NMWD, once the two-nucleon induced channel is also included. The curves were normalized beyond 35 MeV.

For what concerne the $^{12}_{\Lambda}\text{C}$ proton spectrum (Fig. 6.4) from the comparison with the theoretical calculation one deduces that in the region beyond

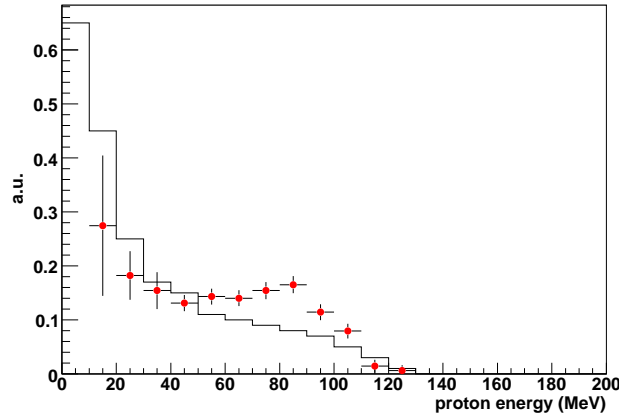


Figure 6.4: Red dots: experimental proton spectra of $^{12}_{\Lambda}\text{C}$ normalized *per p-induced non mesonic weak decay*; Black curve: theoretical calculation for the proton energy spectrum of $^{12}_{\Lambda}\text{C}$ performed with the addition of the FSI contribution.

~ 70 MeV the shape of the experimental data is not reproduced and in the low energy region, where the FSI becomes competitive it seems that the contribution of this process is too large to reproduce the data.

In fact, even if the data show, below 40 MeV, a smearing of the distribution due to the FSI and to the two-nucleons induced NMWD process, the comparison suggests that this smearing is not so evident like it appears from the theoretical expectations. The K-S test for the comparison between the data and the theoretical calculation of $^{12}_{\Lambda}\text{C}$ provides a value of confidence level of 5% that indicate a really low compatibility. If we look to the comparison reported in Fig.6.5 for the $^5_{\Lambda}\text{He}$ proton spectrum we found that the shape of the experimental data distribution differs from the theoretical curves.

In particular it looks that for the low energy part of the spectrum the rise is more evident in the proton data respect to the theoretical calculation while for the higher energy bins (≥ 90 MeV) the theoretical spectrum is wider than the experimental one and the bump around 80 MeV is less pronounced.

The K-S test applied to the $^5_{\Lambda}\text{He}$ data gives a value of confidence level of 80%. One of the explanation of this difference in the shape for $^5_{\Lambda}\text{He}$ proton

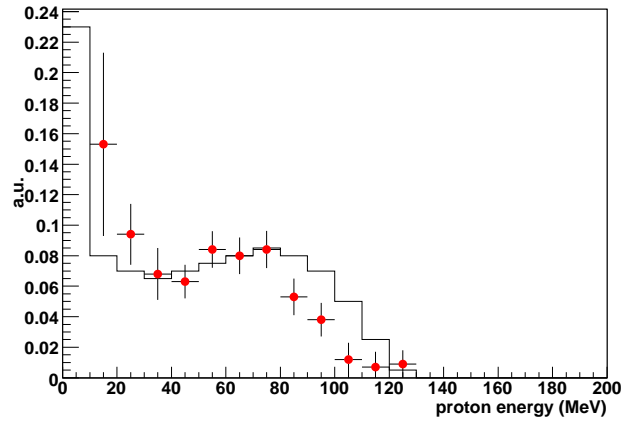


Figure 6.5: Red dots: experimental proton spectra of ${}^5_{\Lambda}\text{He}$ normalized *per p-induced non mesonic weak decay*; Black curve: theoretical calculation for the proton energy spectrum of ${}^5_{\Lambda}\text{He}$ performed with the addition of the FSI contribution.

spectrum is reported in [100] by the authors. They, in fact assert that accounting for nucleon final state interactions effects in light residual nuclei (as those required to treat ${}^5_{\Lambda}\text{He}$) through Monte Carlo techniques is questionable and for this reason the theoretical calculation presented for ${}^5_{\Lambda}\text{He}$ should be considered less realistic than the corresponding ones for ${}^{12}_{\Lambda}\text{C}$.

It emerges that further experimental and theoretical confirmations are needed and that the FINUDA experimental results, unlike the KEK data, give more complete information about the proton spectra of the NMWD, thanks to the low proton energy threshold.

Moreover the disagreement with the theoretical calculation is not too strong for ${}^5_{\Lambda}\text{He}$ and very strong for ${}^{12}_{\Lambda}\text{C}$ thus suggesting a deeper study of this physical channel and the need of both experimental and theoretical efforts in order to reach a full consistency between the experimental data and the theoretical predictions.

Chapter 7

Conclusions

The study of the proton spectra from hypernuclear non mesonic weak decay has been performed analyzing the data collected during the first and the second FINUDA data taking period. In particular the analysis has been carried out for three different hypernuclei: ${}^5_{\Lambda}\text{He}$, ${}^7_{\Lambda}\text{Li}$ and ${}^{12}_{\Lambda}\text{C}$.

The proton spectra obtained from the analysis of the FINUDA data have a very low energy threshold of 15 MeV giving the possibility to study a proton energy range never studied before and to make comparison with the theoretical expectation on the FSI contribution to the proton spectra. It is important to recall that the previous spectra obtained from the KEK data, collected at SKS spectrometer, show a higher energy cut at 35 MeV, due to the use of quite thick targets and to the energy loss in the detectors.

The ratio R_p of the total number of protons with energy larger than 15 MeV to the total number of produced Hypernuclei reported for ${}^5_{\Lambda}\text{He}$ and ${}^{12}_{\Lambda}\text{C}$ represent the first experimental measurement for these two hypernuclei. Moreover the value of R_p calculated for ${}^7_{\Lambda}\text{Li}$ has been measured for the first time.

Furthermore the results achieved in this thesis for the ${}^5_{\Lambda}\text{He}$ and the ${}^{12}_{\Lambda}\text{C}$ have been compared with the previous KEK experimental results. From this comparison a discrepancy emerges for the ${}^{12}_{\Lambda}\text{C}$ proton spectrum, while the proton spectra of ${}^5_{\Lambda}\text{He}$ seem to be more compatible.

Concerning the amount of FSI, a comparison of the FINUDA data with the theoretical expectations has been done. From this comparison it emerges

that the FSI contribution introduced in the theoretical calculations is too large to reproduce the experimental data.

List of Tables

2.1	Table of typical lifetimes for different interactions.	25
3.1	DAΦNE design values	42
3.2	FINUDA magnet main features	51
5.1	π^- momentum corresponding to the Λ binding energy (B_Λ) of the hypernucleus ground state. The B_Λ values have been calculated or extrapolated from experimental values ([57] and [58]).	77
6.1	Momentum interval corresponding to the formation of the studied hypernuclei.	104
6.2	Number of π^- detected in the region of the <i>g.s.</i> of each studied hypernucleus; the statistical errors are also reported. . . .	104
6.3	Number of proton coming from the NMWD of the different studied hypernuclei when they are in their <i>g.s.</i>	105
6.4	R_p values calculated by means the relation (6.4) for the proton induced NMWD of the studied hypernuclei. The errors reported in the table are statistical only.	106
6.5	Previous theoretical and experimental evaluation of the Γ_p value considered in order to have a comparison for the FINUDA experimental measurements.	107

List of Figures

1.1	Mass number dependence of the Λ binding energy [2]	8
1.2	Kinematics of the reactions (1.1), (1.2) and photoproduction for forward Λ emission ($\theta_L=0^\circ$).The momentum transferred to the hyperon is plotted as a function of the incoming particle (K^- , π^+ or e) in the Laboratory system.	10
1.3	Hypernuclear production cross section for typical reactions versus momentum transfer.	14
1.4	A schematic presentation of three strangeness producing reactions used to study hypernuclei.	16
1.5	Excitation spectrum of ${}^1_6\Lambda\text{O}$ (on left) and ${}^{27}_\Lambda\text{Al}$ (on right).	18
1.6	Theoretical spectrum: momentum of emitted π^- due to interaction between K^-_{stop} and nucleus [10].	19
1.7	The excitation spectrum for the ${}^{89}\text{Y}(\pi^+, K^+){}^8_9\Lambda\text{Y}$ reaction at $p_\pi = 1.05 \text{ GeV}/c$ and $\theta_K = 10^\circ$, from the AGS experiment. The curves represent theoretical calculations. (From Ref. [11].)	21
1.8	The excitation spectrum for the ${}^{89}\text{Y}(\pi^+, K^+){}^8_9\Lambda\text{Y}$ reaction obtained at KEK by E369 experiment [12]	22
2.1	One nucleon (on left) and two-nucleons (on right) induced Λ decay in nuclei	29
2.2	Lifetime of the Λ -hyperon as measured for several Λ -hypernuclei.	33
2.3	Total non mesonic decay widths of Λ -hypernuclei. For details see the text.	34
2.4	The Γ_n/Γ_p ratio of Λ -hypernuclei.	35

2.5	(a),(b): the yields of the np and nn coincidence events as a function of the energy sum of the pair nucleons. (c),(d): The upper panel shows the yields of the NN coincidence events plotted as function of the opening angle between the two nucleons. The lower panel depicts the normalized yields of the np and nn coincidence per NMWD.	37
2.6	Neutron (filled circle) and proton (open circle) energy spectra per NMWD of (a) ${}^5_{\Lambda}He$ and (b) ${}^{12}_{\Lambda}C$ with the neutron spectrum of (c) ${}^{89}_{\Lambda}Y$. The errors are statistical. The dashed histogram in the top figure shows the the neutron spectrum per NMWD calculated by Garbarino et al. [100] in which FSI effect and the 2N-induced process were taken into account.	38
3.1	Geometrical design of the DAΦNE main rings (top view).	43
3.2	DAΦNE statistics during the first FINUDA data taking.	44
3.3	DAΦNE statistics during the second FINUDA data taking.	45
3.4	Layout of the FINUDA apparatus.	46
3.5	FINUDA vertex region.	47
3.6	FINUDA target set-up used during the first data taking.	48
3.7	Garfield simulation results for LMDs drift cells.	49
3.8	Layout of FINUDA internal region: coaxial to the beam axis (perpendicular to the picture) several layers of sensitive detectors are located. From the center outwards: beryllium beam pipe, TOFINO (12-slab thin scintillator array), Si microstrip modules inner array (ISIM), targets, Si microstrips outer array (OSIM). The labels close to the targets indicate their composition.	52
4.1	An event in which a <i>short track</i> is reconstructed in the FINUDA spectrometer using the track pattern recognition with 3 points.	62
4.2	A typical <i>long track</i> reconstructed in the FINUDA spectrometer using the track pattern recognition with 4 points.	63

4.3	Simulated π^- inclusive spectrum for background reactions occurring at the K_{stop}^- vertex.	67
4.4	Injected proton momentum spectrum for the proton acceptance calculation of the FINUDA spectrometer.	68
4.5	Reconstructed spectra (momentum on the left and energy on the right) of the simulated protons for the target 1 (6Li). . .	69
4.6	Reconstructed spectra (momentum on the left and energy on the right) of the simulated protons for the target 5 (7Li). . .	69
4.7	Results of the FINUDA acceptance calculation for target 1. The same criteria have been used for all the other targets employed in the data analysis.	70
4.8	Results of the FINUDA acceptance calculation for target 5. .	70
4.9	Energy loss of the particle crossing the first layer of the FINUDA silicon microstrips (OSIM).	71
4.10	Energy loss of the particle crossing the inner layer of FINUDA Low Mass Drift Chamber.	72
4.11	Energy loss of the particle crossing the outer layer of FINUDA Low Mass Drift Chamber.	73
5.1	Inclusive momentum spectrum of π^- emitted from ${}^{12}C$ targets. The spectrum is the sum of the data collected from the three ${}^{12}C$ targets employed in the first data taking.	78
5.2	Level scheme of the ${}^{12}_\Lambda C$ bound state.	78
5.3	Momentum spectrum of the π^- with the additional requirement of a proton in coincidence. The grey spectrum represents the π^- spectrum from K^- absorption by two nucleons. The black area of the peak at 273 MeV/c represents the ${}^{12}_\Lambda C$ <i>g.s.</i>	79
5.4	Energy spectrum, acceptance corrected, of the protons emitted in coincidence with a π^- in ${}^{12}_\Lambda C$ <i>g.s.</i> region.	80
5.5	Dots: energy spectrum of the protons emitted in coincidence with a π^- in ${}^{12}_\Lambda C$ <i>g.s.</i> region. Squares : energy spectrum of the protons, from the K^- absorption by two nucleons, emitted in coincidence with pions of the <i>g.s.</i>	80

5.6	Difference of the two spectra of Fig.5.5	81
5.7	Inclusive momentum spectrum of π^- emitted from ${}^7\text{Li}$ targets. The spectrum is the sum of the data collected from the two ${}^7\text{Li}$ targets employed in the first data taking.	83
5.8	Momentum distribution of negative pions detected in coincidence with a proton. The red region corresponds to the ${}^7_\Lambda\text{Li}$ <i>g.s.</i>	83
5.9	Level scheme of the ${}^7_\Lambda\text{Li}$ bound state. Corresponding level of ${}^6\text{Li}$ are also shown.From [77]	84
5.10	Left: Energy spectrum, not acceptance corrected, of the protons emitted in coincidence with a π^- in ${}^7_\Lambda\text{Li}$ <i>g.s.</i> region; right: energy spectrum obtained after the acceptance correction for the ${}^7_\Lambda\text{Li}_{g.s.}$	86
5.11	π^- momentum spectrum for events with an additional proton track and superimposed (red histogram) the contribution to the spectrum of the K^-np channel, normalized to the spectrum tail.	87
5.12	Left: (blue points) protons coming from the weak decay of ${}^7_\Lambda\text{Li}_{g.s.}$; red points: energy spectrum of the protons coming from the background reaction emitted in correspondence of the <i>g.s.</i> . Right: proton spectrum from the NMWD of the ${}^7_\Lambda\text{Li}_{g.s.}$ after the subtraction of the background contribution	88
5.13	Left:energy spectrum, non acceptance corrected, of the protons emitted in coincidence with a π^- emitted after the formation of the ${}^5_\Lambda\text{He}$ with the ${}^7\text{Li}$ target; right: result of the acceptance correction of the proton spectrum shown on the left of this figure.	89
5.14	Left: proton spectrum coming from the background absorption process (red dots) superimposed to the acceptance corrected proton spectrum obtained from the data (blue dots); right: proton energy spectrum of ${}^5_\Lambda\text{He}$ after the background subtraction	90
5.15	Inclusive proton spectra measured following the K^- capture at rest from ${}^6\text{Li}$ (left) and ${}^7\text{Li}$ (right).	91

5.16	Total π^- inclusive spectrum obtained as the sum of the two ${}^6\text{Li}$ targets contribution	91
5.17	π^- spectrum for events with an additional proton track, from the two ${}^6\text{Li}$ targets.	92
5.18	Top: energy spectrum, non acceptance corrected, of the protons emitted in coincidence with a π^- emitted after the formation of the ${}^5_\Lambda\text{He}$ with the ${}^6\text{Li}$ target; bottom: energy spectrum, acceptance corrected, of the protons coming from the NMWD of the ${}^5_\Lambda\text{He}$	93
5.19	Momentum distribution of a quasi- d in typical light nuclei: ${}^4\text{He}$, ${}^6\text{Li}$ and ${}^{12}\text{C}$. The binding energy of quasi- d in these nuclei and the rms momenta are shown in the inset. This calculation is taken from [94].	94
5.20	π^- momentum spectrum for events with an additional proton track (in black) and superimposed (red histogram) the contribution to the spectrum from the K^-np channel.	95
5.21	Energy spectrum of the protons coming from the background absorption process (red dots) superimposed to the acceptance corrected proton spectrum obtained from the data (blue dots) for the ${}^5_\Lambda\text{He}$	95
5.22	Proton energy spectrum coming from the NMWD of ${}^5_\Lambda\text{He}$ after the background subtraction.	96
5.23	Proton energy spectrum of ${}^5_\Lambda\text{He}$ obtained from ${}^7\text{Li}$ targets analysis (blue dots) and the one obtained with the analysis of ${}^6\text{Li}$ targets (red squares). The two spectra are normalized to area beyond 15 MeV.	97
5.24	Total proton energy spectrum of ${}^5_\Lambda\text{He}$ obtained adding the spectrum obtained from ${}^7\text{Li}$ targets analysis (on right of Fig.5.14) and the one obtained with the analysis of ${}^6\text{Li}$ targets (Fig. 5.22). 97	
5.25	Total π^- inclusive momentum spectrum obtained as the sum of the three ${}^{12}\text{C}$; the red region corresponds to the ${}^{12}_\Lambda C_{g.s.}$	98
5.26	${}^{12}_\Lambda\text{C}$ momentum spectrum for the events in which a π^- is detected in coincidence with a proton from the same K^- vertex. Red region: ${}^{12}_\Lambda C_{g.s.}$ momentum interval.	99

- 5.27 Left: energy spectrum, non acceptance corrected, of the protons emitted in coincidence with a π^- coming from the ${}^{12}_{\Lambda}\text{C}$. s.; right: result of the acceptance correction applied to the proton energy spectrum showed on the left of this figure. 99
- 5.28 ${}^{12}_{\Lambda}\text{C}$ momentum spectrum for π^- detected in coincidence with a proton (black) and in (red) the simulated spectrum of the $Kn p$ ansorption reaction. 100
- 5.29 Blue dots: proton energy spectrum, acceptance corrected, of ${}^{12}_{\Lambda}\text{C}$ *g.s.*; red dots: proton energy spectrum from simulation of the K^- absorption by two nucleons, emitted in coincidence with pions in the *g.s.* range (270 MeV/c–276 MeV/c) 101
- 5.30 Energy spectrum of the protons coming from the NMWD of ${}^{12}_{\Lambda}\text{C}$ in its *g.s.* after the background subtraction. 101
- 6.1 Red dots: FINUDA proton spectrum from proton-induced NMWD for ${}^{12}_{\Lambda}\text{C}_{g.s.}$; blue dots: result achieved for the ${}^{12}_{\Lambda}\text{C}_{g.s.}$ at the KEK experiment; the two spectra are normalized to area beyond 35 MeV. 109
- 6.2 Red dots: FINUDA proton spectrum from proton-induced NMWD for ${}^5_{\Lambda}\text{He}$; blue dots: result achieved for the ${}^5_{\Lambda}\text{He}$ at the KEK experiment; the two spectra are normalized to area beyond 35 MeV. 110
- 6.3 proton kinetic energy spectra corresponding to the decay of ${}^5_{\Lambda}\text{He}$ (continuous line) and ${}^{12}_{\Lambda}\text{C}$ (dashed line) obtained without the contribution of the FSI. 111
- 6.4 Red dots: experimental proton spectra of ${}^{12}_{\Lambda}\text{C}$ normalized *per p-induced non mesonic weak decay*; Black curve: theoretical calculation for the proton energy spectrum of ${}^{12}_{\Lambda}\text{C}$ performed with the addition of the FSI contribution. 112
- 6.5 Red dots: experimental proton spectra of ${}^5_{\Lambda}\text{He}$ normalized *per p-induced non mesonic weak decay*; Black curve: theoretical calculation for the proton energy spectrum of ${}^5_{\Lambda}\text{He}$ performed with the addition of the FSI contribution. 112

Bibliography

- [1] M.Danisz and J.Pniewski *Philos. Mag.*, **44** (1953) 348.
- [2] Ajimura S. *et al.*, *Nucl. Phys. A* **585** (1995) 173c.
- [3] Cassing W. *et al.*,*Eur. Phys. J. A* **16** 2003 549.
- [4] Armstrong T. *et al.*, *Phys. Rev.,C* **47** 1993 1957.
- [5] Feshbach H. and Kerman K., *Preludes in Theoretical Physics* edited by A. Deshalit, H.Feshbach and L. Van Hove (North Holland, Amsterdam) 1966 260-278;
- [6] Bonazzola G.C. *et al.*, *Phys. Lett. B* **53** 1974 297;
- [7] Hungherford E.D. *Varenna Course* 2004 55-106;
- [8] Hashimoto O. and Tamura H. *Prog. Part. Nucl Phys.* **57** 2006 564-653;
- [9] G. C. Bonazzola, T. Bressani, E. Chiavassa, G. Dellacasa, A. Fainberg, M. Gallio, N. Mirfakhrai, A. Musso, G. Rinaudo, *Phys. Rev. Lett.* **34**, (1975) 683;
- [10] Yamazaki T., *Proceedings of workshop on Physics and Detectors for DAΦNE* Frascati, April 9-12, 1991, Eds. G. Pancheri, p. 315;
- [11] W. B. Fowler, R. P. Shutt, A. M. Thorndike and W. L. Whittemore, *Production of Heavy Unstable Particles by 1.37 BeV Pions*, *Phys. Rev.* **98**, (1954) 121;
- [12] T. Nagae, *Nucl. Phys. A* **691** (2001) 76c;

-
- [13] W.M. Alberico and G. Garbarino, *Weak decay of Λ -hypernuclei*. Phys. Reports, 369 (2002) 1-109;
- [14] J. Nieves and E. Oset, *Phys. Rev. C*, **47** (1993) 1478;
- [15] T. Motoba and K. Itonaga, *Prog. Theor Phys. Suppl.*, **117** (1994) 477;
- [16] R. S. Hayano *et al.*, *Phys. Lett.,B* **231** 1989 355;
- [17] H. Oota *et al.*, *Prog. Theor. Phys. Supp.*, **117** (1994) 177;
- [18] T. Nagae *et al.*, *Phys. Rev. Lett.*, **80** (1998) 1605;
- [19] T. Harada *et al.*, *Nucl. Phys. A* **507** (1990) 715;
- [20] S. Kameoka *et al.*, *Nucl. Phys. A* **754** (2005) 173;
- [21] H. Oota, in Proc. of the International School of Physics "E. Fermi" Course CLVIII, edited by T. Bressani, A. Filippi and U. Wiedner (IOS Press, Amsterdam) (2004) 219-258;
- [22] J. Cohen, *Prog. Part. Nucl. Phys.*, **25** (1990) 139;
- [23] E. Oset and A. Ramos, *Prog. Part. Nucl. Phys.*, **41** (1998) 191;
- [24] R. H. Dalitz, *Phys. Rev.* **112** (1958) 605; R. H. Dalitz and L. Liu, *Phys. Rev.* **116** (1959) 1312;
- [25] W. Cheston and H. Primakov, *Phys. Rev.* **92** (1953) 1537;
- [26] R. H. Dalitz and G. Rajasekaran, *Phys. Lett.***1** (1962) 58;
- [27] R. H. Dalitz, *Proceedings of the Summer Study Meeting on Nuclear and Hypernuclear Physics with Kaon Beams*, BNL Report No. 18335 (1973) p. 41;
- [28] C. B. Dover, *Few Body Systems Suppl.* 2 (1987) 77;
- [29] W. M. Alberico and G. Garbarino, *Phys. Lett. B* **486** (2000) 362;
- [30] B. H. J. McKellar and B. F. Gibson, *Phys. Rev. C* **30** (1984) 322;
- [31] K. Maltman and M. Shmatikov, *Phys. Rev. C* **51** (1995) 1576;

- [32] G. Nardulli, *Phys. Rev. C* **38** (1988) 832;
- [33] J. F. Dubach, G. B. Feldman, B. R. Holstein and L. de la Torre, *Nucl. Phys. A* **450** (1986) 71c;
- [34] C. Y. Cheung *et al.*, *Phys. Rev. C* **27** (1983) 335;
- [35] D. P. Heddle and L. S. Kisslinger *Phys. Rev. C* **3** (1985) 608;
- [36] T. Inoue *et al.*, *Nucl. Phys. A* **597** (1995) 563;
- [37] T. Inoue *et al.*, *Nucl. Phys. A* **633** (1998) 312;
- [38] K. Sasaki *et al.*, *Nucl. Phys. A* **669** (2000) 331; **678** (2000) 455;
- [39] K. Itonaga, T. Ueda and T. Motoba, *Phys. Rev. C*, **65** (2002)034617.
- [40] A. Parreno and A. Ramos, *Phys. Rev. C*, **65** (2002);
- [41] D. Jido, E. Oset and J. E. Palomar, *Nucl. Phys. A*, **694** (2001) 525;
- [42] J. J. Szymanski *et al.*, *Phys. Rev. C*, **43** (1991) 849;
- [43] H. Noumi *et al.*, *Phys. Rev. C*, **52** (1995) 2936;
- [44] H. Noumi *et al.*, *Proceedings of the IV International Symposium on Weak and Electromagnetic Interactions in Nuclei*, H. Ejiri, T. Kishimoto and T. Sato eds, World Scientific(1995) p. 550;
- [45] Y. Sato *et al.*, *Physical Review C* **71**, (2005) 025203;
- [46] H. Ota, *Proceedings of VIII International Conference on Hypernuclear and Strange Particle Physics (HYP2003)*, JLab, Newport News, Virginia;
- [47] J. H. Kim *et al.*, *Phys. Rev. C*, **68** (2003) 065201;
- [48] S. Okada *et al.*, *Phys. Lett. B*, **597** (2004) 249;
- [49] Botta Elena (Phd thesis) *Il sistema di tracciamento dell'esperimento FINUDA*, (1995) Università degli Studi di Torino (Italy).

- [50] Giraudo Mauro (Physics degree thesis) *Misura di coordinata con il metodo di divisione di carica*, (1998) Università degli Studi di Torino (Italy).
- [51] The FINUDA Collaboration: *FINUDA Technical report*, SIS-Pubblicazioni dei Laboratori Nazionali di Frascati, P.O Box 13, I-00044, Frascati (Italy).
- [52] L. Benussi *et al.*, *The FINUDA straw tubes detector*, Nuclear Instruments and Methods in Physics Research A, **379** (1996) 649-650.
- [53] Piano Stefano (PHD thesis) *Search for Σ Hypernuclear states with the FINUDA spectrometer*, (2002) Università degli studi di Trieste (Italy);
- [54] V. Innocente, M. Maire and E. Nagy, *GEANE: Average Tracking and Error Propagation Package*, CERN Program Library W5013-E (1991);
- [55] R. Brun, *et al.*, "GEANT", CERN, DD, EE, 84-1, Revised 1987;
- [56] H. Wind, *Nucl. Instr. Meth.* **84**(1970), 117
- [57] H. Noumi *et al.*, *Nucl. Phys. A* **691** (2001) 123c.
- [58] T. Nagae *et al.*, *Nucl. Phys. A* **691** (2001) 76.
- [59] M. Agnello *et al.*, *Eur. Phys. J. A* **33**, 251-254 (2007);
- [60] H. Tamura *et al.*, *Phys. Lett. B* **32** (1985);
- [61] T. Hasegawa, *et al.*, *Phys. Rev. Lett.*, **74** (1995) 224;
- [62] Zenoni A., *Proc. Int. School of E. Fermi Course CLVIII* (eds, T. Bressani, A. Filippi and U. Wiedern), IOS Press (Amsterdam), (2005), p. 183.
- [63] Park H. *et al.*, *Phys. Rev. C* **61** (2000) 054004;
- [64] Bhang H. *et al.*, *Phys. Rev. Lett.* **81** (1998) 4321;
- [65] Ericson M., *Nucl. Phys. A* **547** (1992) 127c;
- [66] Ramos A. *et al.*, *Phys. Rev. C* **55** (1997) 735;

- [67] Ramos A. *et al.*, *Phys. Rev. C* **50** (1994) 2314;
- [68] Alberico W.M. *et al.*, *Phys. Rev. C* **61**,(2000) 044314;
- [69] Alberico W.M. *et al.*, *Phys. Rep.* **369** (2002) 1;
- [70] Sasaki K. *et al.*, *Nucl. Phys. A* **669** (2000) 331; *Nucl. Phys. A* **678** (2000) 455.
- [71] Parreno A. *et al.*, *Phys. Rev. C* **65** (2002) 015204;
- [72] Outa H. *et al.*, *Nucl. Phys. A* **754** (2005) 157c;
- [73] B.H. Kang *et al.*, *Phys. Rev. Lett.*, **96**, (2006), 062301;
- [74] Kim M.J. *et al.*, nucl-ex/0601029v2 (2006);
- [75] FINUDA Collaboration, M. Agnello *et al.*, *Phys. Lett. B* (2005);
- [76] FINUDA Collaboration, paper in preparation
- [77] O. Hashimoto, H. Tamura, *Prog. Part. Nucl. Phys.* **57** (2006), 564
- [78] S. Ajimura *et al.*, *Nucl. Phys.* **A639** (1998), 93c
- [79] R.H. Dalitz, A. Gal, *Phys. Rev. Lett.* **36** (1976), 362
- [80] H. Band *et al.*, *Nucl. Phys.* **A450** (1986), 217c
- [81] P.H. Pile *et al.*, *Phys. Rev. Lett.* **66** (1991), 2585
- [82] M. Jurić *et al.*, *Nucl. Phys.* **B52** (1973) 1.
- [83] K. Itonaga *et al.*, *Phys. Rev. C* **49** (1994), 1045
- [84] M. May *et al.*, *Phys. Rev. Lett.* **47** (1981), 1106
- [85] T. Motoba *et al.*, *Phys. Rev. C* **38** (1998), 1322
- [86] K. Itonaga *et al.*, *Prog. Theor. Phys.* **84** (1990), 291
- [87] A. Bouyssy, *Phys. Lett. B* **84** (1979), 41; *Phys. Lett. B* **91** (1979), 15
- [88] H. Tamura, *et al.*, *Phys. Rev. Lett.* **84**, 5963-5966 (2000);

-
- [89] T. Bressani, *et al.*, *Nucl. Phys. B* **9**, 427 (1969);
- [90] FINUDA Collaboration, M. Agnello *et al.*, *Nucl. Phys. A* **775**, (2006) 35;
- [91] J. Favier, *et al.*, *Nucl. Phys. A* **169**, 540 (1971);
- [92] C. Cernigoi, *et al.*, *Nucl. Phys. A* **352**, 343 (1981);
- [93] C. Cernigoi, *et al.*, *Nucl. Phys. A* **456**, 599 (1986);
- [94] T. Yamazaki and Y. Akaishi, *Nucl. Phys. A* **792**, 229 (2007);
- [95] A. Parreno and A. Ramos *Phys. Rev. C* **65** 015204 (2001);
- [96] V.G.J.toks and Th.A. Rijken, *Phys. Rev. C* **59** 30099 (1999);
- [97] J.J. Szymansky *et al.*, *Phys. Rev. C* **43** 849 (1991);
- [98] H. Noumi *et al.*, *Phys. Rev. C* **52** 2936 (1995);
- [99] S. Okada *et al.*, *Phys. Lett. B* **597**, 249 (2004);
- [100] G. Garbarino *et al.*, *Phys. Rev. C* **69** 054603 (2004);
- [101] E. Bauer *et al.* **arXiv:nucl-th/0602066v1**;